UNIVERSITÀ DEGLI STUDI DI NAPOLI FEDERICO II

SCUOLA DI DOTTORATO IN INGEGNERIA INDUSTRIALE

SCUOLA POLITECNICA E DELLE SCIENZE DI BASE
DOTTORATO DI RICERCA IN INGEGNERIA DEI SISTEMI MECCANICI
Dipartimento di Ingegneria Industriale

A CFD Approach to the Optimization of Components in Fluid Power

Relatore

Ch. mo Prof. Ing. Adolfo Senatore

Ch. mo Prof. Ing. Kim A. Stelson

Candidato

Emma Frosina

Matricola 107215

Correlatori

Ing. Dario Buono

Anno Accademico 2015/2016

SUMMARY

INTRODUCTION

Hydraulics has the highest energy density of any power transmission technology and is a very effective way to transfer power from a source to a user. The convenience of sharing a single power source with many users with high reliability, justifies the wide use of this technology. The recent development of new components and technologies especially the use of electronic sensors and controls on hydraulic components, makes hydraulic systems more flexible and efficient. Hydraulic systems can be used in niche application where electromagnetic effects must be avoided. But hydraulics has a few disadvantage including low efficiency, high costs, noise, leaks and complexity.

Hydraulic systems capability of creating high forces with small electronic control devices has found wide application, and electro hydraulic components are widely used in applications that require precise actuator control or matching of variable working conditions.

Hydraulic is widely used in many sectors. In this PhD Thesis the research has been focused on the optimization of hydraulic components used in the industrial fields and on engines for lubrication circuits.

In recent years, many studies were initiated to improve the performance of hydraulic components. However, the scientific understanding of valves, pumps and transmissions operation is limited because of the lack of three-dimensional fluid dynamics computation capability. In this PhD thesis a 3D computational fluid dynamics (CFD) modeling technique developed by the Hydraulic Research Group of the University of Naples Federico II led by Professor Adolfo Senatore is presented. The methodology has been applied for the study of several different applications. Using a three-dimensional CFD approach it is possible to improve component performance and the understanding of the internal flow of each component. To achieve the goals, the hydraulic research group of University of Naples “Federico II” has worked in close collaboration with the Center for Compact and Efficient Fluid Power at the University of Minnesota led by the Professor Kim A. Stelson.

The first chapter describes, in detail, the three-dimensional CFD modeling methodology proposed in this thesis. After an introduction to Computational Fluid Dynamics (CFD), the methodology will be shown along with all possible applications.

Then, in the second chapter, each study will be presented. Research is focused on the optimization of hydraulic components. In particular, these applications were studied:

1) Hydro - Mechanical Transmission,
2) Variable Displacement Vane pump,
3) Gerotor Pumps,
4) Engine Lubrication Circuit,
5) Pumps as Turbine (PAT),
6) Directional Spool Valve,
7) Flow Control Valve.

The results demonstrate that the technique achieves high accuracy for a wide variety of applications and components.

CHAPTER 1 - COMPUTATIONAL FLUID DYNAMICS

Introduction

This PhD thesis presents the results obtained applying a modeling technique for the optimization of hydraulic components. This methodology has been developed by the Hydraulic Research Group of the University of Naples "Federico II" coordinated by the Prof. Adolfo Senatore. Nowadays, the research in this field is conducted using experimentation or modeling. The powerful of numerical approaches make it possible to study and get insights on the physical behavior inside components by monitoring variables that are extremely difficult or impossible to measure. In this way the design or the optimization of a new component becomes faster and easier reducing the experimentation phase to the verification of the model results.

Modeling techniques can be one-dimensional or three-dimensional. The first is easier and quicker but requires setting calibration parameters to achieve a satisfactory accuracy. For this reason, one-dimension modeling is more closely linked to experimentation. Three-dimensional models do not need experimentation to be built since the model is directly obtained from the real geometry of the component without any calibration. But, three-dimensional Computational Fluid Dynamics (CFD) techniques require more computing power and higher computational time. Computational time is a function of the number of the 3D cells of the mesh. However, the development of software able to have a high accuracy with mesh less dense combined with powerful computers enables the more widespread use of three-dimensional modeling approaches, compared to the relatively limited one-dimensional models, especially in the design and optimization of hydraulic components. For this reason, studies shown in this thesis have been approached with a three-dimensional technique of modeling. Furthermore, thanks to the interaction with software developers, many new functions have been introduced to simulate innovative components.

From 3D geometries, fluid volumes have been extracted and meshed. Studies on the mesh sensitivity have been done for each project to find the best compromise

between the computational time and the accuracy. For example, boundary layers have been studied separately by increasing the grid density on the surface without excessively increasing the total cell count.

CFD codes solve the Navier-Stokes equations. The analytic resolution of these equations is possible only in simple cases such as laminar flows, and simple geometries (spheres, flat sheets), while the resolutions of real cases, with complex geometries or where turbulent flows frequently appear, require a numerical approach. So there are different ways to solve the Navier-Stokes equations, and there is a variety of software available based on various approaches. The typical approach requires discretizing the fluid domain in elementary cells to obtain a calculation grid (called mesh), on which to apply resolution methods iterative to solve the Navier-Stokes or Euler equations. In this chapter, various methods of discretization of the fluid volume will be presented.

1.1 Computational Fluid Dynamic

To obtain numerically an approximate solution of Navier-Stokes Equations [1], it is necessary a discretization method which approximates the differential equations by a system of algebraic equations.

Much as the accuracy of experimental data depends on the quality of the tools used, the accuracy of numerical solutions is function of the quality of discretization used.

Contained within the broad field of computational fluid dynamics are activities that cover the range from the automation of well-established engineering design methods to the use of detailed solutions of the Navier-Stokes equations as substitutes for experimental research into the nature of complex flows.

1.1.1 Components of a Numerical Solution Method

Mathematical Model

The starting point of any modeling method is the mathematical model [1], i.e. the set of partial differential or integro-differential equations and boundary conditions. One chooses an appropriate model for the target application (incompressible, inviscid,

turbulent; two or three-dimensional, etc.). This model may include simplifications of the exact conservation laws. A solution method is usually designed for a particular set of equations. Trying to produce a general purpose solution method, i.e. one which is applicable to all flows, is impractical, if not impossible and, as with most general purpose tools, they are usually not optimum for any one application.

Discretization Method

After selecting the mathematical model, one has to choose a suitable discretization method, i.e. a method that approximates the differential equations by a system of algebraic equations for the variables at some set of discrete locations in space and time. There are many approaches, but the most important of which are: the Finite Difference (FD), the Finite Volume (FV) and the Finite Element (FE) methods. Each type of method yields the same solution if the grid is very fine. However, some methods are more suitable to some classes of problems than others.

Coordinate and Basis Vector Systems

The conservation equations can be written in many different forms, depending on the coordinate system and the basis vectors used.

The choice between Cartesian, cylindrical or spherical coordinate systems depends on the target flow, and may influence the discretization method and grid type to be used.

Numerical Grid

The numerical grid defines the discrete locations at which the variables are to be calculated. This grid [1] is essentially a discrete representation of the geometric domain on which the problem is to be solved. It divides the solution domain into a finite number of subdomains (elements, control volumes etc.).

Some of the options available are the following:

- *Structured (regular) grid*: This is the simplest grid structure, since it is logically equivalent to a Cartesian grid. Each point has four nearest neighbors in two dimensions and six in three dimensions.

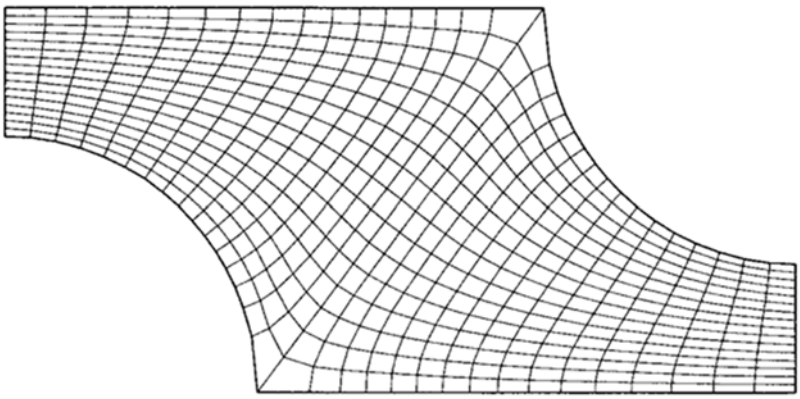

FIGURE 1.1: STRUCTURED GRID

- *Lock-structured grid*: In a block structured grid, there are two (or more) levels subdivision of solution domain. On the coarse level, there are blocks which are relatively large segments of the domain; their structure may be irregular and they may or may not overlap. On the fine level (within each block), a structured grid is defined. This kind of grid is more flexible than the previous ones, as it allows use of finer grid in regions, where greater resolution is required.

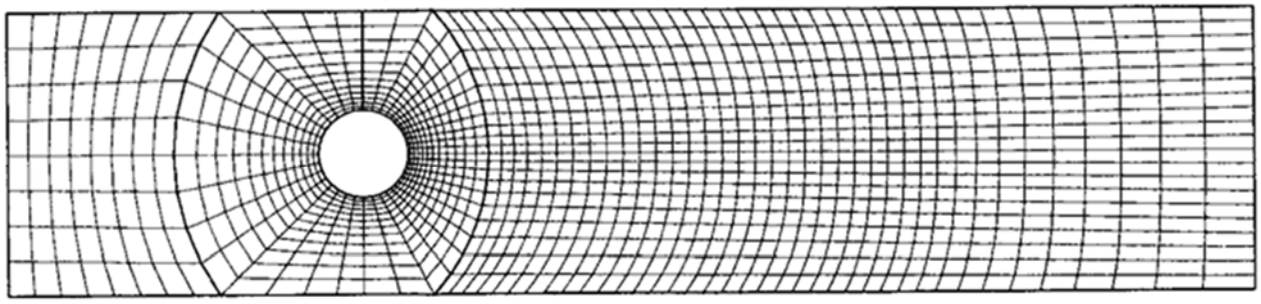

FIGURE 1.2: BLOCK-STRUCTURED GRID

- *Unstructured grids*: For very complex geometries, the most flexible type of grid is one that can fit an arbitrary solution domain boundary. Elements or control volumes may have any shape; nor is there a restriction on the number of neighbor elements or nodes.

Following the choice of grid type, one has to select the approximations to be used in the discretization process. In a finite difference method, approximations for the derivatives at the grid points have to be selected. In a finite volume method, one has to

select the methods of approximating surface and volume integrals. In a finite element method, one has to choose shape functions (elements) and weighting functions.

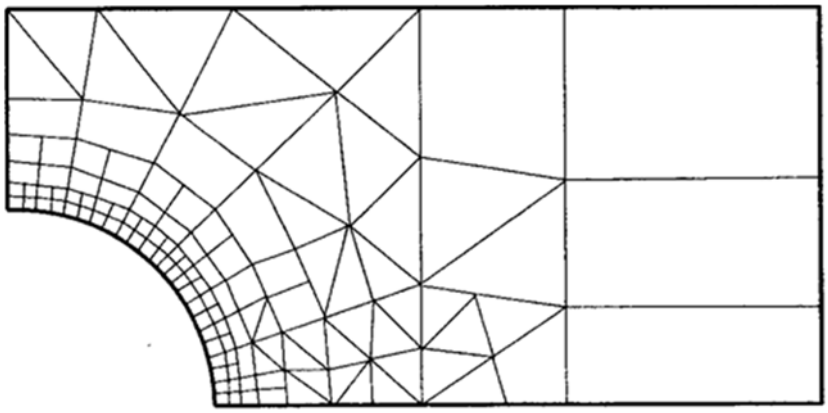

FIGURE 1.3: UNSTRUCTURED GRIDS

Solution Method and convergence criteria

Discretization yields a large system of non-linear algebraic equations. The method of solution depends on the problem. For unsteady flows, methods [1] based on those used for initial value problems for ordinary differential equations (marching in time) are used. At each time step, an elliptic problem has to be solved. Pseudo-time marching or an equivalent iteration scheme usually solves steady flow problems. Since the equations are non-linear, an iteration scheme is used to solve them. These methods use successive linearization of the equations and the resulting linear systems are usually solved by iterative techniques. The choice of solver depends on the grid type and the number of nodes involved in each algebraic equation.

Finally, one needs to set the convergence criteria for the iterative method. Usually, there are two levels of iterations: inner iterations, within which the linear equation are solved, and outer iterations, that deal with the non-linearity and coupling of the equations. Deciding when to stop the iterative process on each level is important, from both the accuracy and efficiency points of view.

1.1.2 Properties of Numerical Solution Methods

The solution method should have certain properties. In most cases, it is not possible to analyze the complete solution method [1]. One analyzes components of the

method; if the components do not possess the desired properties, neither will the complete method but the reverse is not necessarily true.

Consistency

The difference between the discretized equation and the exact one is called the "truncation error". This error is usually estimated by replacing all the nodal values in the discrete approximation by a Taylor series expansion about a single point. For a method to be consistent, the truncation error must become zero when the mesh spacing $\Delta t \to 0$ and/or $\Delta x_i \to 0$. Truncation error is usually proportional to a power of the grid spacing Δx_i and/or the time step Δt. If the most important term is proportional to $(\Delta x_i)^n$ or $(\Delta t)^n$ the method is called an nth-order approximation; $n > 0$ is required for consistency.

Stability

A numerical solution method is said to be "stable" if it does not magnify the errors that appear in the course of numerical solution process. For temporal problems, stability guarantees that the method produces a bounded solution whenever the solution of the exact equation is bounded. For iterative methods, a stable method is one that does not diverge. Stability can be difficult to investigate, especially when boundary conditions non-linear are present.

Convergence

A numerical method is said to be "convergent" if the solution of the discretized equations tends to the exact solution of the differential equation as the grid spacing tends to zero. For linear initial value problems, the equivalence theorem (Richtmyer and Morton, 1967) states that "given a properly posed linear initial value problem and a finite difference approximation to it that satisfies the consistency condition, stability is the necessary and sufficient condition for convergence". Obviously, a consistent scheme is useless unless the solution method converges.

For non-linear problems which are strongly influenced by boundary conditions, the stability and convergence of a method are difficult to demonstrate. Therefore,

convergence is usually checked using numerical experiments, i.e. repeating the calculation on a series of successively refined grids. If the method is stable and if all approximations used in the discretization process are consistent, we usually find that the solution does converge to a grid-independent solution.

Conservation

Since the equations to be solved are conservation laws, the numerical scheme should also - on both a local and a global basis - respect these laws. This means that, at steady state and in the absence of sources, the amount of a conserved quantity leaving a closed volume is equal to the amount entering that volume. If the strong conservation form of equations and a finite volume method are used, this is guaranteed for each individual control volume and for the solution domain as a whole. Other discretization methods can be made conservative if care is taken in the choice of approximations. The treatment of sources or sink terms should be consistent so that the total source or sink in the domain is equal to the net flux of the conserved quantity through the boundaries.

This is an important property of the solution method, since it imposes a constraint on the solution error. If the conservation of mass, momentum and energy are insured, the error can only improperly distribute these quantities over the solution domain. Non-conservative schemes can produce artificial sources and sinks, changing the balance both locally and globally. However, non-conservative schemes can be consistent and stable and therefore lead to correct solutions in the limit of very fine grids. Errors due to non-conservation are in most cases appreciable only on relatively coarse grids. The problem is that it is difficult to know on which grid these errors are small enough. Conservative schemes are therefore preferred.

Boundedness

Numerical solutions should lie within proper bounds. Physically non-negative quantities (like density, kinetic energy of turbulence) must always be positive. In the absence of sources, some equations (e.g. the heat equation for the temperature when no heat sources are present) require that the minimum and maximum values of the variable be found on the boundaries of the domain.

Realizability

Models of phenomena which are too complex to treat directly (for example, turbulence, combustion, or multiphase flow) should be designed to guarantee physically realistic solutions. This is not a numerical issue but models that are not realizable may result in unphysical solutions or cause numerical methods to diverge.

Accuracy

Numerical solutions of fluid flow and heat transfer problems are only approximate solutions. In addition to the errors that might be introduced in the course of the development of the solution algorithm, in programming or setting up the boundary conditions, numerical solutions always include three kinds of systematic errors:

- Modeling errors, which are defined as the difference between the actual flow and the exact solution of the mathematical model;
- Discretization errors, defined as the difference between the exact solution of the conservation equations and the exact solution of the algebraic system of equations obtained by discretizing these equations, and
- Iteration errors, defined as the difference between the iterative and exact solutions of the algebraic equations systems.

Iteration errors are often called convergence errors.

However, the term convergence is used not only in conjunction with error reduction in iterative solution methods, but is also (quite appropriately) often associated with the convergence of numerical solutions towards a grid-independent solution, in which case it is closely linked to discretization error. Various errors may cancel each other, so that sometimes a solution obtained on a coarse grid may agree better with the experiment than a solution on a finer grid which, by definition, should be more accurate.

As already said, that discretization approximations introduce errors which decrease as the grid is refined, and that the order of the approximation is a measure of

accuracy. However, on a given grid, methods of the same order may produce solution errors which differ by as much as an order of magnitude. This is because the order only tells us the rate at which the error decreases as the mesh spacing is reduced; it gives no information about the error on a single grid. Errors due to iterative solution and round - off are easier to control.

The ultimate goal is to obtain desired accuracy with least effort, or the maximum accuracy with the available resources.

1.1.3 Discretization Approaches

As mentioned above the most important discretization approaches are the Finite Difference (FD), the Finite Volume (FV) and the Finite Element (FE) method.

Finite Difference Method

This is the oldest method for numerical solution of Partial Differential Equations, believed to have been introduced by Euler in the 18th century. It is also the easiest method to use for simple geometries.

The starting point is the conservation equation in differential form. A grid covers the solution domain. At each grid point, the differential equation is approximated by replacing the partial derivatives by approximations in terms of the nodal values of the functions. The result is one algebraic equation per grid node, in which the variable value at that and a certain number of neighbor nodes appear as unknowns. The grid lines serve as local coordinate lines.

Finite Volume Method

The FV method uses the integral form of the conservation equations as its starting point. The solution domain is subdivided into a finite number of contiguous control volumes (CVs), and the conservation equations are applied to each CV. At the centroid of each CV lies a computational node at which the variable values are to be calculated. Interpolation is used to express variable values at the CV surface in terms of the nodal (CV-center) values. As a result, one obtains an algebraic equation for each CV, in which a number of neighbor nodal values appear.

The FV method can accommodate any type of grid, so it is suitable for complex geometries. The grid defines only the control volume boundaries and need not be related to a coordinate system.

The FV approach is perhaps the simplest to understand and to program. All terms that need be approximated have physical meaning which is why it is popular with engineers.

Finite Element Method

The FE method is similar to the FV method in many ways. The domain is broken into a set of discrete volumes or finite elements that are generally unstructured; in 2D, they are usually triangles or quadrilaterals, while in 3D tetrahedral or hexahedra are most often used. The distinguishing feature of FE methods is that the equations are multiplied by a weight function before they are integrated over the entire domain. In the simplest FE methods, the solution is approximated by a linear shape function within each element in a way that guarantees continuity of the solution across element boundaries. Such a function can be constructed from its values at the corners of the elements. The result is a set of non-linear algebraic equations.

An important advantage of finite element methods is the ability to deal with arbitrary geometries and the grids are easily refined. The principal drawback, which is shared by any method that uses unstructured grids, is that the matrices of the linearized equations are not as well structured as those for regular grids making it more difficult to find efficient solution methods.

1.2 Applied Three-Dimensional Methodology

As said in the chapter introduction, models have been built up using a commercial code. After an analysis on codes available, the software PumpLinx® has be chosen because it has been developed to study many of the common problem of hydraulic components.

PumpLinx® (developed by Simerics Inc.®) solves numerically the fundamental conservation equations of mass, momentum and energy and includes accurate physical models for turbulence and cavitation [3].

PumpLinx® grids use a body-fitted binary tree approach [3 - 5].

This type of grids is accurate and efficient because:

- The parent-child tree architecture allows for an expandable data structure with reduced memory storage;
- Binary refinement is optimal for transitioning between different length scales and resolutions within the model;
- The majority of cells are cubes, which is the optimum cell type in terms of orthogonally, aspect ratio, and skew ness thereby reducing the influence of numerical errors and improving speed and accuracy;
- It can be automated, greatly reducing the set-up time;
- Since the grid is created from a volume, it can tolerate "dirty" CAD surfaces with small cracks and overlaps.

In the boundary layer, the binary tree approach can easily increase the grid density on the surface without excessively increasing the total cell count. In the regions of high curvature and small details, the grid has been subdivided and cut to conform to the surface.

As already stated, the code, during the simulations, solves the conservation equations for mass, momentum and energy:

Mass Conservation:

$$\frac{\vartheta}{\vartheta t}\int_{\Omega(t)}^{0}\rho d\Omega + \int_{\sigma}^{0}\rho(v - v_{\sigma})nd\sigma = 0 \qquad (1.1)$$

Momentum Conservation:

$$\frac{\vartheta}{\vartheta t}\int_{\Omega(t)}^{0}\rho v d\Omega + \int_{\sigma}^{0}\rho\big((v - v_{\sigma})n\big)vd\sigma = \int_{\sigma}^{0}\tilde{\tau}nd\sigma - \int_{\sigma}^{0}pnd\sigma + \int_{\Omega}^{0}fd\Omega \qquad (1.2)$$

Energy Conservation:

$$\frac{\vartheta}{\vartheta t}\left[\rho\left(u + \frac{v^2}{2} + gz\right)\right] + \nabla\left[\rho v\left(h + \frac{v^2}{2} + gz\right)\right] + \nabla Q - \nabla(T_d v) = 0 \qquad (1.3)$$

in which $\Omega(t)$ is the control volume, σ is the control volume surface, n is the surface normal pointed outwards, ρ is the fluid density, p is the pressure, f is the body force, v is the fluid velocity, v_σ is the surface motion velocity. The shear stress tensor $\tilde{\tau}$ is a function of the fluid viscosity μ and of the velocity gradient; for a Newtonian fluid this is given by the following equation:

$$\tau_{ij} = \mu\left(\frac{\vartheta u_i}{\vartheta x_j} + \frac{\vartheta u_j}{\vartheta x_i}\right) - \frac{2}{3}\mu\frac{\vartheta u_k}{\vartheta x_k}\delta_{ij} \qquad (1.4)$$

where u_i (i = 1, 2, 3) is the velocity component and δ_{ij} is the Kronecker delta function.

The code allows for the simultaneous treatment of moving and stationary fluid volumes. Each volume connects to the others via an implicit interface. The PumpLinx® Mismatched Grid Interface is a very efficient implicit algorithm that identifies the overlap areas and matches them without interpolation. After that, this area is treated as the common face connecting cells on both sides of the interface. During the simulation process, this face is treated no differently than an internal face between two neighboring cells in the same grid domain [3]. Thanks to this approach, the solution becomes very robust, quick and accurate.

Turbulence models for computing effective liquid viscosities are important at high Reynolds numbers. Mature turbulence models, such as the standard $k - \varepsilon$ is implemented [5]. This model has been available for more than a decade and has been widely demonstrated to provide good engineering results. In the CFD 3D modeling there are other resolution method more accurate than the $k - \varepsilon$ model and RNG $k - \varepsilon$ model. As a matter of fact, for the specific problem, losses due to the viscous stresses are negligible compared to pressure forces. The adoption of higher order turbulence models would have increased the computational time with no relevant improvement of the results. Therefore, the K - Epsilon model was used as it is numerically robust, computationally efficient and it provides good accuracy. This strategy was used by the Hydraulic Research Group of the University of Naples for many analyses confirming the solution accuracy. Thus the adopted model for simulations is the standard $k - \varepsilon$

(and not others RNG, LES, or DES etc.) because, in this field, results are faithful at the real phenomenon [2], [5].

The standard k − ε model is based on the following two equations:

$$\frac{\vartheta}{\vartheta t}\int_{\Omega(t)}^{0}\rho k d\Omega + \int_{\sigma}^{0}\rho\big((v-v_\sigma)n\big)k d\sigma =$$

$$\int_{\sigma}^{0}\left(\mu+\frac{\mu_t}{\sigma_k}\right)(\nabla k n)n d\sigma + \int_{\Omega}^{0}(G_t-\rho\varepsilon)d\Omega \qquad (1.5)$$

$$\frac{\vartheta}{\vartheta t}\int_{\Omega(t)}^{0}\rho\varepsilon d\Omega + \int_{\sigma}^{0}\rho\big((v-v_\sigma)n\big)\varepsilon d\sigma =$$

$$\int_{\sigma}^{0}\left(\mu+\frac{\mu_t}{\sigma_\varepsilon}\right)(\nabla\varepsilon n)n d\sigma + \int_{\Omega}^{0}\left(c_1 G_t\frac{\varepsilon}{k}-c_2\rho\frac{\varepsilon^2}{k}\right)d\Omega \qquad (1.6)$$

with $c_1 = 1.44$, $c_1 = 1.92$, $\sigma_k = 1$, $\sigma_\varepsilon = 1.3$; where σ_k e σ_ε are the turbulent kinetic energy and the turbulent kinetic energy dissipation rate Prandtl numbers.

The turbulent kinetic energy, k, is defined as:

$$k = \frac{1}{2}(v'\cdot v') \qquad (1.7)$$

with v' being the turbulent fluctuation velocity, and the dissipation rate, ε, of the turbulent kinetic energy is defined as:

$$\varepsilon = 2\frac{\mu}{\rho}\left(\overline{S'_{ij}S'_{ij}}\right) \qquad (1.8)$$

in which the strain tensor is:

$$S'_{ij} = \frac{1}{2}\left(\frac{\vartheta u'_i}{\vartheta x_j}+\frac{\vartheta u'_j}{\vartheta x_i}\right) \qquad (1.8)$$

with u'_i (i = 1, 2, 3) being components of v'.

The turbulent viscosity μ_t is calculated by:

$$\mu_t = \rho C_\mu\frac{k^2}{\varepsilon} \qquad (1.10)$$

with $C_\mu = 0.09$.

The turbulent generation term G_t can be expressed as a function of velocity and the shear stress tensor as:

$$G_t = -\rho\overline{u_i' u_j'}\frac{\vartheta u_i'}{\vartheta x_j} \tag{1.11}$$

where $\tau_{ij}' = \rho\overline{u_i' u_j'}$ is the turbulent Reynolds stress, which can be modelled by the Boussinesq hypothesis:

$$\tau_{ij}' = \mu_t\left(\frac{\vartheta u_i}{\vartheta x_j} + \frac{\vartheta u_j}{\vartheta x_i}\right) - \frac{2}{3}\left(\rho k + \frac{\vartheta u_k}{\vartheta x_k}\right)\delta_{ij} \tag{1.12}$$

A real fluid model based on the work of Singhal [6] is implemented allowing the calculation of cavitation effects, when pressure in a specified zone of the fluid domain falls below the saturation pressure. Vapor bubbles form and then collapse as the pressure rise again [7 – 10].

Many physical models for the formation and transport of vapor bubbles in the liquid are available in literature, but only few computational codes offer robust cavitation models. This is due to the difficulty to handle gas/liquid mixtures with very different densities. Even small pressure variations may cause numerical instability if they are not optimally treated [10].

The cavitation model implemented in PumpLinx® uses the following equations (Rayleigh – Plesset) [3], [11]:

$$\frac{\vartheta}{\vartheta t}\int_{\Omega(t)} \rho f d\Omega + \int_{\sigma} \rho\big((v - v_\sigma)n\big) f d\sigma =$$

$$\int_{\sigma}\left(D_f + \frac{\mu_t}{\sigma_f}\right)(\nabla f n)\, d\sigma + \int_{\Omega}(R_e - R_c) d\Omega \tag{1.13}$$

where D_f is the diffusivity of the vapor mass fraction and σ_f is the turbulent Schmidt number. In the present study, these two numbers are set equal to the mixture viscosity and unity, respectively. The vapor generation term, R_e, and the condensation rate, R_c, are modeled as:

$$R_e = C_e\frac{\sqrt{k}}{\sigma_l}\rho_l\rho_v\left[\frac{2}{3}\frac{(p - p_v)}{\rho_l}\right]^{\frac{1}{2}}\left(1 - f_v - f_g\right) \tag{1.14}$$

$$R_c = C_c \frac{\sqrt{k}}{\sigma_l} \rho_l \rho_v \left[\frac{2}{3}\frac{(p-p_v)}{\rho_l}\right]^{\frac{1}{2}} f_v \quad (1.15)$$

in which the model constants are $C_e = 0.02$ and $C_c = 0.01$.

The final density calculation for the mixture is done by:

$$\frac{1}{\rho} = \frac{f_v}{\rho_v} + \frac{f_g}{\rho_g} + \frac{(1-f_v-f_g)}{\rho_l} \quad (1.16)$$

The fluid model accounts for liquid compressibility. This is critical to accurately model pressure wave propagation in liquid. The liquid compressibility is found to be very important for a high-pressure system and the systems in which water hammer effects are relevant.

CHAPTER 2 - Components Optimization

Introduction

The three-dimensional CDF modeling approach described in the first chapter has been applied for the optimization of many hydraulic components. In Chapter 2 all case studies are presented.

Research have been focused on the design and optimization of:

1) Hydro - Mechanical Transmission,
2) Variable Displacement Vane pump,
3) Gerotor Pumps,
4) Engine Lubrication Circuit,
5) Pumps as Turbine (PAT),
6) Directional Spool Valve,
7) Flow Control Valve.

The first study is a result of collaboration of the University of Naples "Federico II" with the hydraulic research group of coordinated by the Professor Kim A. Stelson of the University of Minnesota (Minneapolis, USA). The universities involved in this project worked in close cooperation for the study of a novel vane pump power split transmission patented by the Australian company, the Mathers Hydraulics®. After an introduction on the application of the vane pump power split transmission and a comparison with the other technologies applied for vehicles transmissions the pump is studied in depth. Then the model will be shown with its results and, by the end, simulations will be applied to estimate the efficiency of the vane pump.

The second study is focused on a variable displacement vane pump applied for a lubrication circuit of a modern high-performance engine. The model has been built taking into account all of the thermo-fluid dynamic conditions with particular attention to cavitation. The aim of the research is to study the component in depth to find working anomalies. Vane variable displacement oil pumps are widely adopted on engines to reduce the torque needed to drive the oil pump. This type of pump is going to become a standard on engines because by using a variable displacement oil pump, it is possible

to reduce the vehicle fuel consumption by about 1–3%. The research demonstrates that the developed approach is the best way to analyze phenomena that occur during pump operation, such as cavitation, to calculate the flow - rate limit during the eccentricity variations and, consequently, the displacement variation. The model also allows determining the forces between the pump rotating elements that influence the equilibrium of the ring and consequently the displacement variation.

The third study concerns the identification of the main losses that effect the volumetric efficiency of a gerotor pump installed on a diesel engine. An accurate analysis of the losses from leakage between inner and outer elements of a gerotor pump through a modeling approach will be shown. Using the proposed method, information has been obtained that is not measurable.

Following the research on a gerotor pump, the forth study is focused on the lubrication circuit of a diesel engine modeling the pump and all the circuit with a three-dimensional approach. This research has demonstrated that the modeling technique can be applied not only for the pump but also for the lubrication circuit without greatly increasing computational time. The model has been validated with data from experiments from the hydraulic laboratory of the Industrial Engineering Department of the University of Naples. The oil pump model has been coupled with a three-dimensional model of the entire lubrication circuit, to compute the hydraulic resistances of the network and the oil consumption rate of the circuit components.

In the fifth project, a centrifugal pump (also called PAT, pump as turbine) has been analyzed. These pumps are a solution for generating and recovering power in small and micro hydropower situations. Pumps are relatively simple machines, inexpensive (compared to hydraulic turbines), and readily available worldwide. The study showed that CFD analysis is an effective design tool for predicting the performance of centrifugal pumps in turbine mode and for identifying the losses in turbo-machinery components such as the draft tube, impeller and casing. Results of the simulation are in good agreement with the experiments performed at the University of Naples “Federico II”.

The penultimate research is performed on a proportional spool valve. The study demonstrates that the proposed three-dimensional CFD methodology can be applied to valves. Using a computational fluid dynamics (CFD) technique with an accurate turbulence model, it is possible to improve the internal geometry of valves to reduce internal flow vorticity. The models have been validated using experimental data from the hydraulic laboratory of the University of Naples. The experimental layout is an innovative configuration to measure spool torque.

The last study is concerned with the optimization of a two-way pressure compensated flow control valve. The goal is to reduce fluid-dynamic forces. During operation, the flow causes forces on the spool. These forces must be correctly balanced. Since these forces cannot be measured, a three-dimensional CFD modeling approach is needed. The final geometry was modeled, prototyped and tested. A comparison with experimental data shows good agreement with a maximum error of 3%. The model was adopted to make several analyses of velocity contouring, streamlines trends, and pressure distribution in the fluid volume. The modeled and tested results achieved the expected performance confirming the effectiveness of the methodology.

2.1 Hydro - Mechanical Transmission

2.1.1 Introduction

The three dimensional CFD modeling technique shown has been applied for the study of a novel vane pump power split transmission patented by the Australian company "The Mathers Hydraulics®". The vane pump is a double-acting vane pump with a floating ring. By coupling the floating ring to an output shaft, the vane pump becomes a hydrostatic transmission. The focus of this research is the optimization of the vane pump analyzing the internal fluid dynamics of each part during the pump operation and redesign. The study is a result of collaboration between the University of Minnesota and the University of Naples "Federico II" research groups. The universities involved in this project worked in close cooperation on these simulations. A prototype pump will be tested on a hydraulic test bench at the University of Minnesota, and the experimental data will be used to validate the simulation model.

After an introduction on the application of the vane pump power split transmission and a comparison with the other technologies applied for the vehicles transmission the pump will be deeply studied. Then the model will be shown with its results. By the end, thanks to the application of the bond graph theory, it will be shown the results of the study made to estimate the pump efficiency.

2.1.2 Hydro - Mechanical Transmission (HMT)

The demand for low emissions and better fuel economy requires increased vehicle drive system efficiency. This creates opportunities to integrate new technologies to achieve better performance and efficiency [12 - 13]. The automatic transmission is a widely acceptable solution but it is unable to maintain high efficiency over the entire engine operating range. In contrast, a Continuously Variable Transmission (CVT) can decouple the engine speed from the wheel speed, making the engine run more efficiently by using a hydrostatic transmission consisting of a hydraulic pump driving a hydraulic motor. By changing the displacement of either unit,

a variable transmission ratio is created. The hydrostatic transmission (HST) has been widely used in off-road machinery for agriculture, construction and forestry.

With a continuously variable transmission (CVT) and energy storage, full engine management becomes possible. The high power density of the hydraulic powertrain reduces vehicle weight, and allows regenerative braking and faster acceleration. The world's first series hydraulic hybrid delivery vehicle from the EPA has 60-70% better fuel economy and reduces CO_2 emissions by 40% or more. Altair's series hydraulic hybrid city bus delivers 30% better fuel efficiency than other diesel-electric buses available today. Nevertheless, the inefficiency of pumps and motors at low displacement dramatically reduces the transmission efficiency. Combining a Hydro Static Transmission (HST) and a gearbox in one unit, the hydro-mechanical transmission (HMT) has the advantages of both, the continuously transmission ratio of an HST and the high efficiency of a gearbox. Since the power is transferred though both the mechanical path and hydraulic path, it is also called a power split transmission. Although an HMT is more efficient than an HST, the transmission is more bulky due to the planetary gear set. Therefore, a more compact and cost-effective power split transmission is needed. The Vane Pump Power Split Transmission (VPPST) functions much like a conventional power split hydro-mechanical transmission (HMT) but without the planetary gear. It consists of a Vane Power Split Unit (VPSU) and a variable displacement hydraulic motor.

The three dimensional CFD analysis of a novel vane pump power split transmission (VPPST) is the first application components optimization presented in this thesis. The study, as already said, is a result of a collaboration between the University of Minnesota (USA) and the University of Naples "Federico II" research groups. In particular, the study is focused on the fluid-dynamic optimization of the Vane Power Split Unit (VPSU) that is part of the (VPPST). The VPSU is a double-acting vane pump with a floating ring. The input shaft of the VPSU is connected to the engine and the floating ring is connected to the output shaft. The combination of the VPSU and the hydraulic motor creates the VPPST. The VPSU generates hydraulic oil

flow proportional to the difference in angular velocities between the input and output shafts. This flow enters a hydraulic motor mounted to the output shaft. The Input shaft of the VPSU is directly coupled to the engine and the output shaft, fixed to the floating ring, is connected to the drive train (see figure 2.1).

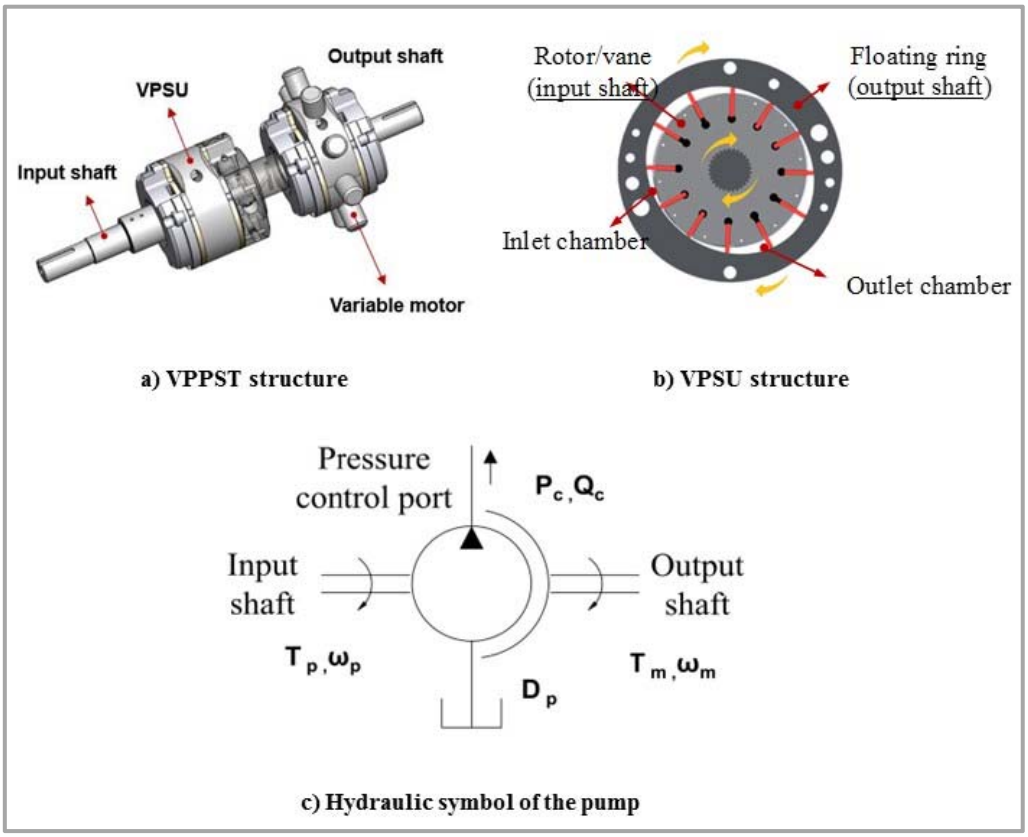

FIGURE 2.1: THE VPPST AND VPSU STRUCTURES AND THE HYDRAULIC SYMBOL OF THE PUMP

The exploded view of VPSU is shown in figure 2.2.

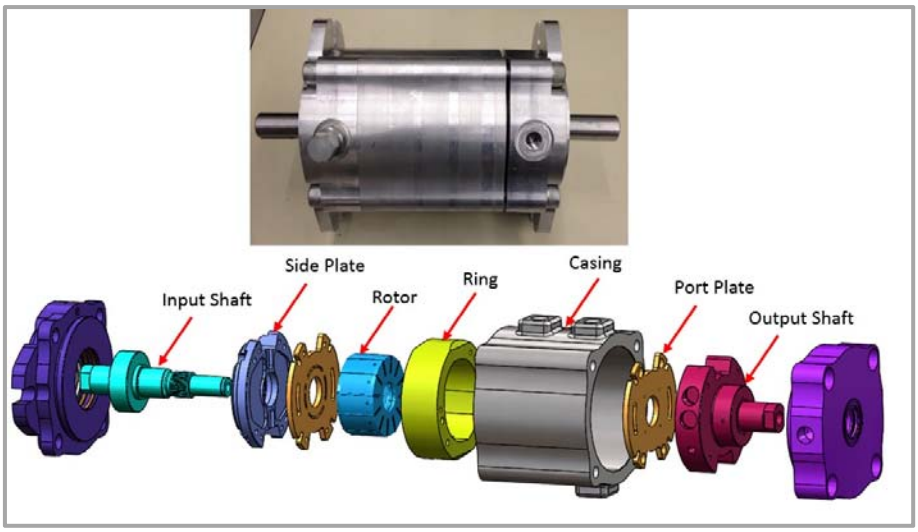

FIGURE 2.2: EXPLODED VIEW OF THE VPSU

Unlike a HST, where the transmission ratio can be adjusted by changing the displacement of the pump, motor, or both, in a VPPST, the transmission ratio is adjusted by controlling the displacement of the motor thus affecting the pressure of the control port of the VPSU.

The key component in this design is the VPSU that splits power into a hydraulic path to run a variable displacement motor and a mechanical path to rotate the output shaft of the VPSU. The power sharing between mechanical path and hydraulic path is controlled by the hydraulic motor displacement [12 - 14]. The hydraulic power is then added to the drive shaft to amplify the torque. The schematic of power split transmission is shown in figure 2.3. When the control flow is zero, the input and output shafts lock up at the same rotational speed. The VPPST is studied using a three-dimensional CFD approach to investigate the internal fluid dynamics.

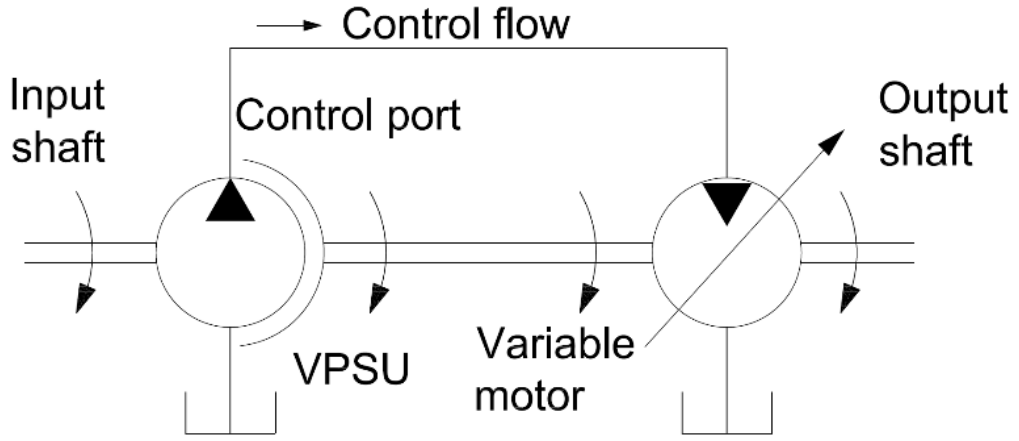

FIGURE 2.3: SCHEMATIC OF POWER SPLIT TRANSMISSION

The input shaft of the VPSU is connected to the IC engine and the output shaft is connected to the differential. The differential ratio is used to obtained the desired wheel speed and wheel torque from the engine. The appropriate differential ratio is important to sizing the pump and motor.

The Vane Power Split Unit (VPSU) has another attractive feature, an integral clutch. For each vane there is a pin driving a ball. By providing pilot pressures to these pins, the vane can be fully retracted (see figure 2.4), decoupling the output shaft from input shaft. The parasitic loss in the clutch is mainly the viscous drag on the rotor and

is very low. In the future, the integral clutch system will be studied by using the same CFD modeling approach presented here.

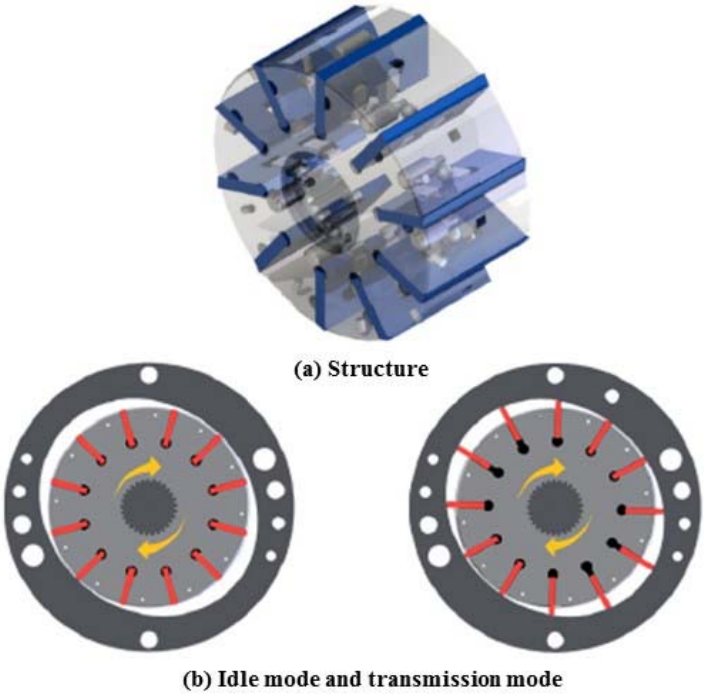

FIGURE 2.4: CLUTCH FUNCTION OF THE PRESSURE-CONTROLLED HYDRAULIC TRANSMISSION

The project is aimed at optimizing a vane pump power split transmission based on the floating ring vane pump invented by the Australian Company, "Mathers Hydraulics®"

An accurate model of all the pump has been built by the technique already described in the first chapter of the thesis.

The model based on preliminary pump geometry has been simulated to better understand component performance analyzing, in particular, forces acting on the ring. Then, thanks to collaboration with the code developers, the model has been implemented in order to predict the complex fluid dynamics in the pockets in the rotor into which the vanes retract. These pockets are referred to as under vane volumes.

2.1.3 Vane Pump Power Split Unit

The VPSU is based on a double-acting vane pump, meaning that it intakes and discharges oil symmetrically from two pumping chambers. Since it has a balanced design, it has smaller bearings, a longer lifetime and quieter operation than a gear or

piston pump. The rotor with the vanes is coupled to the input shaft and the floating ring is coupled to the output shaft.

The control flow at the control port,Q_c, is determined by the relative rotary speed between the input and output shaft:

$$Q_c = (\omega_p - \omega_m) D_p \eta \quad (2.1)$$

where ω_p and ω_m are the input and output shaft speeds, D_p is the pump displacement, $\eta = f(p_c, \omega_p - \omega_m)$ is the volumetric efficiency of the transmission, which is pressure and relative speed dependent, and p_c is the control pressure at the control port.

The power equation for the VPSU is:

$$T_p \omega_p = T_m \omega_m + p_c Q_c \quad (2.2)$$

The mechanical and volumetric efficiencies of the unit can be found by analyzing the equivalent unit shown on figure 2.3. The details are given in [12 - 14]. The characteristics of VPSU will be determined in upcoming experiments, but experimental results on fan drives give some indication of the potential for energy saving. These experiments show that the input power of the VPSU is nearly 20% lower than with a conventional vane pump given the same output fan speed and torque.

By increasing the control pressure to a high level, the control flow becomes zero and the input and output shafts have same rotational speeds. This lock up function creates an efficient direct drive for high speed.

2.1.4 Three - Dimensional CFD Model

Some studies have been conducted on conventional double-acting vane pumps. A theoretical analysis on the mechanical efficiency of a double-acting vane pump is presented in [15 - 20], with the focus on the friction torque reduction through both the parameter design and the structure optimization. Other researchers have investigated the lubrication mode of the line contacts between the vane tips and the cam ring in a balanced vane pump [17], [20]. An analysis of the force and torque applied to the cam

ring, shaft and the vanes in a single-acting variable displacement vane pump was also done [14]. Although these studies are based on conventional vane pumps, the friction and torque analysis between the vane and the cam ring gives a good understanding on how the presented pump works.

Using a three-dimensional CFD approach it is possible to predict the torque. The model used for this prediction is now described.

The CFD 3D model takes into account all forces acting on the control ring depending on the operations condition. For this reason it is able to well predict the rotation of the pump's ring and consequently the VPSU's output power.

In table 1 the main fluid characteristics are reported. The fluid used for simulations is an ISO VG 46 (ASTM D455, 44.2 cst at 40°C and 6.65cst at 100°C).

WORKING FLUID	**MOBILE DTE™**
Density	876kg/m^3
Temperature	40°C
Viscosity	0.031Pa·s
Saturation Pressure	400Pa
%Air	2%

TABLE 2.1: FLUID PROPERTIES

The complete model, shown in figure 2.5, consists of about 1,000,000 three-dimensional cells.

Simulations have been run on a multi-core Windows® 64bit PC (CPU E5–2640, 64Gb RAM). For all simulations, it was necessary to run for three complete revolutions to achieve numerical regime conditions with a computational time of 27h for each point. For this study, it was assumed that there is always a constant gap between the tip vanes and the ring.

FIGURE 2.5: VANE PUMP POWER SPLIT TRANSMISSION FLUID VOLUME MESH

After mesh generation, a large number of simulations have been run to obtain the pump characteristic map for each geometry. In figure 2.6, the first result of the 3D model is shown.

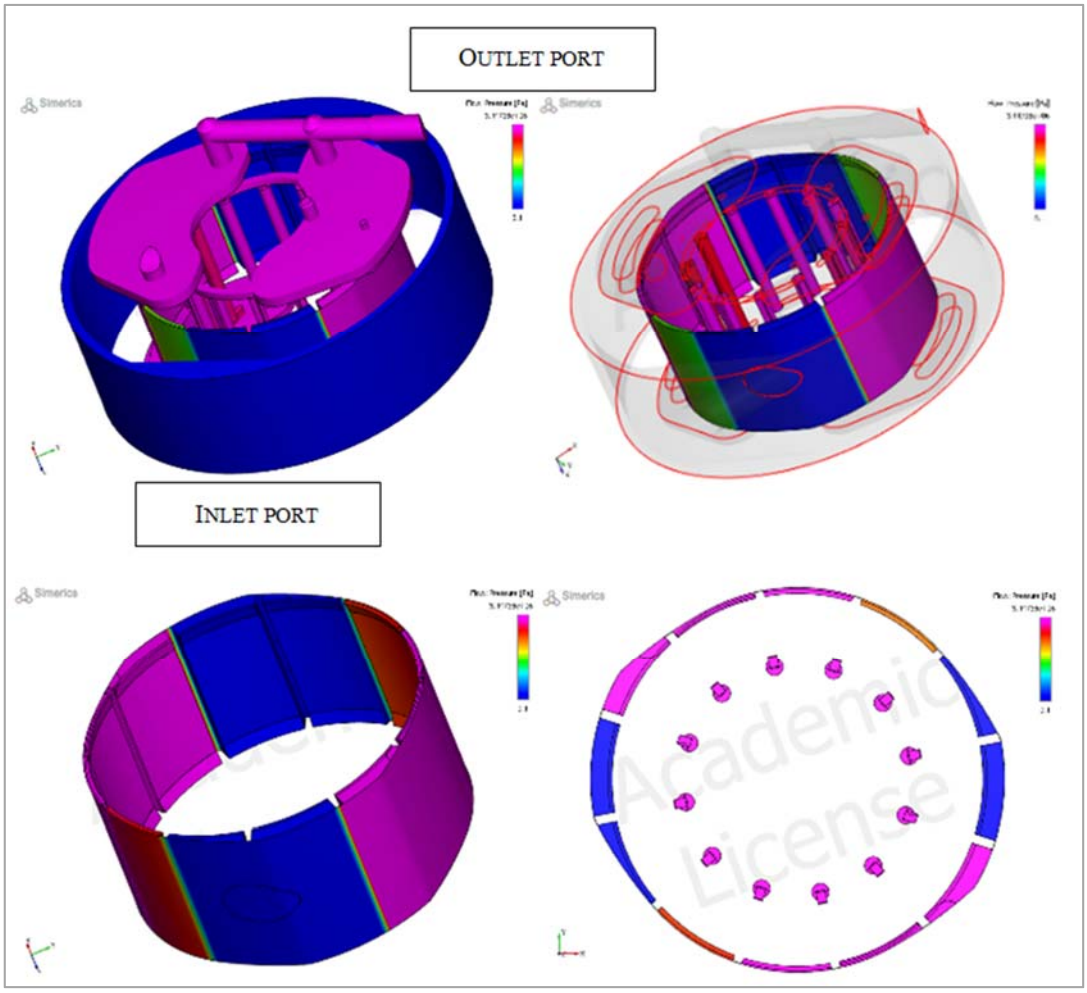

FIGURE 2.6: PRESSURE DISTRIBUTION IN THE FLUID VOLUME

It is possible to visualize the oil pressure distribution inside the pump fluid volume for the following operating conditions:

- Input Pump Speed of 2400 rpm,
- Output Pump Speed range of 0 - 2400 rpm,
- Oil temperature of 40°C,
- p_{inlet} of 1bar.

Figure 2.6 shows the fluid volume colored as a function of the pressure. As shown in the graduate scale in the top right corner the dark blue areas are the low-pressure areas, while the magenta areas are the high-pressure areas.

Since the pump is double acting, there are two areas of high pressure and two areas of low pressure. The suction port in the outer housing is fixed and is not visible in figure 2.6. However, the suction duct in the floating ring rotates at the same speed as the unit's output shaft and is connected to the suction port through the port plate. The top area (top left corner of the figure 2.6) is the delivery port. This fluid volume is directly connected to both high-pressure chambers by the port plate. The picture in the bottom right corner of figure 2.6 highlights the bottom side of the vanes. These fluid volumes are inside the rotor and rotate at the inlet shaft speed.

The model takes into account of the vane tip profile. This application has been developed in close collaboration with the simulation code developers. This sub-model has been included in the model to study the effect, in term of efficiency, on performance of the pump. In figure 2.7 the real profile of the tip of one vane is shown. As know, the choice of the vane tip is important in order to minimize the leakage through the area underlined with the red circle in figure 2.7, without increasing friction.

Defining the average cam radius as:

$$R = \frac{R_1 + R_2}{2} \tag{2.3}$$

The torque due to the friction between the vane tip and the cam contour can be obtained as shown in the following equation:

$$T_n = F_t R \Delta p z \tag{2.4}$$

Where z is the number of vanes and F_t is the friction force of the vane shown in figure 8. The reduction of the torque is crucial to improve the performance of the pump.

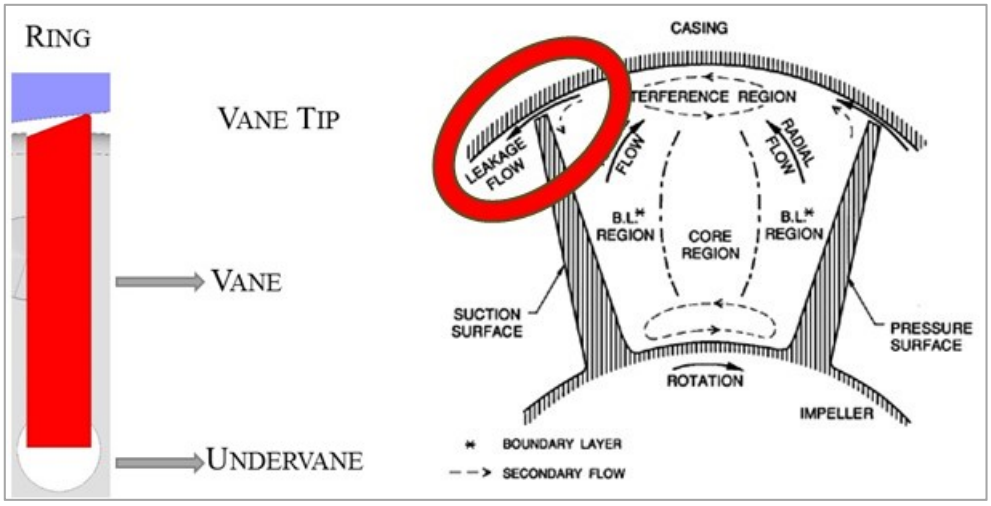

FIGURE 2.7: STUDY OF THE TIP OF VANES

As already shown by Inaguma at all. [16 - 18], the efficiency of a vane pump is function of the correct balance of the pressure acting on the bottom and tip of the vane and the force F_v caused by the pressure difference in the small radius region (1) suction (2), large radius (3), and delivery (4). This force F_t, therefore, depend by the position of the vane during the rotation. The value of this force changes as shown in figure 2.8.

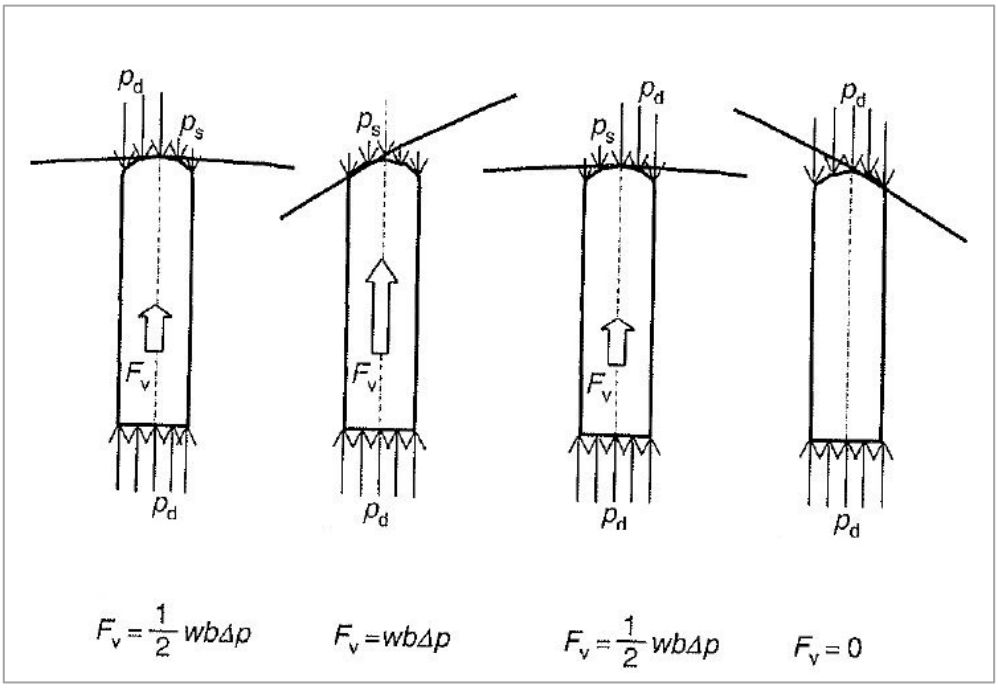

FIGURE 2.8: VANE FORCE AT EACH PART

In the transaction areas (1) and (2), (connection inlet→outlet and vice versa) the force F_v is almost the same, while is maximum in the position (2) in figure 2.8.

When the vane is located in the suction part, the pressure p_i acts on the entire vane and vane bottom. When the vane is connected to the delivery port the pressure p_o constantly acts on the vane bottom and on the tip of the vane. Undervane areas are volumes connected through ducts and kidneys to the delivery and suction ports as shown in figure 2.9.

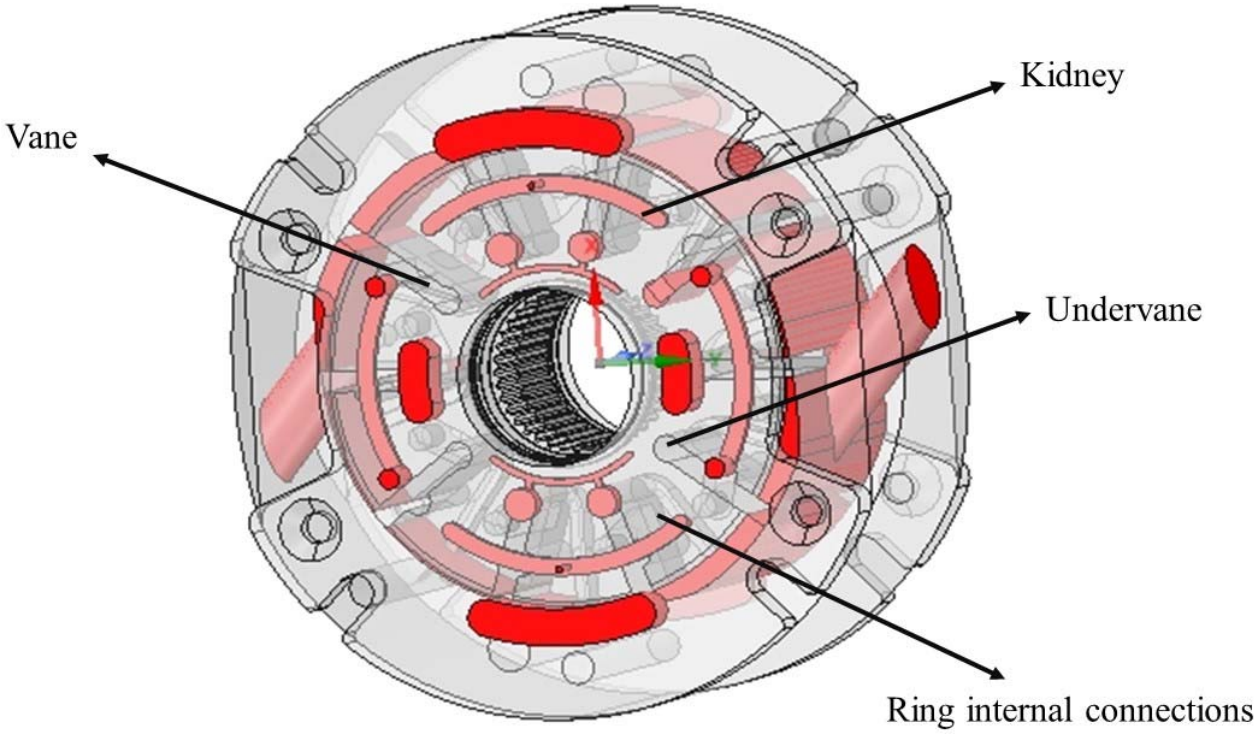

FIGURE 2.9: UNDERVANE CONNECTION WITH PORTS

The final profile of the vane is clearly shown in figure 2.7. This profile is finally introduced in the CFD 3D model as shown in figure 2.10.

Thanks to collaboration with the code developers, the model is now able to predict the complex fluid dynamics in the pockets in the rotor into which the vanes retract. These pockets are referred to as under vane volumes. The rotor of the vane pump, in fact, has several internal channels that connect the pumping chambers between the vanes to the under vane volumes (see figures 2.9 and 2.10). The combination of the vanes and the internal ducts and volumes of the under vanes have

been modelled as dynamic valves that rotate with the rotor. Radial movements of the vanes are computed as a part of the simulation, based on the pressures due to the compression of the volumes on the inner diameter side of the vanes.

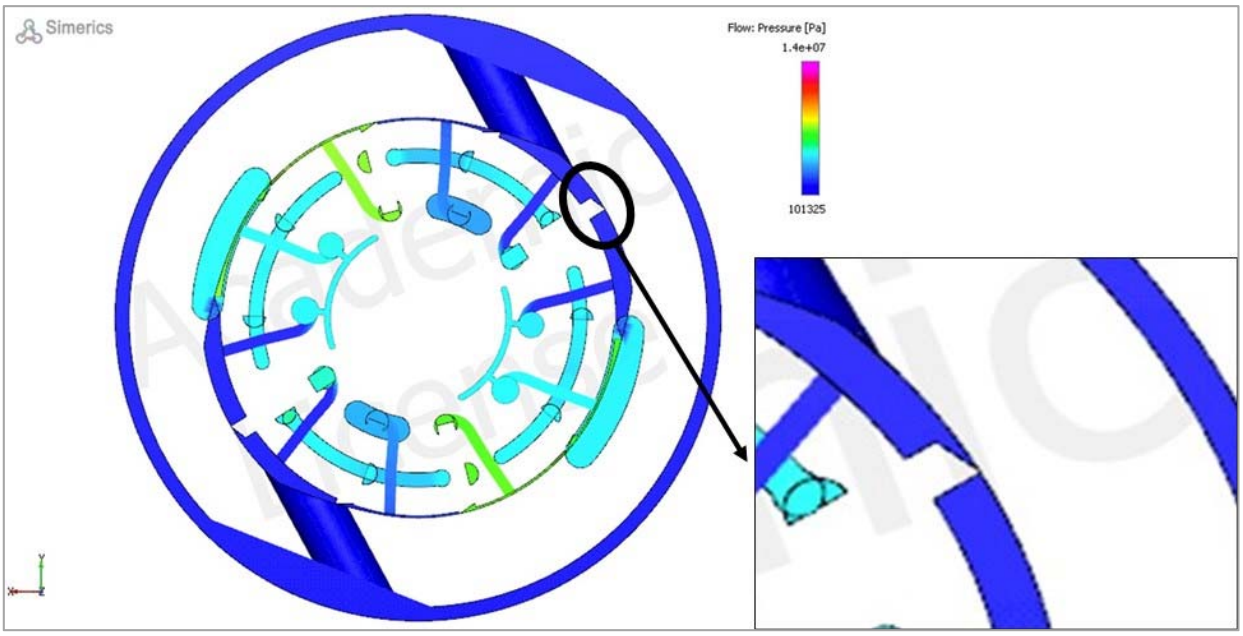

FIGURE 2.10: MODEL RESULTS – PRESSURE DISTRIBUTION IN THE FLUID VOLUME

Thanks to the implementation of the dynamic valve sub-model, the fluid-dynamic force acting on bottom of the vane is evaluated as result of a force balance. In this way it is possible to evaluate the force F_v:

$$F_{model} = \sum F_{pressure} + \sum F_{shear} \qquad (2.5)$$

The next step of this research concerns the application of the same function for the tip of the vane and the ring. In this way, the vane position inside the ring will be an output of the model and, consequently it will be possible to estimate the gap between vanes and ring that is very difficult to measure.

Simulations has been run in different operating conditions and all the results are shown in the following sub-paragraphs.

2.1.5 Power Transmission Study: The Variation of Speed

Using the model is possible to evaluate the output power available on the outlet shaft of the VPSU. In figure 2.11 the output power ripples function of the shaft position are shown at different outlet shaft speeds. The input speed is fixed at 2400 rpm.

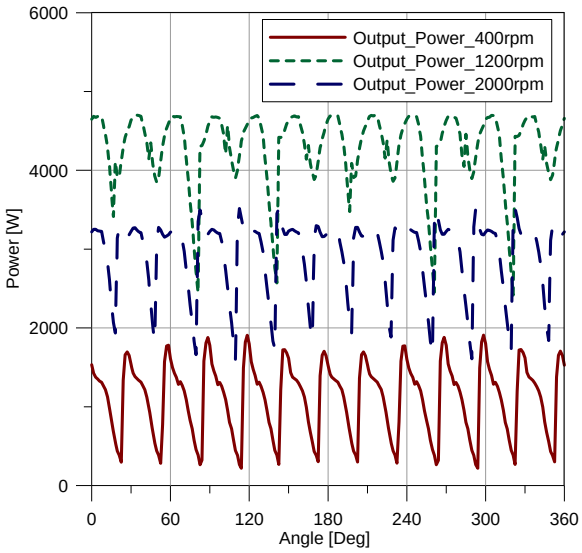

FIGURE 2.11: OUTPUT POWER COMPARISONS AT DIFFERENT OUTPUT SHAFT SPEEDS

The difference in shaft speeds influences the average output power value. When the difference between the speed of the input and the output shafts is high, the average output power is lowest while the ripples are greatest. Growing from 400 rpm to 2000 rpm oscillations' amplitude decreases by 15%. The graph confirm that the output power reduction increased by increased leakage.

At the same way analyzing the figure 2.12 the inlet power ripples varies from 2kW to 10kW at low shaft output speed (400 rpm). This effect is less present where the output shaft speed is near to the inlet shaft speed, for example, with an outlet speed of 2000 rpm. In this case the unit's power request is almost constant.

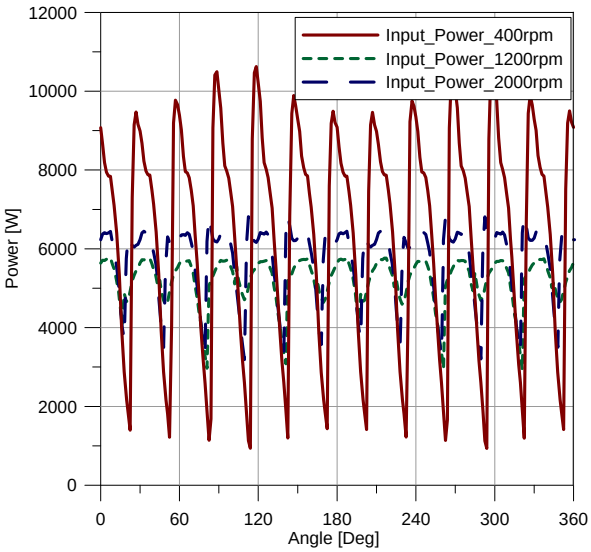

FIGURE 2.12: INPUT POWER COMPARISON AT DIFFERENT OUTPUT SHAFT SPEED

Figure 2.12 shows the inlet power required by the pump varying the output shaft speed.

From the results in figures 2.11 and 2.12 it is clear that increasing the speed difference between the input and the output shafts decreases the output power while keeping the input power almost constant.

Using the model, other analyses were made by changing the delivery pressure. The effect on the power is shown in figure 2.13, where the comparison between the input powers and the output powers is presented for two delivery pressures: 103.4 and 34.5 bar. In these simulations, the input shaft speed is 2400 rpm and the output shaft speed is 2000 rpm. As expected, by increasing the delivery pressure, the input and output powers increase and the ripples also increase.

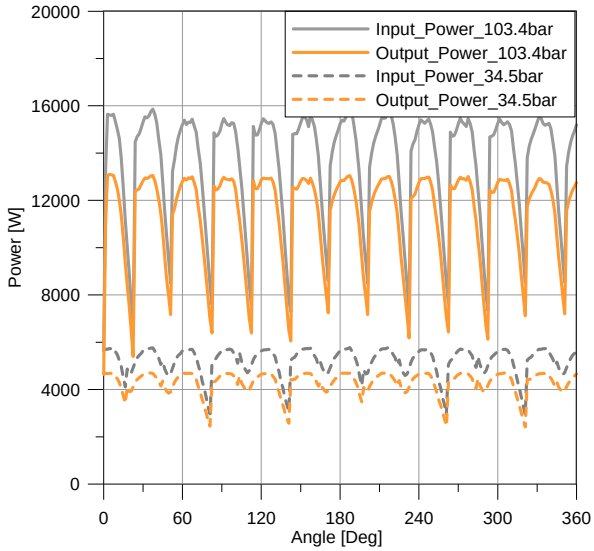

FIGURE 2.13: POWER COMPARISON AT DIFFERENT OUTPUT PRESSURE

2.1.6 Power Transmission Study: Variation of Gap Height

Using the model the influence of the gap height between the tip vanes and the ring on the output power has been analyzed. The following figures present results obtained by changing the output shaft speed in the range of 400 to 2000 rpm.

There following gap conditions were studied:

- No gap between the tip of vanes and the ring (tangent surfaces)
- Medium gap of 0.01mm
- High gap of 0.037mm.

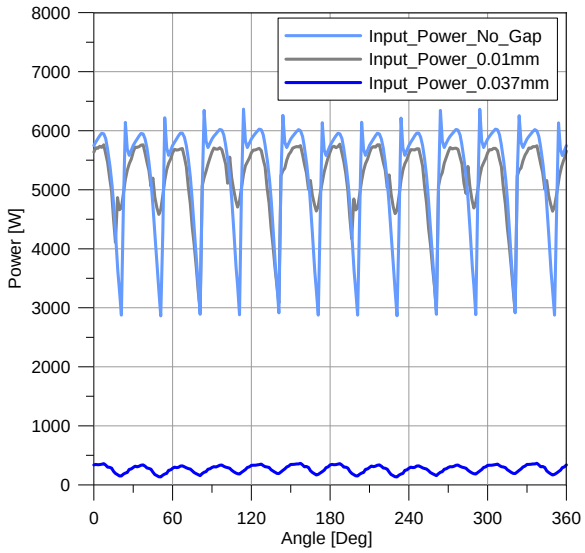

FIGURE 2.14: INPUT POWER AT DIFFERENT GAP HEIGHTS

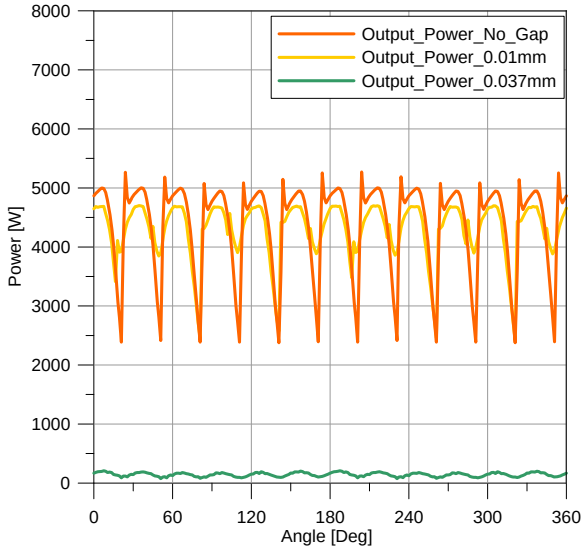

FIGURE 2.15: OUTPUT POWER AT DIFFERENT GAP HEIGHTS

Figure 2.14 and 2.15 demonstrate the high influence of this parameter on the pump input power. To complete this analysis is important to investigate on the output power in the same operation condition (see figure 2.15).

To understand the gap's influence, in figure 2.16 the input and output power at 2000 rpm were compared directly for each case. These pictures show as the powers decreases from zero height (case 1) to maximum gap (case 3). Both input and output power decrease with increasing gap. Thus, the case 3 power value is lower in comparison with the other two analyzed gaps. Therefore the last graph in figure 2.16 has the power axis zoomed in the range of zero to 400W.

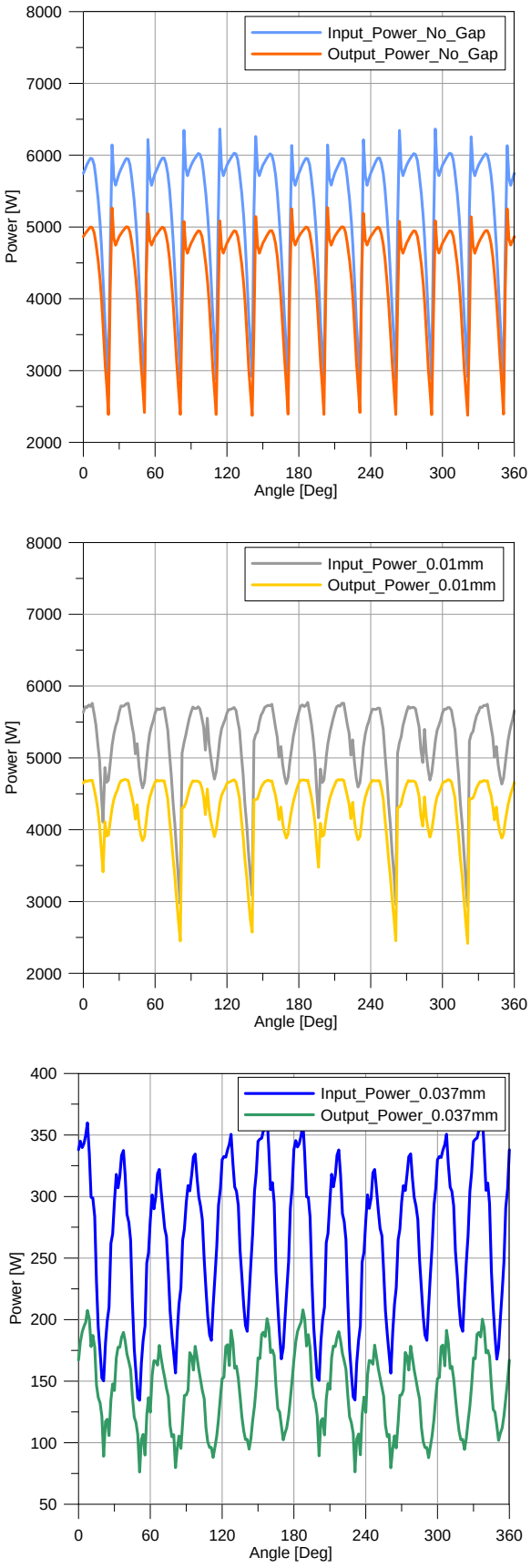

FIGURE 2.16: COMPARISON INPUT POWER WITH OUTPUT POWER AT 2000RPM

In figure 2.16 it is possible to note that power ripple amplitude is high for the case with no gap while it decreases for case of the maximum gap height (case 3).

Figures 2.17 – 2.19 present results made on each studied case changing the speed of the output shaft. The speed of the inlet shaft has been fixed at 2400rpm. These graphs confirm the results presented in figures 2.11 and 2.12.

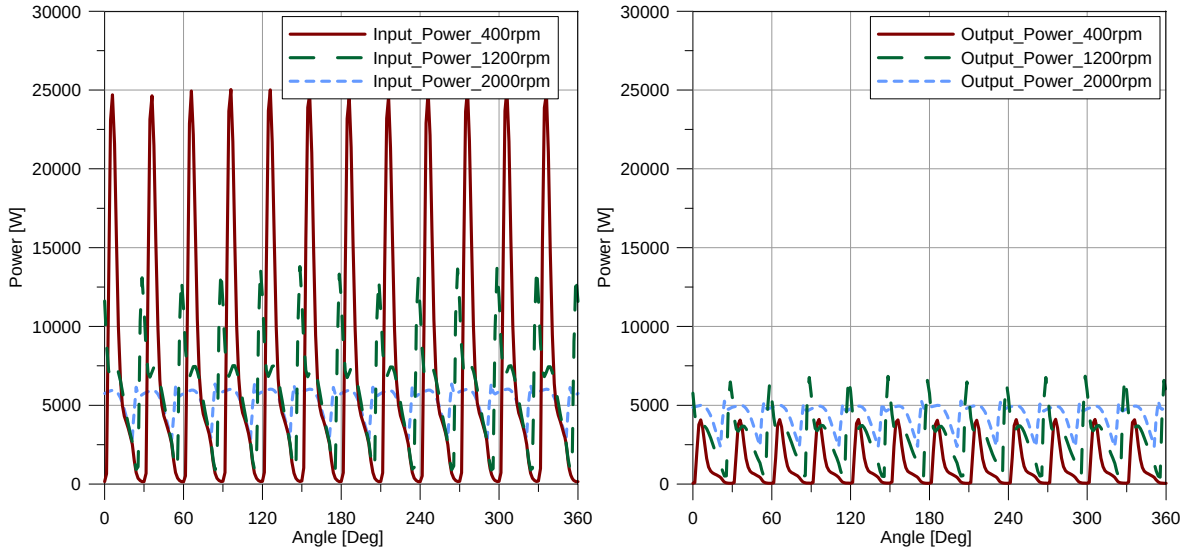

FIGURE 2.17: POWER AT DIFFERENT SHAFT OUTPUT SPEED – NO GAP CASE

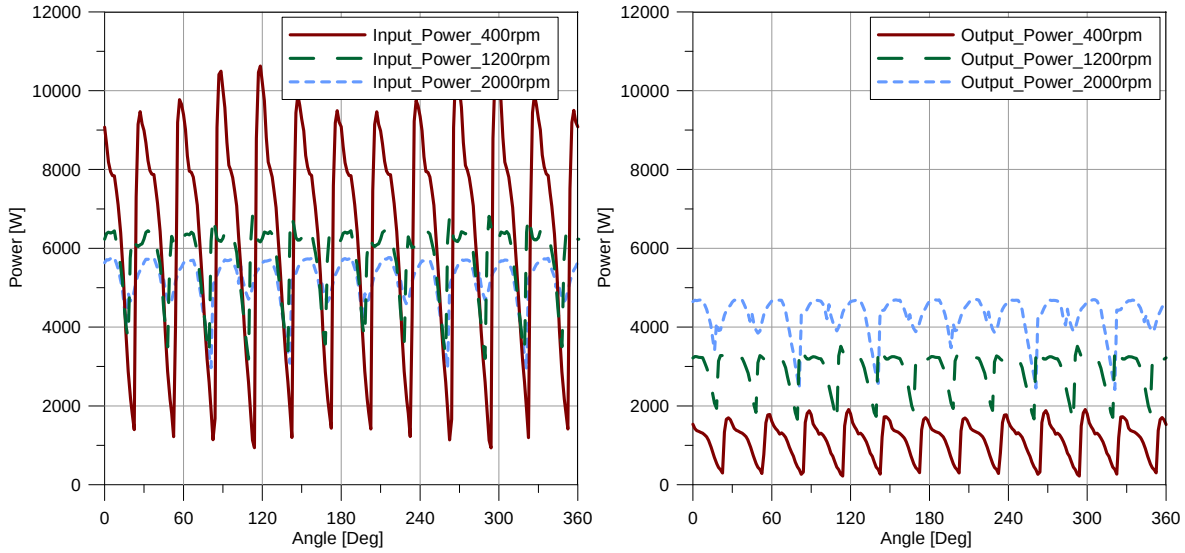

FIGURE 2.18: POWER AT DIFFERENT SHAFT OUTPUT SPEED – GAP 0.01MM CASE

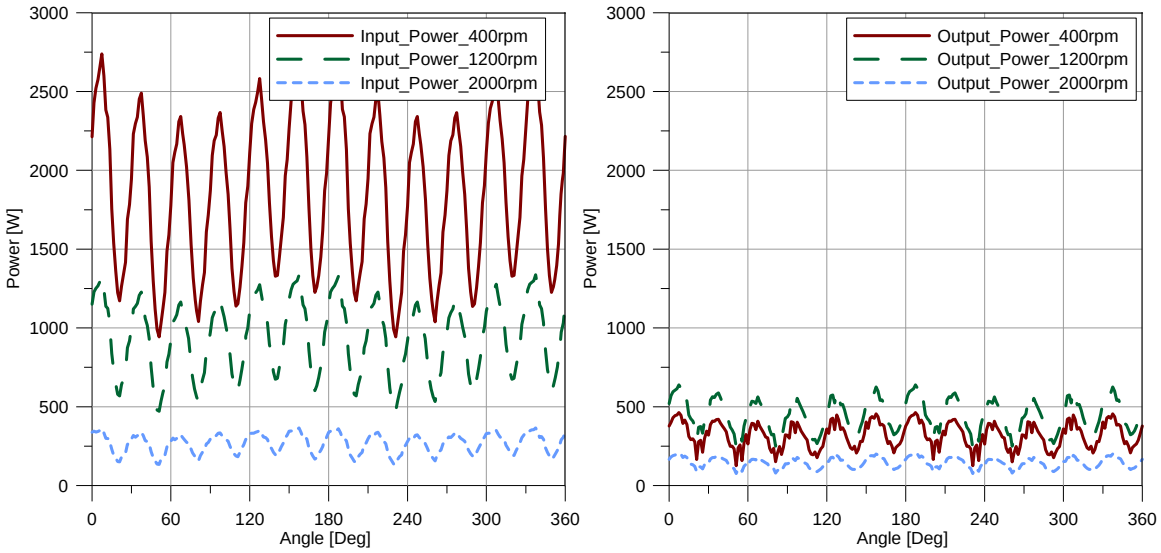

FIGURE 2.19: POWER AT DIFFERENT SHAFT OUTPUT SPEED – GAP 0.037MM CASE

By changing the output speed, it is possible to see that the pressure ripple of the input power decreases. These graphs confirm that increasing the speed difference between the inlet and outlet shafts, amplifies the input power ripples and decreases the output power.

Therefore, this first analysis of the pump has confirmed that by increasing the gap, and consequently the leakage, the output power decreases.

Starting from the first already described analysis, the research has been continued with the goal to understand the efficiency of the VPSU under varying conditions. The CFD model can be used, in absence of experimental data, to evaluate the unit efficiency varying delivery pressures of the pump and displacement ratios. Bond graph theory facilitates an understanding of the impact of VPSU efficiency from these results on overall VPPST efficiency.

The analysis through the bond graph theory approach has been made to identify the variable of input to set and the consequent outputs of the model. In this way, the input parameters to set as boundary conditions for the simulations have been identify in function of requested output of the model.

The input for the code are the inlet of the velocity of the shaft and the pressure at the input and output ports.

The HMT can be schematize like in figure 2.20.

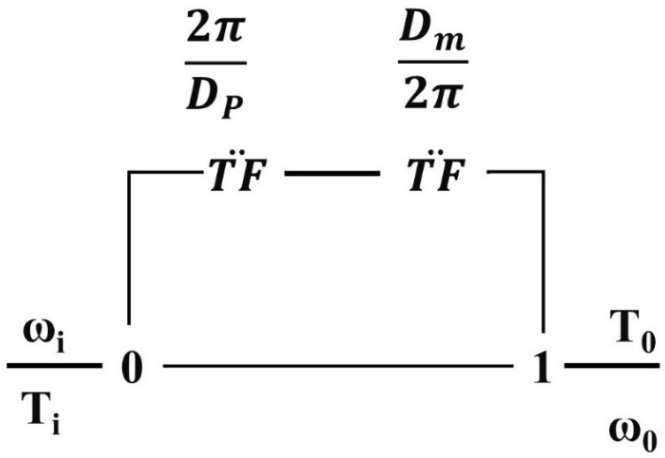

FIGURE 2.20: HMT BOND GRAPH MODEL

Where D_m is the hydraulic motor displacement, D_p is the vane pump displacement, T_i and ω_i are respectively the inlet torque and the angular velocity at the inlet shaft (pump inlet) while T_o and ω_o are respectively the outlet torque and the angular velocity at the outlet shaft of the HTM.

Two transformations in figure 2.20 can be unified by defining the displacement ratios r as:

$$r = \frac{D_m}{D_p} \tag{2.6}$$

In this way the bond graph in figure 2.20 changes and becomes the graph in figure 2.21:

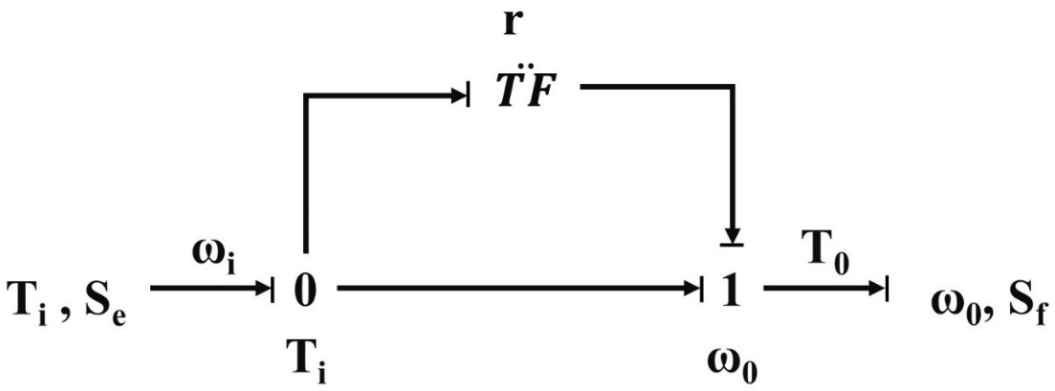

FIGURE 2.21: HMT BOND GRAPH MODEL

From equation (2.4), it is possible to define the outlet torque and angular velocity as function of the displacement ratio defined in equation 2.6.

- $T_o = (1 + r)T_i$ (2.7)

- $\omega_i = (1 + r)\omega_o \quad \rightarrow \quad \omega_o = \frac{1}{(1+r)}\omega_i$ (2.8)

Defined the torque at the inlet and outlet shaft of the transmission the power can be expresses as:

$$P = \frac{2\pi}{D_m}(T_o - T_i) \tag{2.9}$$

but the power is also equal to:

$$P = \frac{2\pi}{D_p}T_i \tag{2.10}$$

then:

$$P = \frac{2\pi}{D_m}\left(T_o - \frac{2\pi}{D_p}P\right) = \frac{2\pi}{D_p}T_o - \frac{P}{r} \qquad \rightarrow \qquad P\left(1 + \frac{1}{r}\right) = \frac{2\pi}{D_m}T_o$$

$$\rightarrow \qquad P = \frac{\frac{2\pi}{D_m}}{\left(1+\frac{1}{r}\right)}T_o = \frac{2\pi T_o}{D_p}\frac{\frac{1}{r}}{1+\frac{1}{r}} \tag{2.11}$$

and consequently:

$$P = \frac{2\pi}{D_p}\frac{T_o}{r+1} \tag{2.12}$$

From equation 2.12, it is possible to express the outlet torque as function of the power P, the displacement of the pump D_p and the displacement ratio r. Infant T_o is equal to:

$$T_o = \frac{P(1+r)}{2\pi}D_p \tag{2.13}$$

Multiplying both terms of the equation 2.13 for the outlet angular velocity ω_o (defined in equation 2.8), it is possible to define the output power:

$$T_o\omega_o = \frac{PD_p\omega_i}{2\pi} \tag{2.14}$$

The output power of the transmission function of the D_p , r, P and ω_o.

The volumetric efficiency of the VPSU can be defined as:

$$\eta = \frac{P_o + P_{flow}}{P_i} \tag{2.15}$$

Where P_{flow} is the power due from the hydraulic path.

Simulations have been run to evaluate the efficiency of the transmission as function of the displacement ratio and the outlet pressure. The graph in figure 2.22 shows the efficiency behavior.

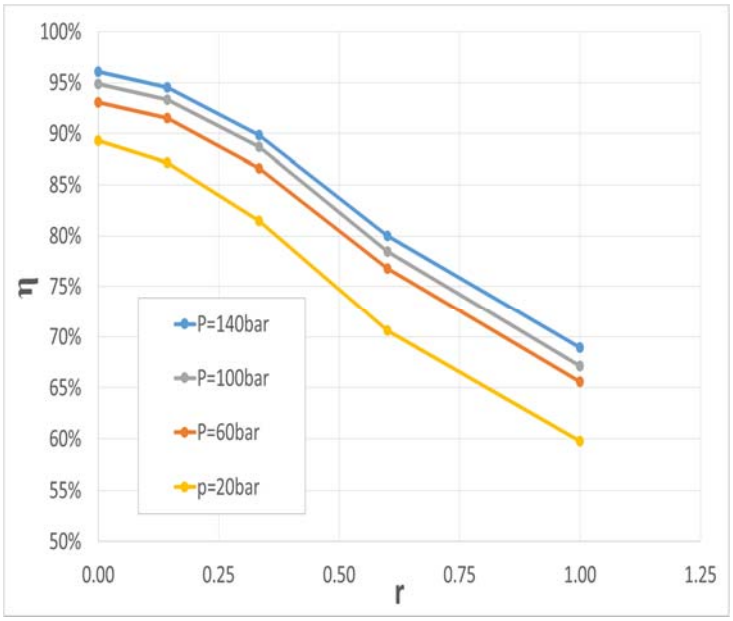

FIGURE 2.22: EFFICIENCY OF THE VPSU

When the inlet velocity is equal to the outlet one the displacement ratio is zero, in this case the VPSU efficiency varies in the range (89 ÷97) % in function of the pressure at the output port. Increasing the pressure the efficiency increases as well.

For $r = 1 \rightarrow \omega_o = \frac{1}{2}\omega_i$, the efficiency decreases to (60 ÷ 70) % which is low. Therefore, the collaboration between the universities is still in progress with the goal of the optimization of the geometries of each part of the pump like port plates, ports and of the profiles of the tip of the vanes and of the ring in order to improve the unit performance for $r > 0$.

The shown methodology has demonstrated to be very useful in the understanding of the performance of the VPSU in absence of experimental data.

2.2 Variable Displacement Vane Pump

2.2.1 Introduction

In this paragraph the study performed on a variable displacement vane pump will be shown. The application of a tridimensional CFD technique, in this case, is focused on the optimization of an oil pump of a modern high-performance engine.

The model has been built up with the commercial 3D CFD code PumpLinx® taking into account all the thermo-fluid dynamic conditions with particular attention to the cavitation phenomena.

In recent years, internal combustion engines have achieved the objective of high specific power output with low fuel consumption and low exhaust gas emissions.

Consequently, all engine components have to be carefully studied and designed from the early stages of their development. The oil delivery pump is, by all means, one of the components that can be analyzed to reduce mechanical power losses. The pump is known to require mechanical power proportional to its geometric displacement and the oil pressure on its delivery port, while its flow-rate depends on shaft velocity. In fact, the main drawback of fixed displacement pumps is power losses due to the flow-rate recirculation within the pressure relief valve, especially at high shaft rotational speed. Such an excess flow-rate is due to the pumps size selection process, which focuses on providing the necessary flow-rate at low regimes [3].

For this reasons a vane variable displacement oil pump has been adopted to reduce the torque needed to drive the oil pump. This type of pump is going to become a standard on engines because, as well known, using a variable displacement oil pump it is possible to reduce the vehicle fuel consumption by about 1 – 3%. The variable displacement oil pump is installed on a high performance engine to reduce the unnecessary power losses as well.

The activity described in this paragraph demonstrate that the methodology developed by the Engine Hydraulic Research Group of the Department of Industrial Engineering of University of Naples “Federico II” it can be adopted for several

application in the hydraulic field. The oil pump has been modeled with a CFD three-dimensional approach. The model has been validated by data of an experimental campaign performed on a hydraulic test bench of the manufacturer of the engine. The focus of the this study is to analyze phenomena which occur during the pump operation, as cavitation, to calculate the flow - rate limit during the eccentricity variations and, consequently, the displacement variation. Moreover, the model allows to determine the forces between the pump rotating elements which influence the equilibrium of the ring and consequently the displacement variation.

In this particular application, the variable displacement pump is used to optimize the operative conditions of the lubricant circuit in all engine-running conditions. This variable displacement pump changes the positions of the ring as a function of the boundary conditions.

The modeling methodology is an innovative solution because it is able to simulate the performance of the pump in a simplified manner to avoid adopting an onerous simulation tasks and undertaking experiments.

In fact, the vane pump cam ring moves according to the force balance to control the eccentricity and hence the flow - rate.

This model is able to simulate the dynamic of the oil pump. The simulation results will show the flow - rate variation as function of the engine speed. Then, the outlet pressure will been compared with experimental data performed by the manufacturer of the engine.

2.2.2 Variable Displacement Vane Pump

The oil pump (shown in figure 2.23) is composed by two main systems. The first one includes the vane, the rotor ring, the rotor and the control ring (slider); the second one includes all the components of the variable displacement system: the two springs, the hydraulic valve and the discharge bore.

The balance of the force on the control ring allows the displacement variation; the result is an optimization of the oil pressure and flow - rate by controlling the eccentricity.

FIGURE 2.23: PICTURES OF THE VARIABLE DISPLACEMENT VANE PUMP

The control ring is fixed at the maximum eccentricity position for low engine speeds. In these operating conditions the pressure and the flow - rate increases linearly with the engine speed while the pump efficiency decreases because some oil goes from the delivery pump to the suction side passing through the discharge bore.

When the oil pressure rises with the engine speed the slider moves to reduce the pump displacement.

If the oil pressure at the pump delivery goes over the set point value (typically 4 – 6 bar), the variable displacement system start to operate, depending on the force balance (see figure 2.24), since a new slider position is researched, which causes an oil flow - rate reduction.

The pump displacement variation depends by the following factors:

- Oil pump speed;
- Oil properties;
- Pump geometry;
- Pressure distribution;
- Cavitation.

The forces acting on the ring are shown in figure 2.24.

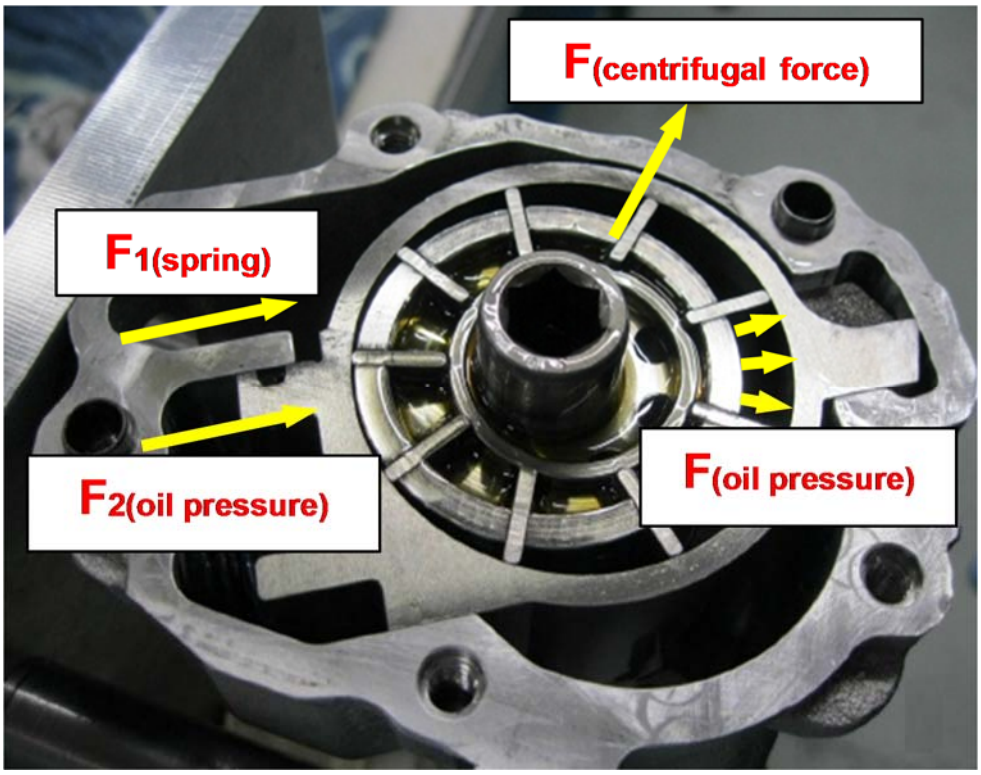

FIGURE 2.24: INTERNAL FORCE ON THE CONTROL RING

Forces F_1 and F_2 act in opposition of the other forces. From the figure 2.24 it is possible to visualize the influence of each force in the oil pump displacement variation.

By following, the performance of this oil pump, the simulation model, the comparison between the CFD 3D results and the experimental data results will be described.

2.2.3 Three - Dimensional CFD Model

The oil pump has been simulated with the commercial CFD program PumpLinx® (developed by Simerics Inc.®). From the pump 3D geometry, obtained by a reverse engineering operation, the fluid volume has been extracted. Then the obtained geometry has been meshed with the grid generator of the code [3] that, has already said, it uses the body-fitted binary tree approach.

Figure 2.25 shows the binary tree mesh in a section plane of the considered oil pump. In the boundary layer and in regions of high curvature and small details the binary tree approach can easily increase the grid density on the surface without excessively increasing the total cell count.

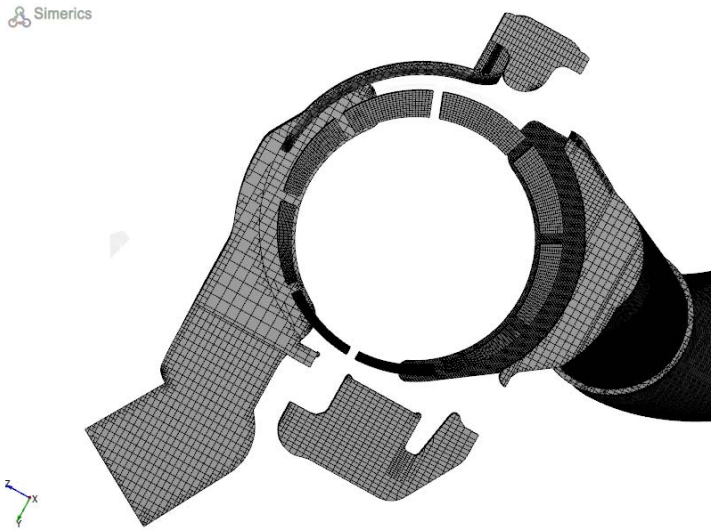

FIGURE 2.25: BINARY TREE MESH – PUMP CROSS SECTION

The code allows for the simultaneous treatment of moving (rotors) and stationary (intake and delivery ports) fluid volumes. Each volume connects to the others via an implicit interface.

As said, the model 3D CFD model takes into account all force acting on the control ring so, depending on the operations condition, it is possible to calculate the displacement variation.

In figure 2.26, the 3D CFD model is shown. Starting from the suction duct, the lubrication fluid enters in each vane of the suction area, is compressed and, finally, it is sent to the pump delivery.

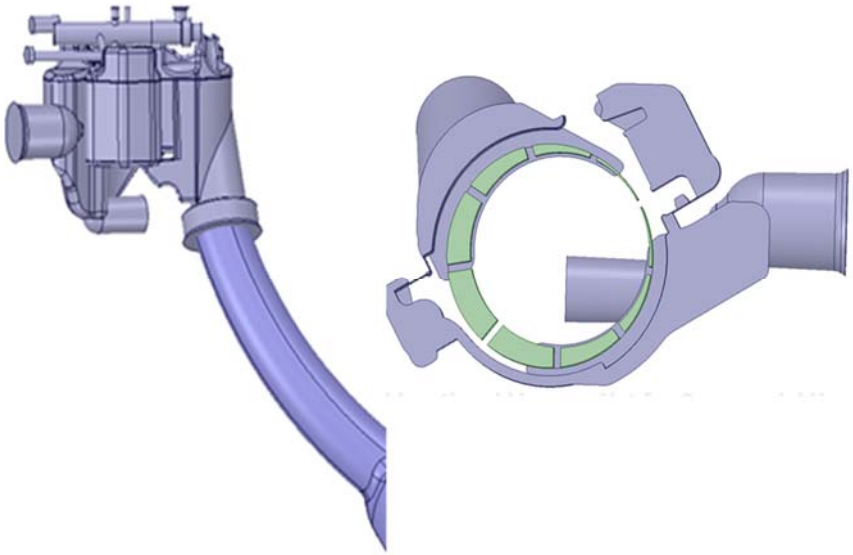

FIGURE 2.26: OIL PUMP FLUID VOLUME

In the oil pump model, the relief valve is also modeled (figure 2.27). The valve sends oil to the feedback branch of the lubrication circuit, allowing the oil pump displacement variation.

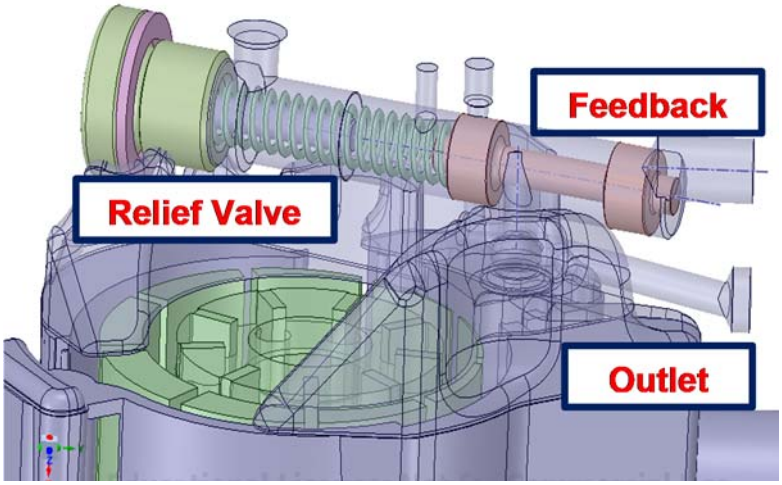

FIGURE 2.27: OIL PUMP RELIEF VALVE

The complete model, shown in figure 2.28, it consists of 3.552.466 3D cells. Transient simulations have been run on a multi-core Windows® 64bit PC (CPU Intel(R) Xeon(R) X5650, 12Gb RAM). For all simulations, it was necessary to run from 3 to 5 complete revolutions to achieve numerical regime conditions. Calculation times for each working point were always less than 5 hours.

FIGURE 2.28: FLUID VOLUME MESH

After model creation, a large number of simulations have been run to obtain the pump characteristics map. In figure 2.29, a first application result of the 3D model is shown. It is possible to appreciate the oil pressure distribution inside the pump fluid volume at 5500 rpm and at oil temperature of 114°C. The fluid volume is colored as function of the pressure distribution. The dark blue areas (pressure 1 bar) are the low-pressure areas, while the magenta areas (pressure 7 bar) are the pressurized areas. In figure 2.29 it is possible to observe the suction port.

FIGURE 2.29: PRESSURE DISTRIBUTION INSIDE THE FLUID VOLUME AT 5500RPM

2.2.4 Experimental Data

The below table one lists the fluid properties and operating conditions of the pump.

WORKING FLUID	**SAE 5W40**
Density	860kg/m^3
Oil Viscosity	0.01204Pa·s
Saturation Pressure	400Pa
Vapor Density	0.0245kg/m^3

TABLE 2.2: FLUID PROPERTIES AND PUMP OPERATING CONDITIONS

The experimental flow - rate data has been measured for different operating points. The engine speed varies from 1000 rpm to 7000 rpm.

In figure 2.30, the transducers position are shown:

1) Spring chamber;

2) Pump delivery;

3) Feedback channel.

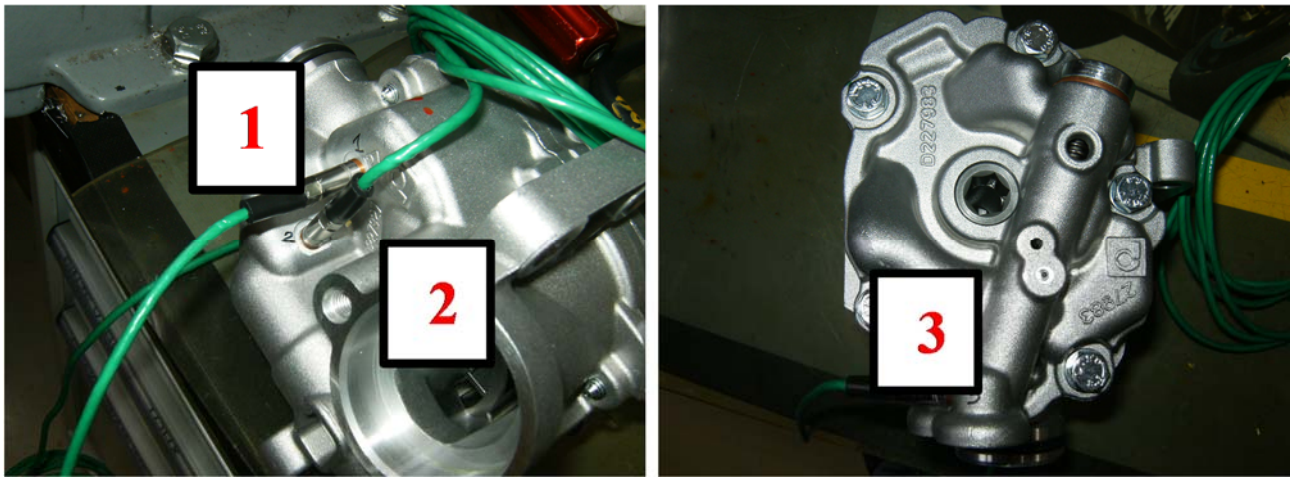

FIGURE 2.30: TRANSDUCERS POSITION

The tests have been made at different oil temperature (in °C) as shown in figure 2.31.

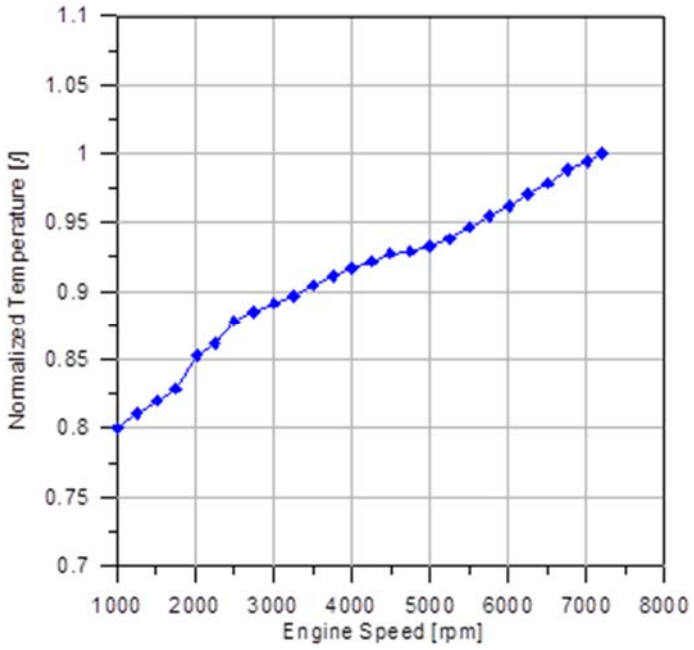

FIGURE 2.31: OIL TEMPERATURE VS RPM

It can be noted that the oil temperature increases with the engine speed, the oil pump model takes into account of this phenomena to have the best correlation with the experimental data.

Figures 2.32 and 2.33 show the data obtained by engine manufacturer on an engine test bench. In the first graph (figure 2.32), the eccentricity varying with the engine speed at 80°C of the oil temperature is shown.

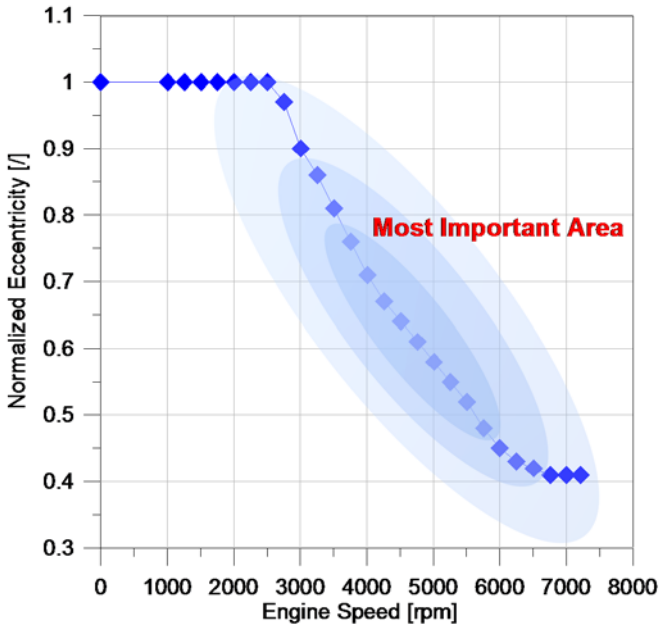

FIGURE 2.32: ECCENTRICITY VARIATION IN FUNCTION OF RPM

Analyzing the graph in figure 2.32 it can be seen that there is no eccentricity variation up to 2500rpm; increasing the oil pressure the control ring moves because the oil pressure force become greater than the spring force of the displacement control system.

Therefore, three areas can be identified in the graph, but the most important is located, the dark blue area, between 3500rpm and 5500rpm.

The eccentricity between the rotor and the control ring varies between 9% and 50% from the initial value where there is no variation (maximum eccentricity).

In figure 2.33, the trend of the pressure at the oil pump delivery is shown.

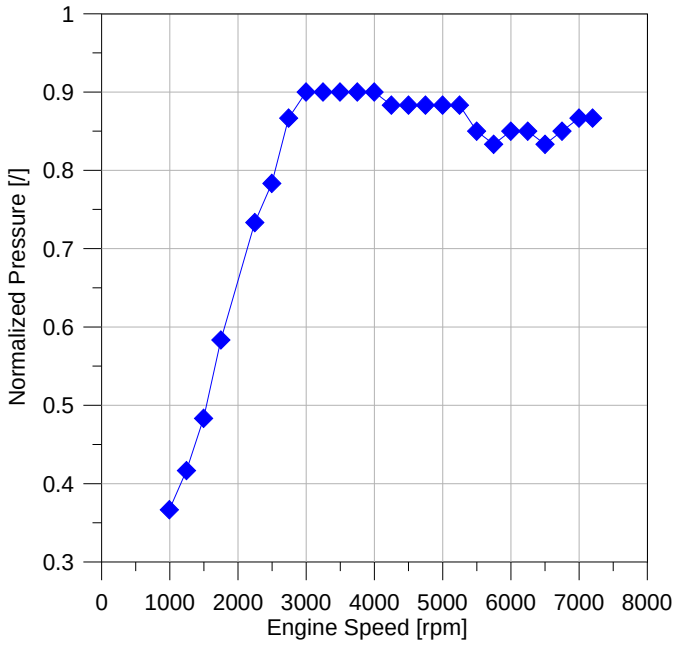

FIGURE 2.33: EXPERIMENTAL DATA, PRESSURE TREND AT T_{H20}=80°C

In the first area (no regulation), the pressure increases about linearly with the engine speed; between 2500rpm and 4000rpm the pressure remains constant (in this area the control ring is moving, as show in the figure 2.32); after 4000rpm the pressure decreases with the increase of the speed of rotation. The study of this phenomenon is one of the aims of the research.

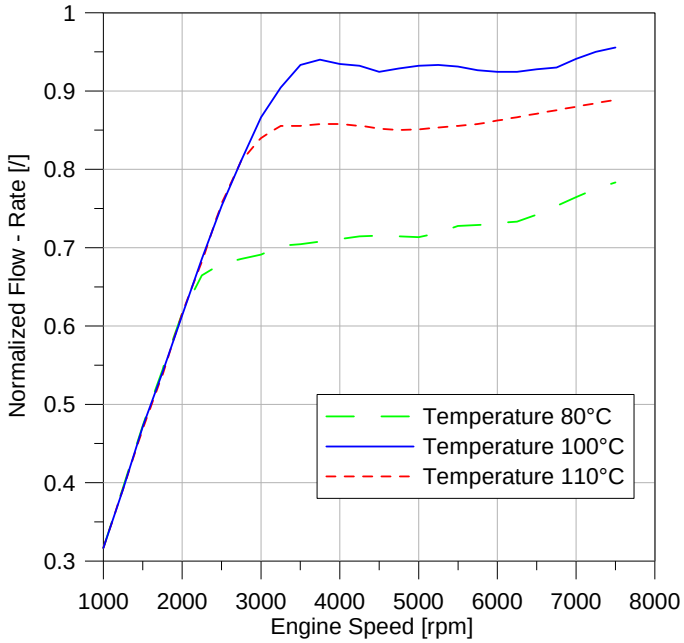

FIGURE 2.34: EXPERIMENTAL DATA, FLOW - RATE TREND

In the figure 2.34 the flow - rate as a function of the engine speed is shown; these

tests, have been obtained varying the oil temperature of the lubrication circuit. The engine speed varies between 1000rpm and 8000rpm.

Analyzing the figure 2.34 is possible to note the displacement variations for the three different curves. The flow - rate linearly increases up to 3000rpm then remains almost constant with the engine speed.

2.2.5 Three - Dimensional CFD Model Validation

The model validation has been carried out comparing results of the simulations with experimental data at the different rotational speeds and oil temperatures. Plots in figure 2.35 show the flow - rate comparison between numerical model results (red points) and experiments (continuous line).

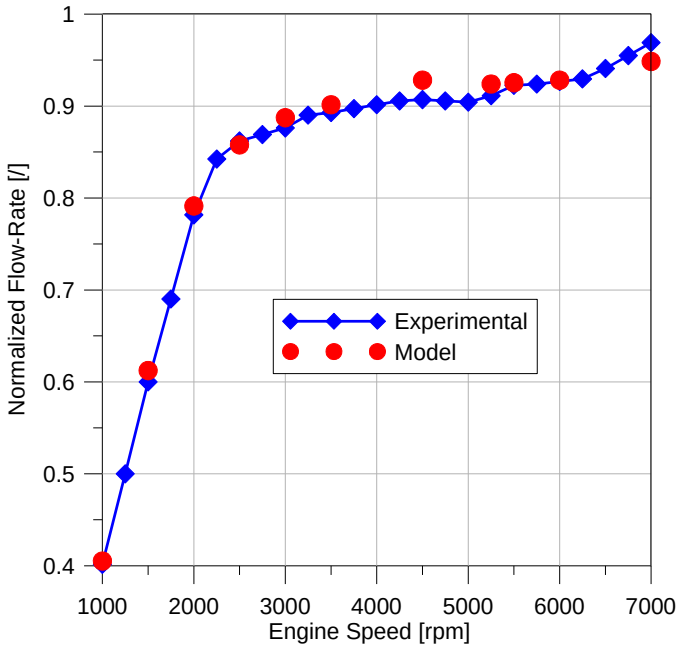

FIGURE 2.35: MODEL/EXPERIMENT RESULTS COMPARISON

From the analysis of the above plots (figure 2.35), it can be noted that the numerical model curves slope, with respect to the pressure axis, is very similar to the experimental results. This confirms that the model correctly simulates the pump and evaluate the displacement variations well.

Furthermore, for all the operating conditions simulated, i.e. 1000, 1500, 2000, 3000, 4000, 4500, 5000, 6000rpm and 7000rpm the maximum difference between the numerical model flow - rate estimate and the experimental data is 2%.

2.2.6 Model Results: Force Analysis

The following figures show the simulated results for the total internal force of F_o, $F_{c(vane)}$ and $F_{c(oil)}$ under the same conditions. Because these forces act in the upward direction in figure 2.36, it has the effect of inhibiting the eccentric movement of the control ring.

The following figures show graphs created in the same way for F_o, $F_{c(vane)}$ and $F_{c(oil)}$, the three components of the total internal force. These simulated results indicate that the $F_{c(oil)}$ centrifugal force component increases as the engine speed rises, thereby influencing the tendency for the total internal force to become larger.

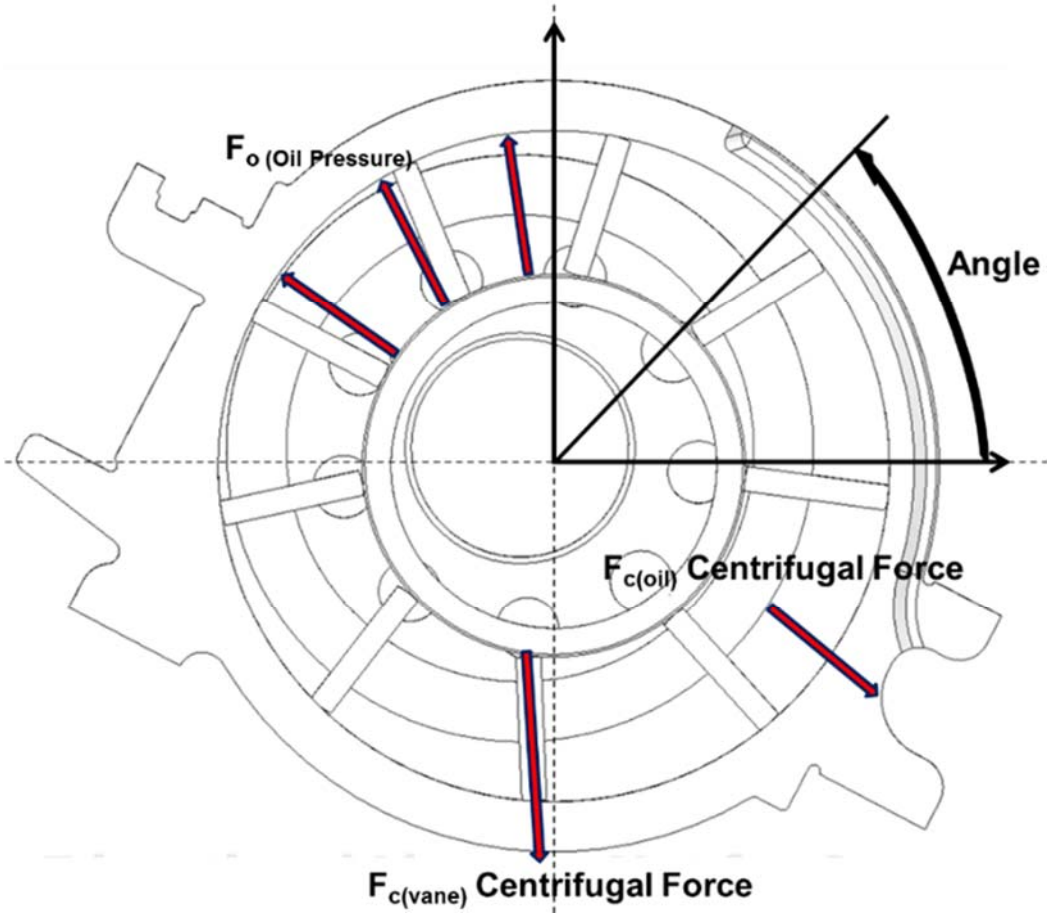

FIGURE 2.36: OIL PUMP FORCE ACTING ON THE SLIDE

Analyzing the graph in figure 2.37, for one revolution the pressure in each chamber, increases in the first 180 degrees (high-pressure side) then in the following 180 degrees (low-pressure side). From this graph, it can be noted the transition zone where the chamber passes from the delivery to the suction and vice versa.

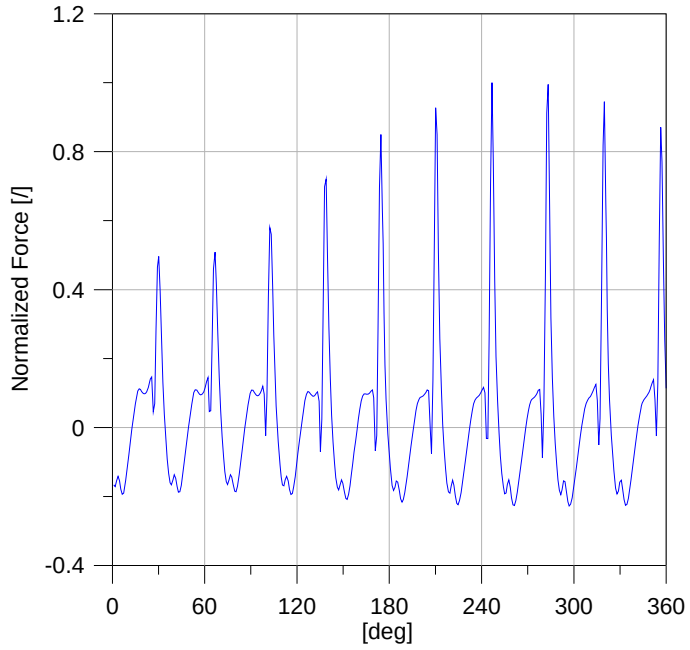

FIGURE 2.37: FORCE ACTING ON THE CAM RING AT 7000RPM

In the firsts 180 degree the maximum value of each oscillation is always less than the others 180 degree because the first area is the suction while the second one is the pump delivery.

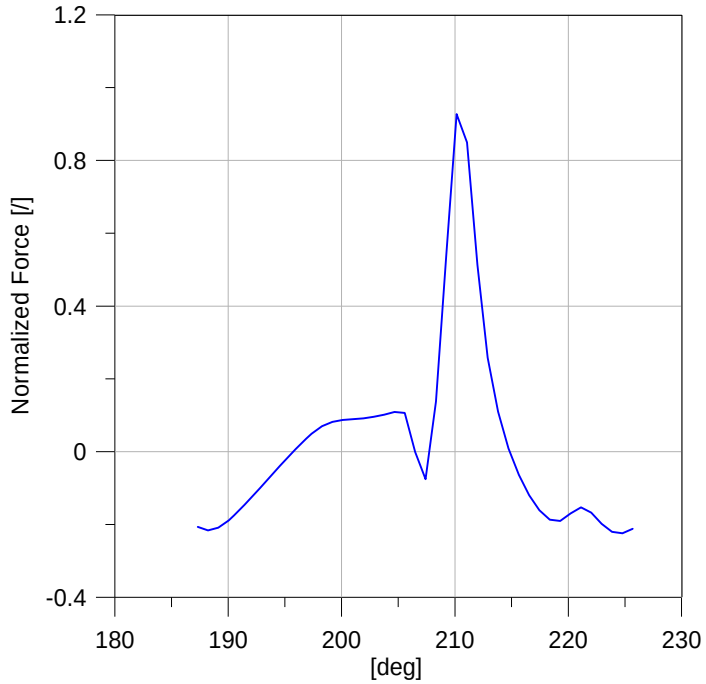

FIGURE 2.38: ONE OSCILLATION OF THE FORCE ACTING ON THE CAM RING AT 7000RPM

In figure 2.38, a zoom of one oscillation is shown. The pressure force grows during the pump shaft revolution, reaches a maximum and then decreases.

Figure 2.39 shows the pressure forces for one pump shaft rotation at 7000rpm.

Pressure forces (y and z components) are compared with the total force acting on the slide that is function of the pressure forces.

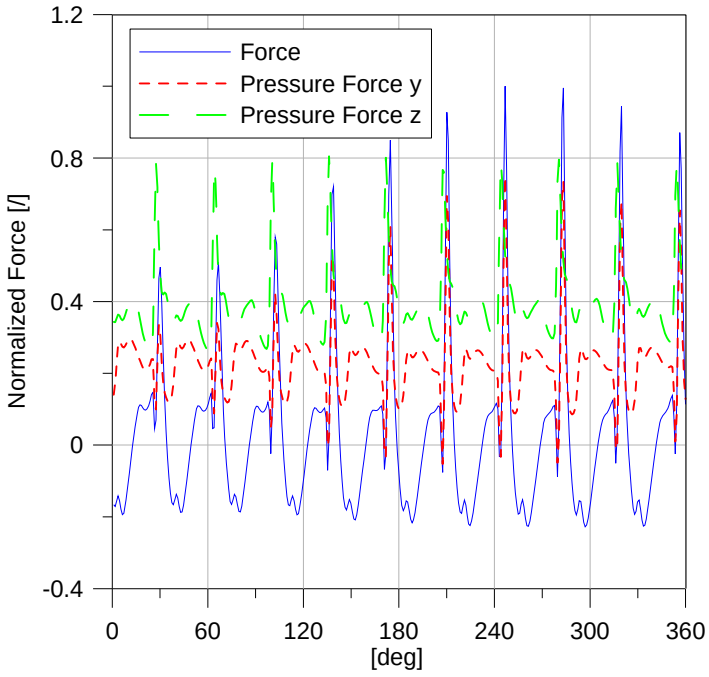

FIGURE 2.39: VARIATION OF THE FORCE WITH CHAMBER POSITION AT 7000RPM

Figure 2.40 shows a zoomed area between 185deg and 225 degree where one oscillation of these forces is plotted.

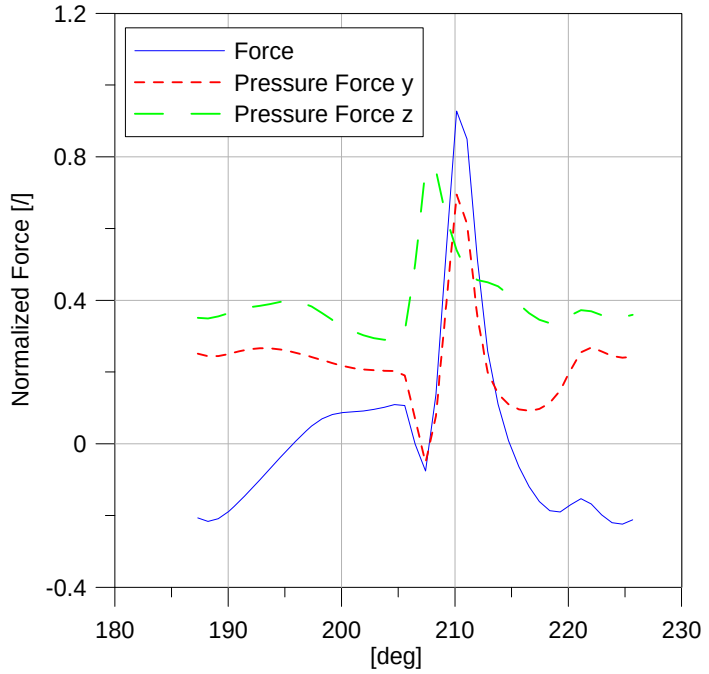

FIGURE 2.40: VARIATION OF THE FORCE WITH CHAMBER POSITION AT 7000RPM

In figures 2.41, a comparison of the forces acting on the slide for different oil pump shaft rotations is shown. While Another in figure 2.42 the vertical pressure forces at different engine speed are compared.

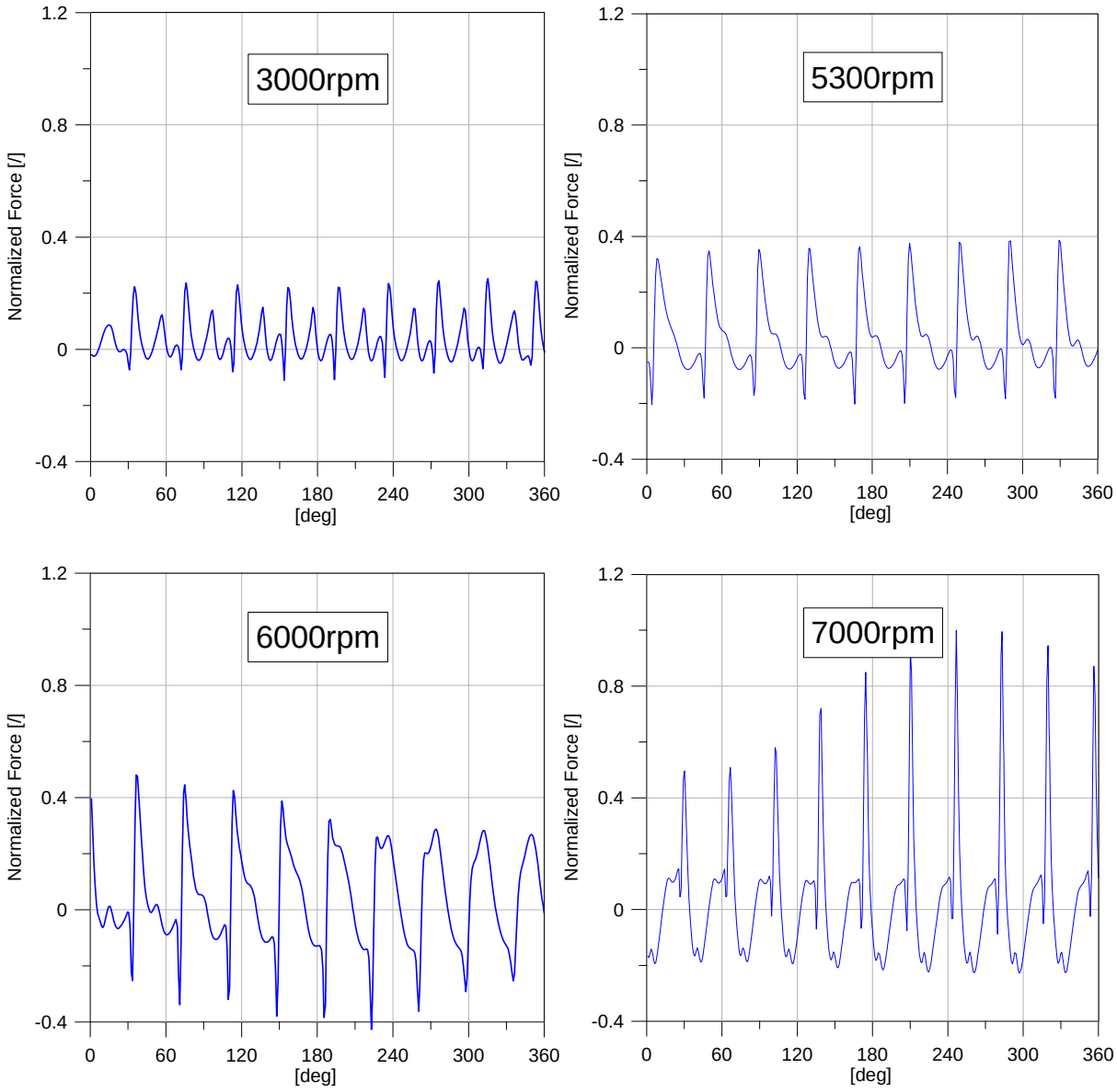

FIGURE 2.41: VARIATION OF THE FORCE WITH CHAMBER POSITION

From graphs in figure 2.41 and 2.42, it has been confirmed that problematic operating conditions are at the higher speed rotations especially between 6000rpm and 7000rpm when the forces acting on the chamber are higher than the other speed rotations.

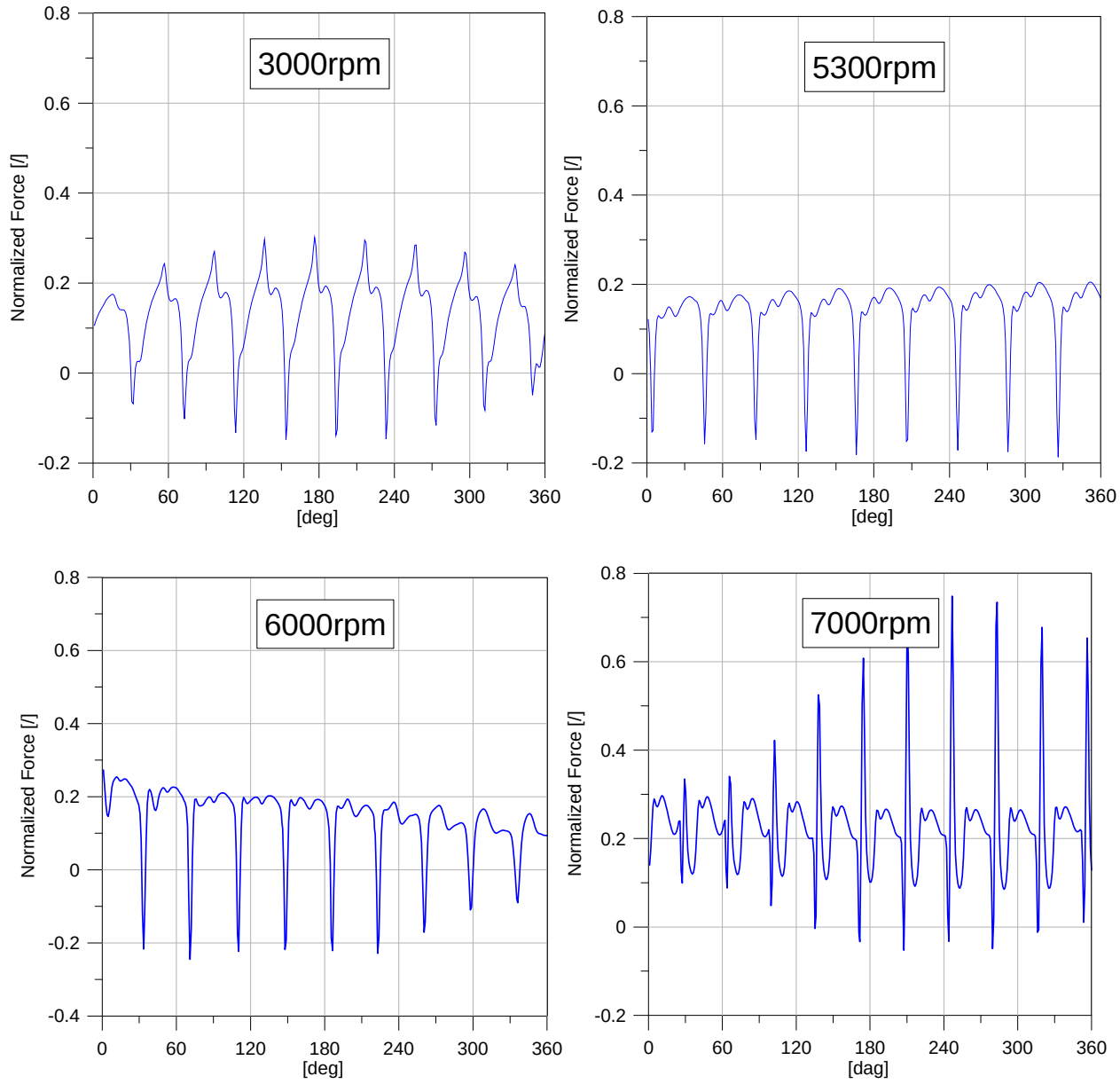

FIGURE 2.42: VARIATION OF VERTICAL FORCE WITH CHAMBER POSITION

Implementing in the model the cavitation prediction, is has been demonstrated that fault depend by the excessive reduction of the pressure in the high-low pressure connection zone. This study is shown by following.

2.2.7 Cavitation

By following results obtained implementing the real fluid model based on the work of Singhal [5], [7 - 10] are shown. In this way, the model can evaluate the cavitation effects when pressure, in a specified zones of the fluid domain, falls below

the saturation pressure. Vapor bubbles form and then collapse as the pressure rise again [3 - 4].

Many physical models for the formation and transport of vapor bubbles in the liquid are available in literature, but only few computational codes offer robust cavitation models. This is due to the difficulty to handle gas/liquid mixtures with very different densities. Even small pressure variations may cause numerical instability if they are not optimally treated [5].

Using the cavitation model the oil pump model is able to find the areas in which this phenomena happens as shown in following figures.

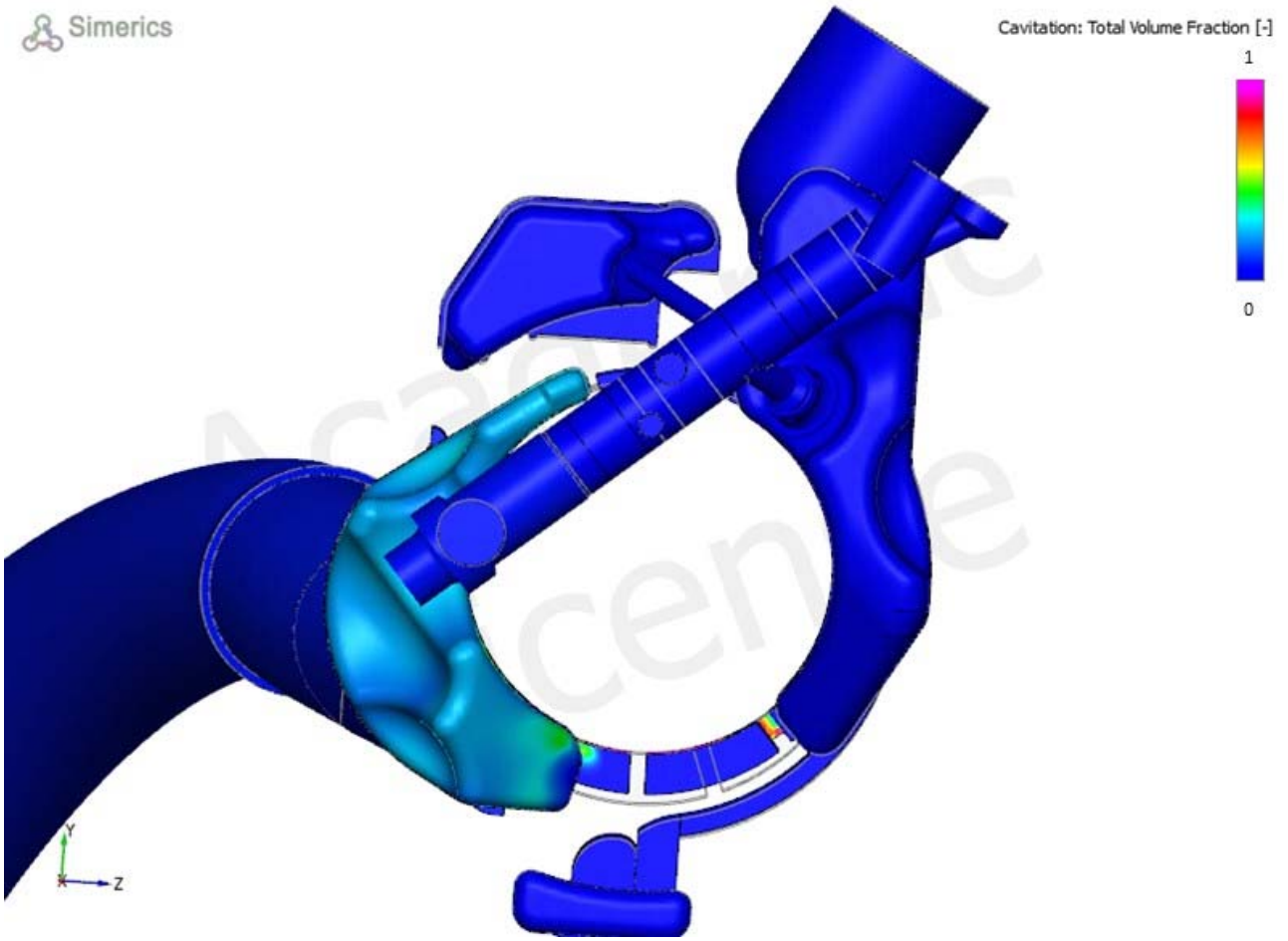

FIGURE 2.43: CAVITATION/AERATION PATTERN OF THE OIL PUMP AT 7000RPM

Figure 2.43 is a snapshot of a transient simulation showing the instantaneous gas volume fraction at 7000rpm. The magenta color represents 100% gas volume fraction and the blue color represents pure liquid.

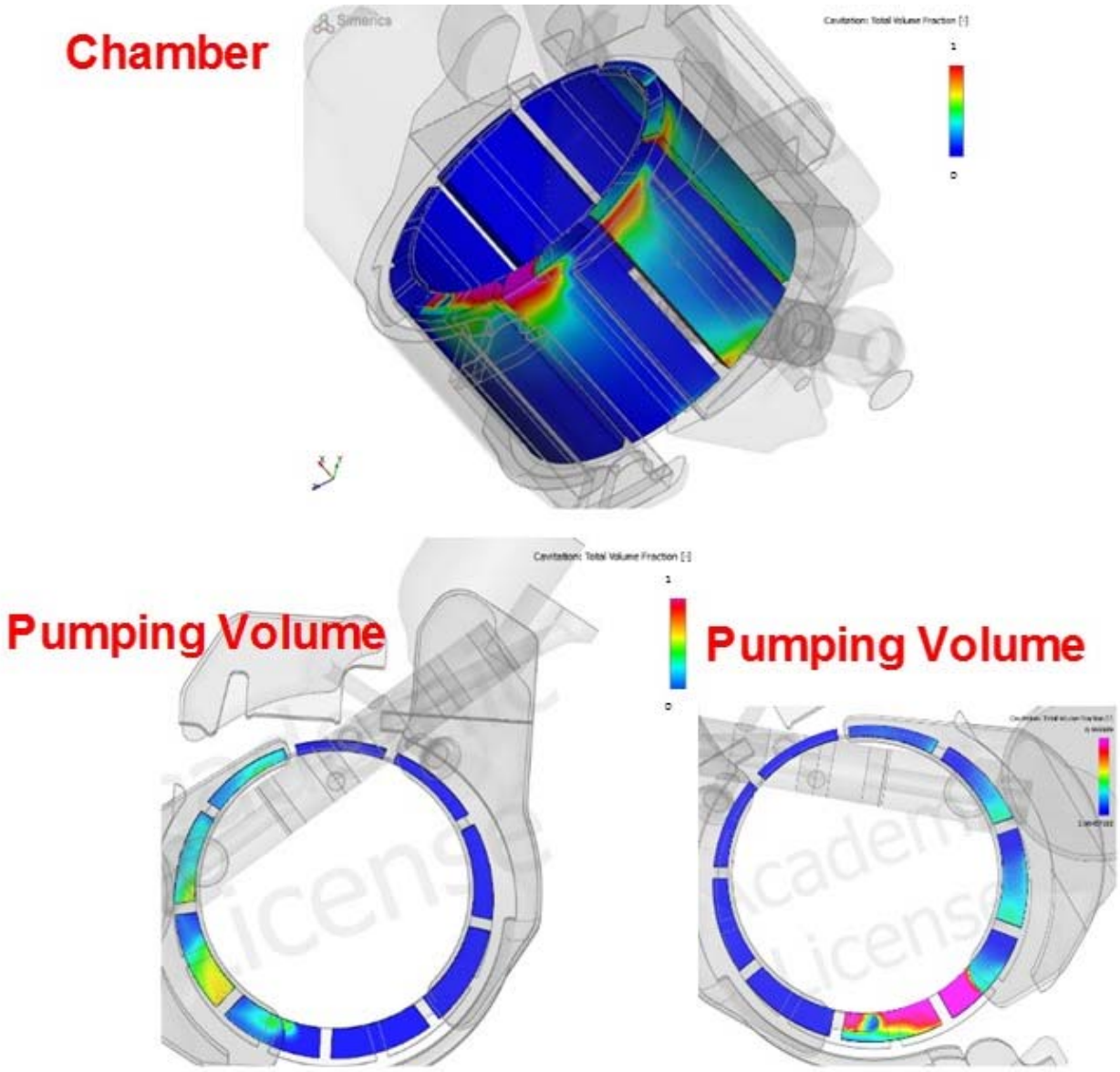

FIGURE 2.44: CAVITATION AREAS AT 7000RPM

In figure 2.44 the vapor volume fraction in the pumping volume is shown, as for the figure 2.43, the magenta color indicates that the region has more than 50% vapor fraction and the blue color indicates that vapor is close to 0% fraction. The cavitation bubbles are located in the suction side of the vanes. In the image in the right corner of the figure 2.44 the vapor volume fraction is near the 100% in some areas of the pumping volume.

In the following figures, the vapor volume fractions for three different pump shaft speed are compared. This analysis confirms that cavitation phenomena happen especially at high speed rotations.

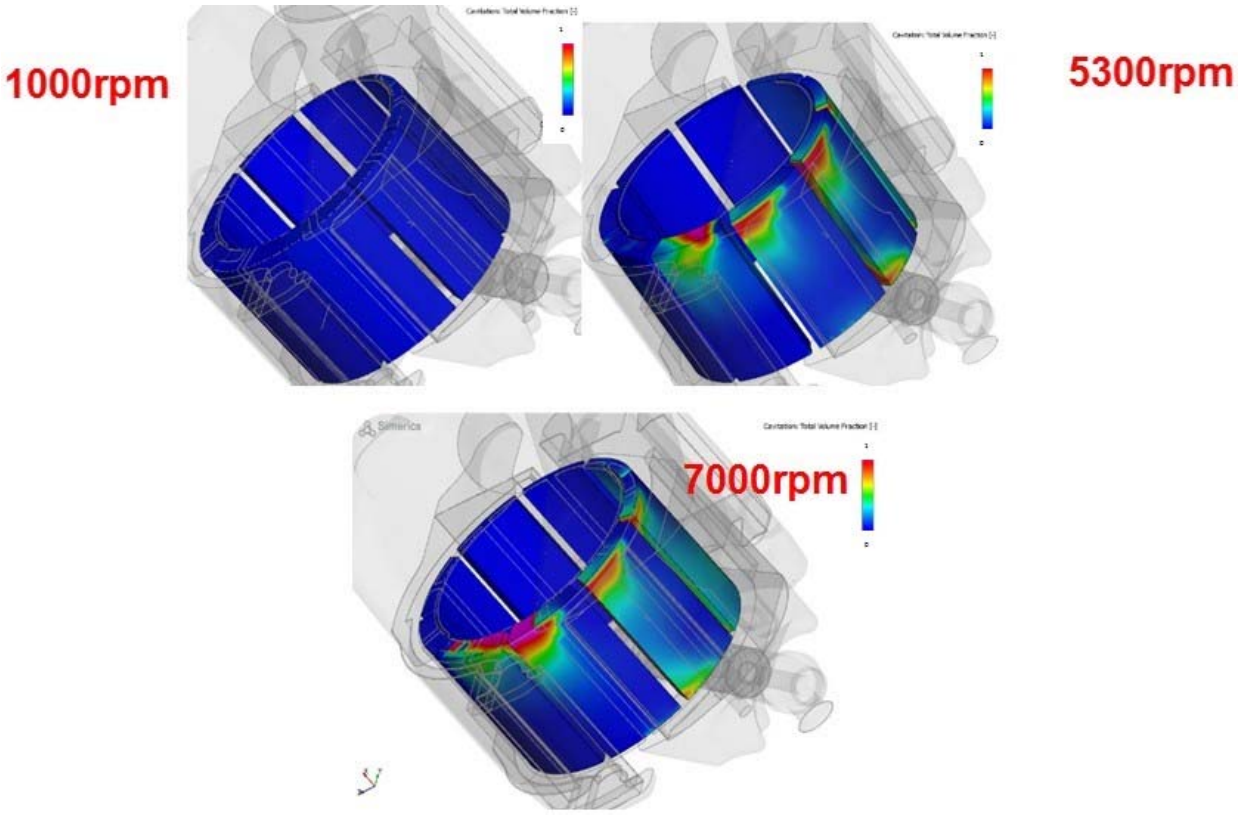

FIGURE 2.45: CAVITATION AREAS COMPARISON AT DIFFERENT OIL PUMP SHAFT SPEED

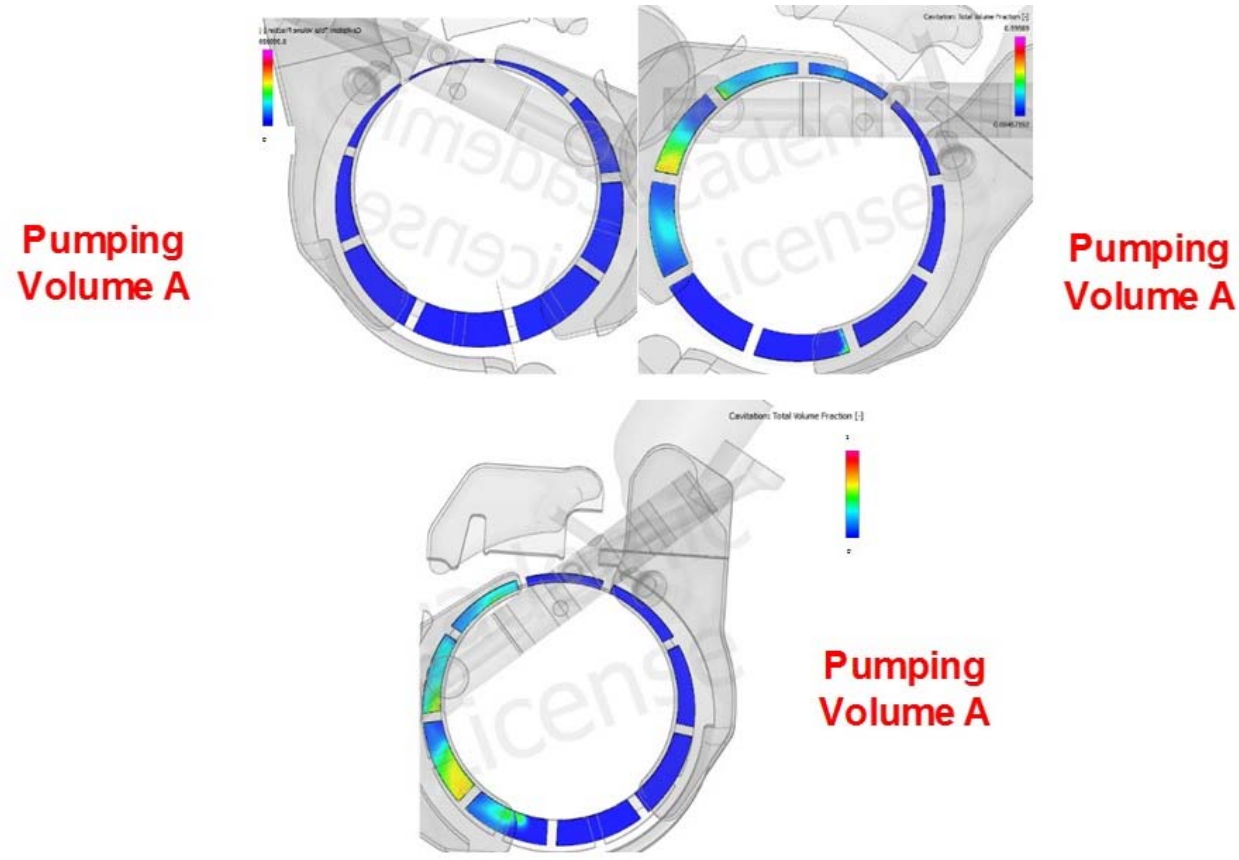

FIGURE 2.46: CAVITATION AREAS COMPARISON AT DIFFERENT OIL PUMP SHAFT SPEED

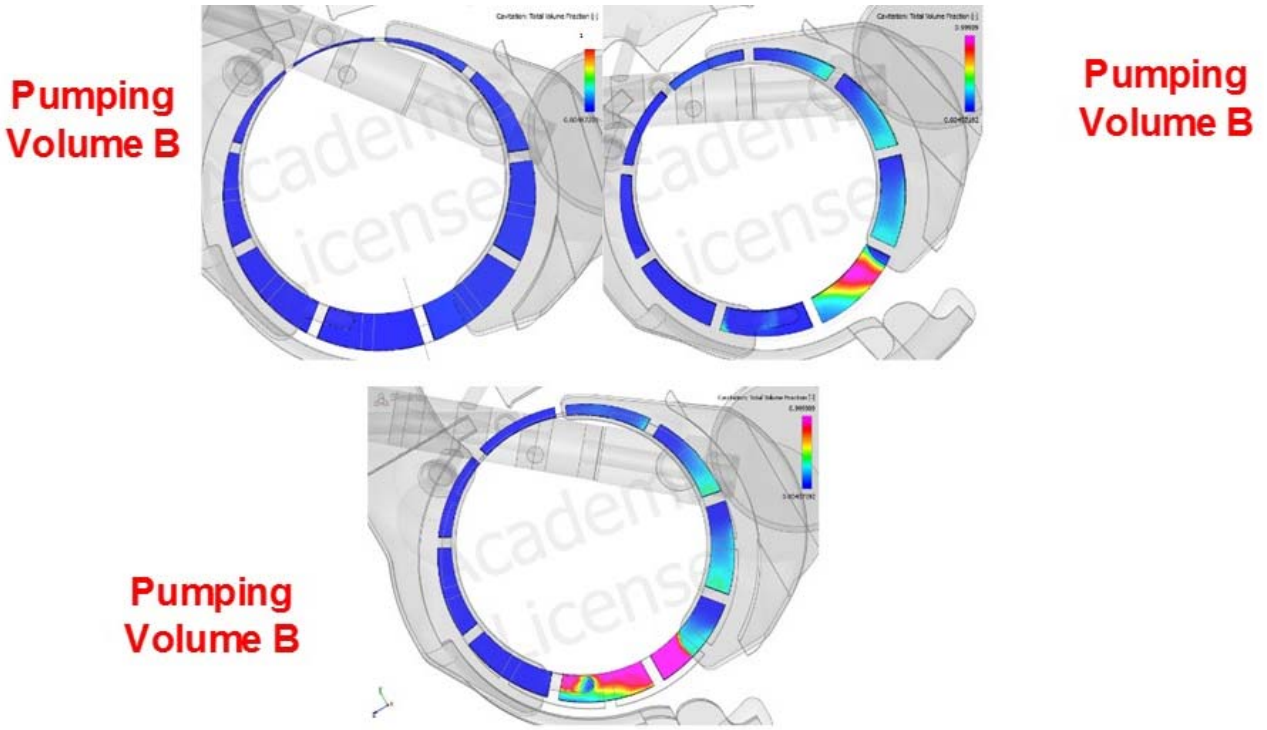

FIGURE 2.47: CAVITATION AREAS COMPARISON AT DIFFERENT OIL PUMP SHAFT SPEED

Figures 2.45 – 2.47 show the cavitation phenomena happening in the suction area, more frequently at the high speed rotations.

The cavitation phenomena is more frequent increasing the speed rotations. Analyzing the figure 2.45 is possible to understand what happen inside the pump fluid volume between 1000rpm to 7000rpm. The suction area at 1000 rpm is blue meaning that there is no cavitation in the fluid volume, when the speed rotations increase some areas become red and magenta (cavitation areas).

2.2.8 Conclusions

In this paragraph an analysis of an oil pump of an high performance engine has been presented. First of all, the detailed 3D CFD model of the oil pump has been described. The model, starting from the pump geometry, allows to evaluate the pump performance taking into account all phenomena that occurs during the pump operation, including cavitation.

The model has been validated with experimental data, performed on an engine test bench by the engine manufacturer. In all examined engine conditions, model results

fit very well the experimental data, showing a very low percentage error. Consequently, this technique proves to be well predictive for also these type of issues.

A detailed analysis of the force acting on the internal pump components have been performed in different oil pressure conditions and shaft speed. First of all, it was noted that at high engine speed the forces on chamber reaches high values and this aspect has been investigated taking into account also of the cavitation phenomena. Moreover, an analysis of the cavitation phenomena has been done. It was noted that the higher risk zones are located in the area where the chamber starts to be connected with the suction, most problematic operating conditions are at the high speed rotations.

Finally, the methodology and the results can represent a valid tool. The tridimensional CFD modeling can be implemented for the design of new engines systems or pump, as it is computationally very efficient.

2.3 Gerotor Pump

2.3.1 Introduction

The modeling approach can be used for other applications. In this paragraph the research done on a gerotor pump of the lubrication circuit of an engine is shown. As already said for the case analyzed in the paragraph 2.2 (Variable Displacement Vane Pump), targets of nowadays engine designers are the reduction of exhaust emissions and fuel consumption and the improvement of engine performance. In the design phase of a new internal combustion engine, therefore, all the aspects related to friction and mechanical power loss must be deeply considered. All engine components have to be studied and designed from the early stages of their development to reduce frictions with them also the lubrication system and the oil pump.

The scope of this research is the study of an pump in order to identify main losses that affect on the volumetric efficiency of the pump. An accurate analysis of the losses due to the leakage between inner and outer of a "Gerotor Pump" through a modeling approach it will be presented by following. In recent years, during the design phase, one-dimensional and three-dimensional codes have been used to simulate the behavior of the engine oil circuit components. Using these codes, information may be obtained on points that are not always experimentally measurable. 1D codes are simpler to use for modeling complex systems and require less computational power. On the other hand, they can hardly be predictive as 3D codes. For these reason a three-dimensional CFD model of the oil delivery pump made with a three-dimensional CFD has been built up. An experimental comparing has been performed at the Department of Industrial Engineering of University of Naples "Federico II". Experimental data have been used to validate the CFD code.

2.3.2 Engine and Pump Description

Before describing the CFD model constriction, engine characteristics will be shown to better understand the pump working. The engine is a high performance motorbike engine manufactured (see figure 2.48), four cylinders with a displacement

of 999,6 cm^3, and a maximum rotation speed of 14000 rpm. The lubrication circuit is a wet sump type and is fed by a gerotor volumetric pump, with a displacement of 8 cm^3/rev.

FIGURE 2.48: MOTORBIKE ENGINE

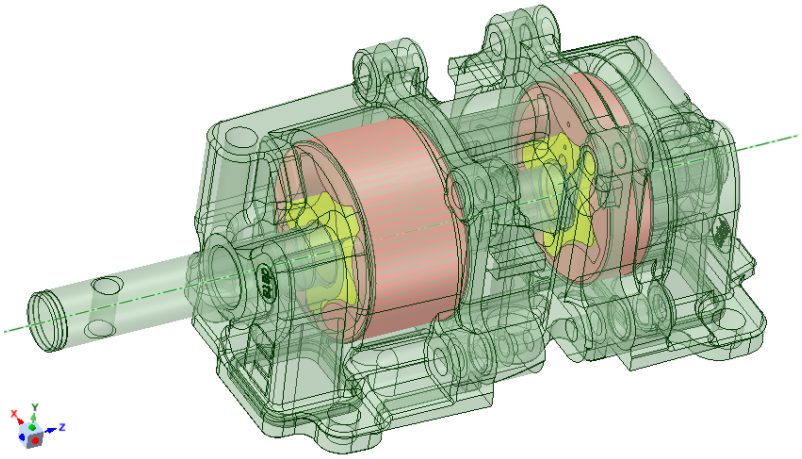

FIGURE 2.49: PUMP ROTORS

The lubrication pump consists of two gears (figure 2.49), with the inner rotor rotating off-center, creating 5 vanes with volumes evolving in one revolution from a minimum to a maximum value during the suction phase and vice versa during the discharge phase.

The rotors have 4 and 5 teethes respectively, the outer rotor rotates with an angular velocity that is equal to 4/5 of the inner rotor velocity (the transmission ratio between the rotors is 4/5).

The whole pump consists in fact of two (twin) pumping units as it is used also for the oil cooling circuit (as showed in figure 2.49).

The whole pump model (for the lubrication and oil cooling circuit) and the validation of the lubrication pump model will be presented in this paragraph.

2.3.3 Three - Dimensional CFD Model

The pump has been simulated with the three-dimensional CFD approach described in the thesis.

From the pump 3D geometry, the fluid volume has been extracted, starting from the surfaces wet by the lubricant itself. The obtained geometry has then been meshed with the program grid generator [3].

Figure 2.50 shows the pump mesh in a section plane of the considered pump. In the boundary layer the grid density has been increased. Figure 2.50 clearly shows the different grid of the moving parts (pumping volume) and the stationary parts (ports). Each volume connects to the others via an implicit interface in figure 2.51.

The model of the considered pump consists of a 400.000 3D cells.

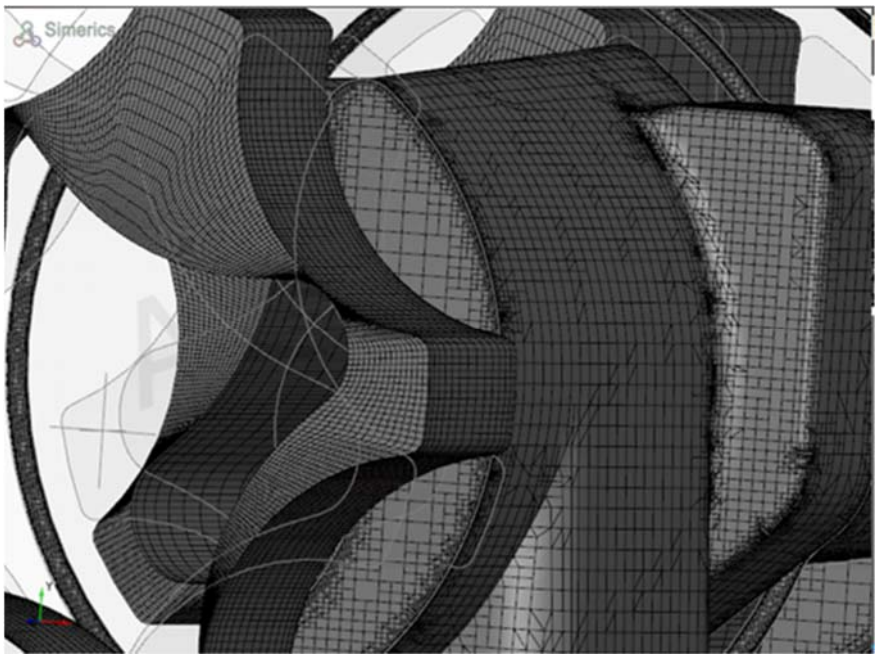

FIGURE 2.50: BINARY TREE MESH – PUMP CROSS SECTION

Figure 2.51 shows the interaction between the rotor and the posts colored in pink. The interface is updated at each time-step.

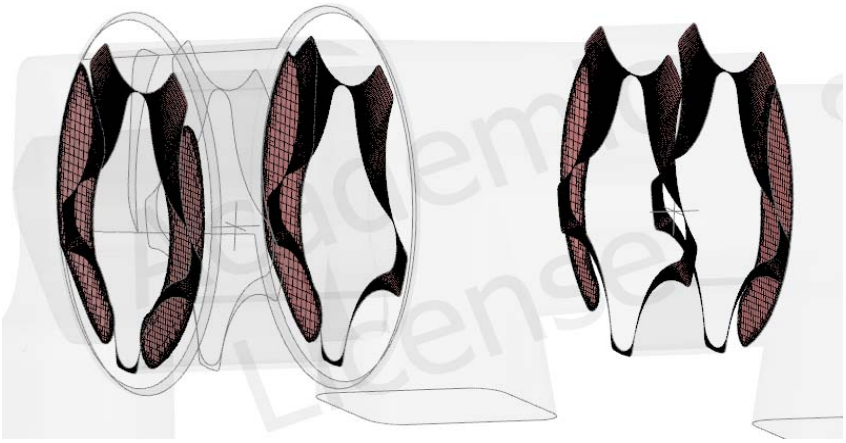

FIGURE 2.51: MISMATCHED GRID INTERFACE BETWEEN MOVING AND STATIONARY VOLUMES

Boundary conditions are experimental data obtained with a test bench campaign held at the Department of Industrial Engineering of University of Naples. The suction port pressure and lubricant density as a function of rotational speed were provided as input for the numerical model, between 1000 rpm and 4000 rpm and with an oil temperature of 80 °C and 110 °C.

Once created the model simulations have been run to obtain the pump characteristics map, which is delivery flow - rate as a function of pressure. Figure 2.52 show the pressure distribution in the pumping volume and the ports.

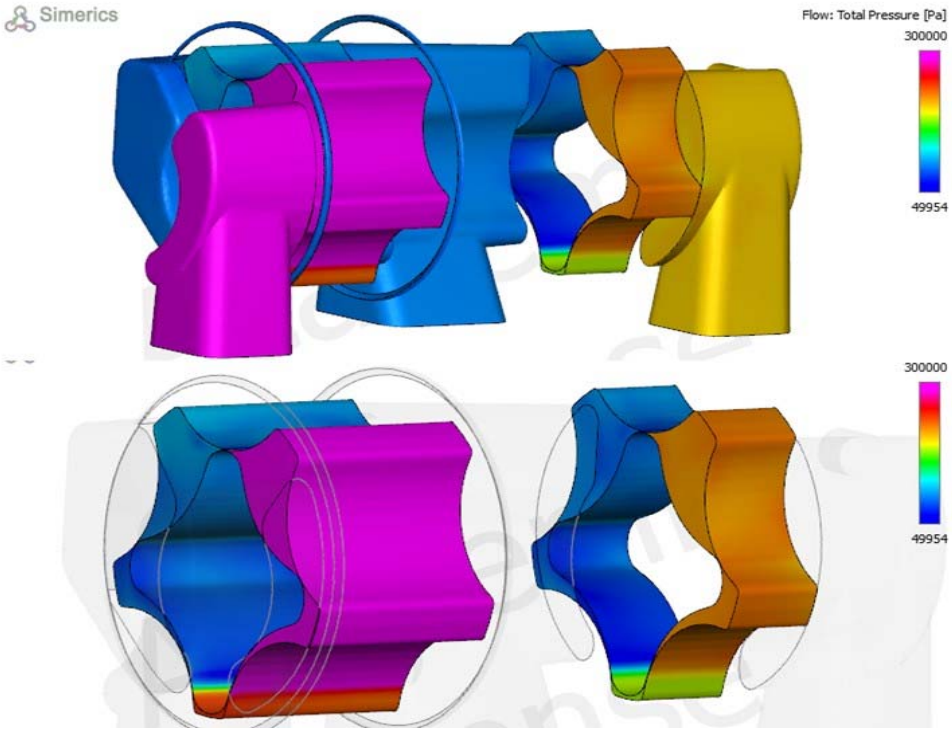

FIGURE 2.52: PRESSURE DISTRIBUTION IN THE FLUID VOLUME AND IN THE PUMPING VOLUME (BETWEEN ROTORS)

2.3.4 Three - Dimensional CFD Model Validation and Results

As already mentioned, the pump model validation has been performed using data from an experimental campaign held at the Department of Industrial Engineering of University of Naples "Federico II". The bench hydraulics scheme is represented in figure 2.53, which will be used to describe the bench functionality.

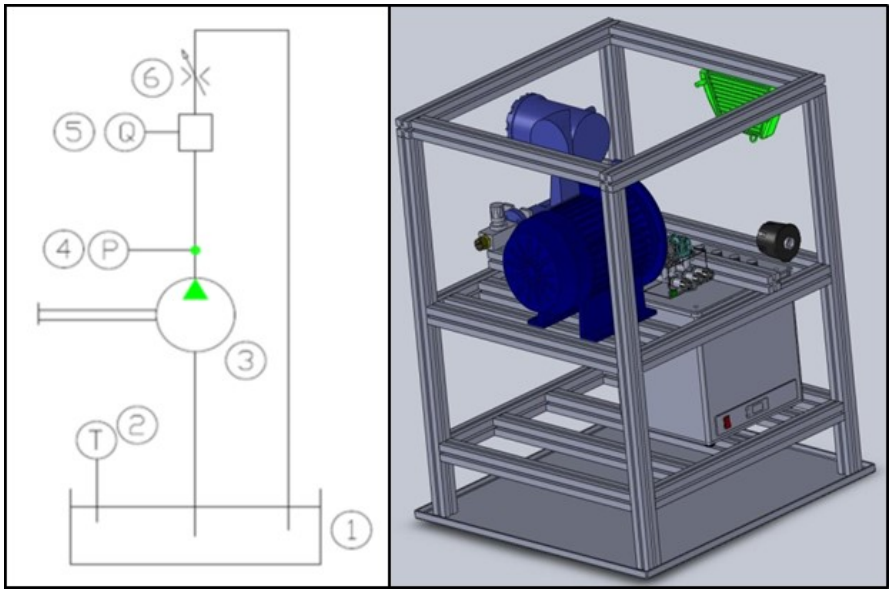

FIGURE 2.53: PUMP TEST BENCH

The oil pump (3) draws oil from a thermostatic tank (1) and delivers it to a mass flow - rate transducer (5) and a lamination valve (6). In the test bench circuit, a thermocouple (2) and a pressure transducer (6) are also integrated in the bench. The pump is motored by an electric motor, which, through an inverter, can vary the pump shaft speed; acting on the lamination valve, the oil pressure in the delivery line can be changed. The pump speed is acquired thanks to a 360-teeth encoder.

An acquisition system allows to control and manage the test bench output signals via a multi-function National Instruments® card (type NI PCI MIO 16 E 1) and a software tool for the management and acquisition of data based on LabView 2011 and developed at the Department of Industrial Engineering of University of Naples "Federico II".

The oil is a 5W40 that complies with API SL, JASO MA-2, and ACEA A3 specifications.

The tests allowed determining the full pump characteristics map, in terms of pressure/flow - rate curves (figure 2.54) as a function of rotation speed and oil temperatures of 100°C.

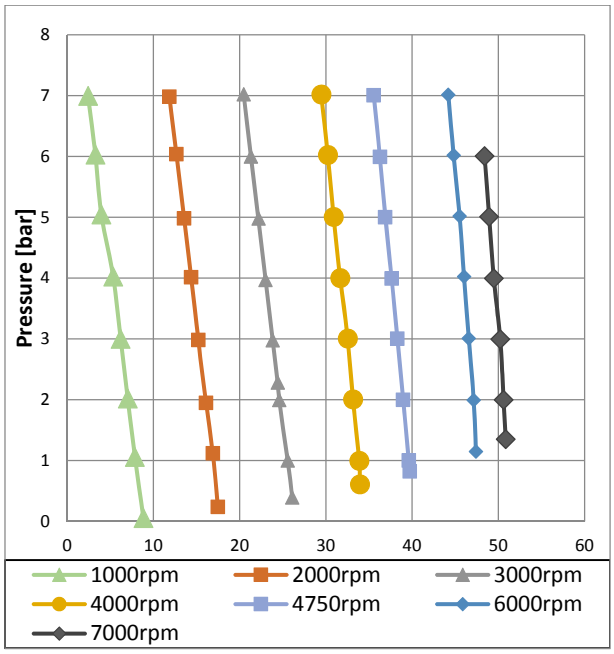

FIGURE 2.54: P-Q CURVES AT 100°C OIL TEMPERATURE

Figure 2.55 shows the flow - rate trend in function of engine speed between 1000 – 7000 rpm and oil pressure of 1bar, 5bar and 7bar. The experimental curves here been compared with the theoretical curve.

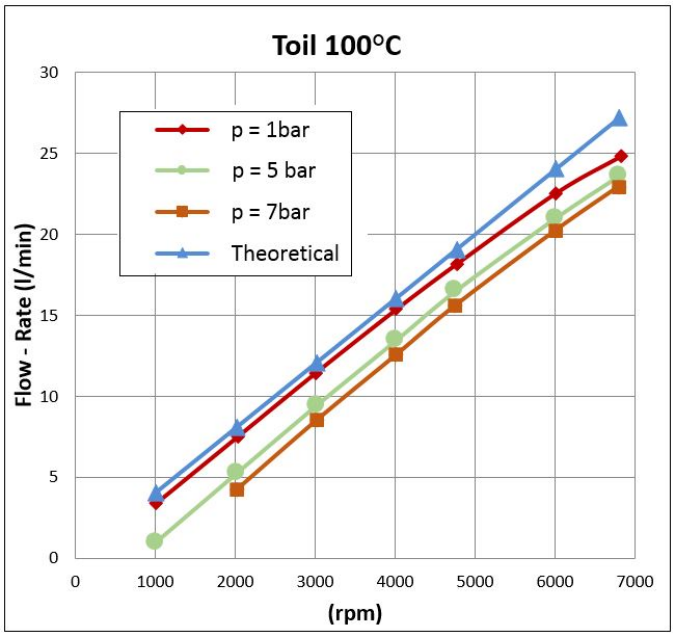

FIGURE 2.55: (FLOW-RATE/RPM) CURVES

From the analysis of the above graph it can be noted that the slope of the experimental curves is very similar to the theoretical curve especially at low rotation speed.

The theoretical curve has been obtained from the expression:

$$Q_{teo} = V_g \cdot \frac{n}{1000} \tag{2.16}$$

Where V_g is the displacement [cm^3], n is the pump rotation speed [rpm] and Q is the pump flow - rate [l/min].

The pump efficiency has been calculated with the equation:

$$\eta = \frac{Q_{eff}}{Q_{teo}} \tag{2.17}$$

Where Q_{eff} is determined from experimental data.

The graph in figure 2.56 shows the pump efficiency as function of rotation speed and oil pressure at the lubricant temperature of 100°C.

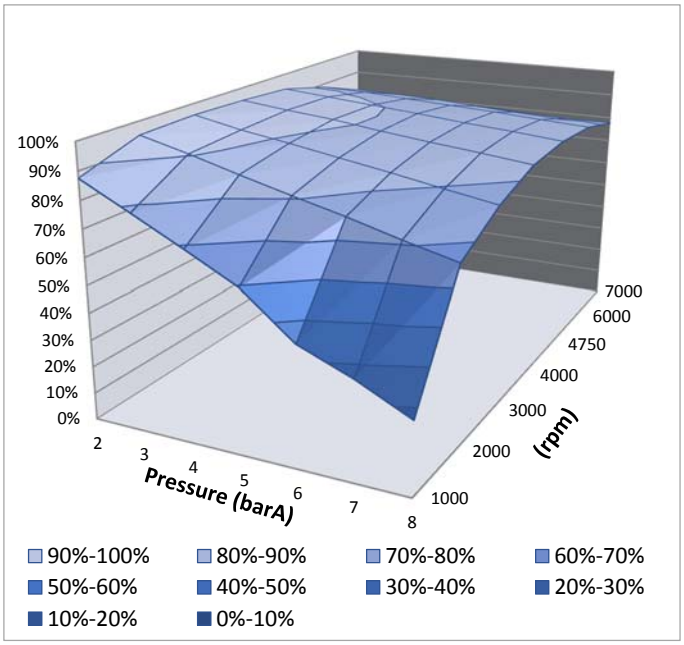

FIGURE 2.56: OIL PUMP EFFICIENCY 100°C OIL TEMPERATURE

The full pump characteristics map has subsequently been calculated in terms of pressure/flow - rate curves (figure 2.57) as a function of rotation speed and oil temperatures of 80°C and 100°C.

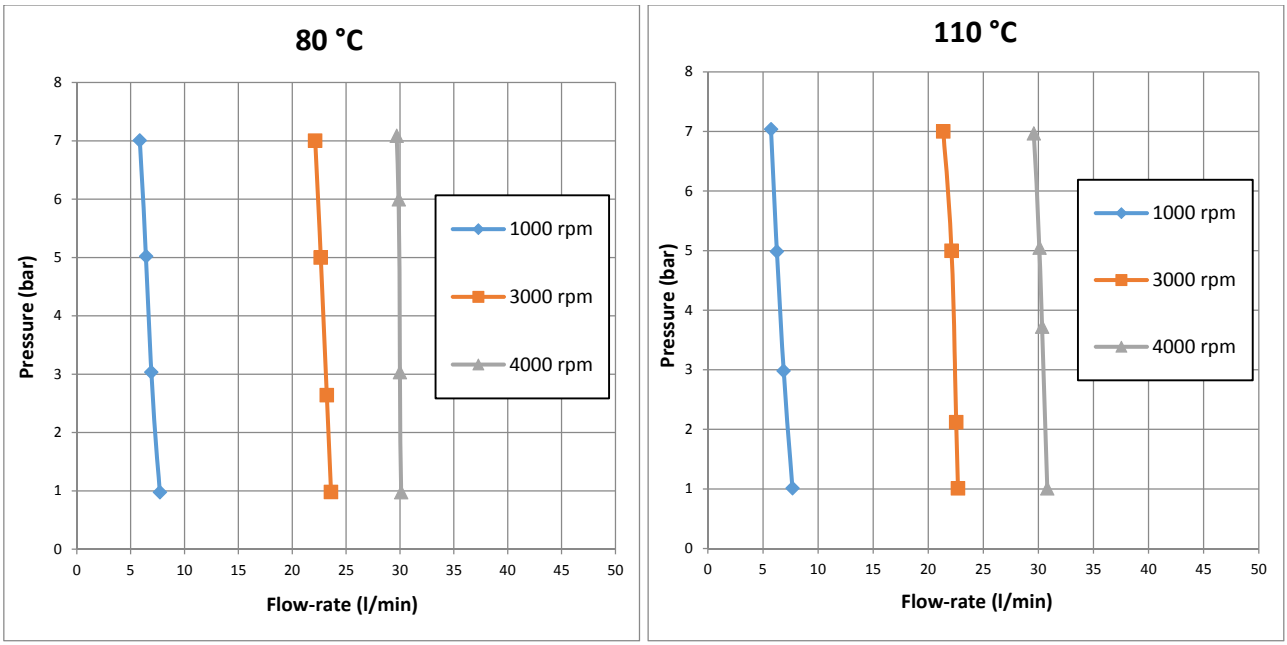

FIGURE 2.57: (P-Q) CURVES AT 80°C AND 110°C OIL TEMPERATURE

The model validation has been carried out comparing results from the 3D CFD model simulations with experimental data at the different rotation speeds and oil temperatures (80°C and 110°C). Plots in figures 2.58 and 2.59 show the comparison between numerical model results (dashed lines) and experiments (continuous line) for different speeds and oil temperatures.

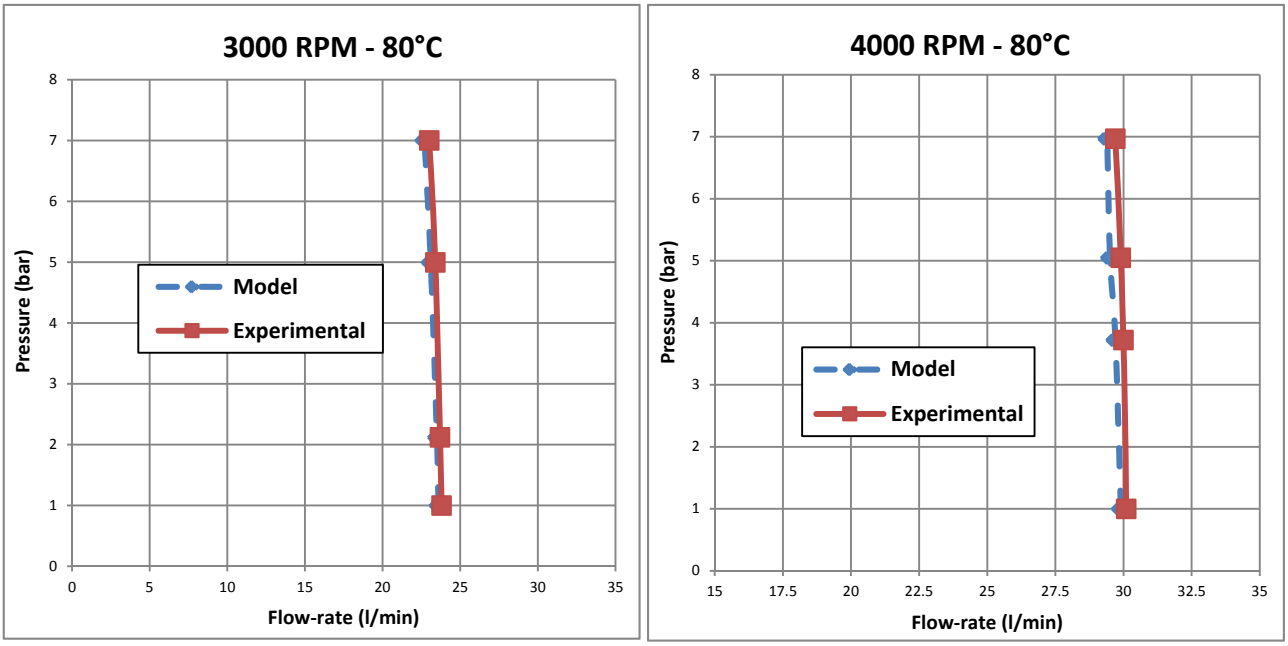

FIGURE 2.58: MODEL/EXPERIMENT RESULTS COMPARISON AT 80°C

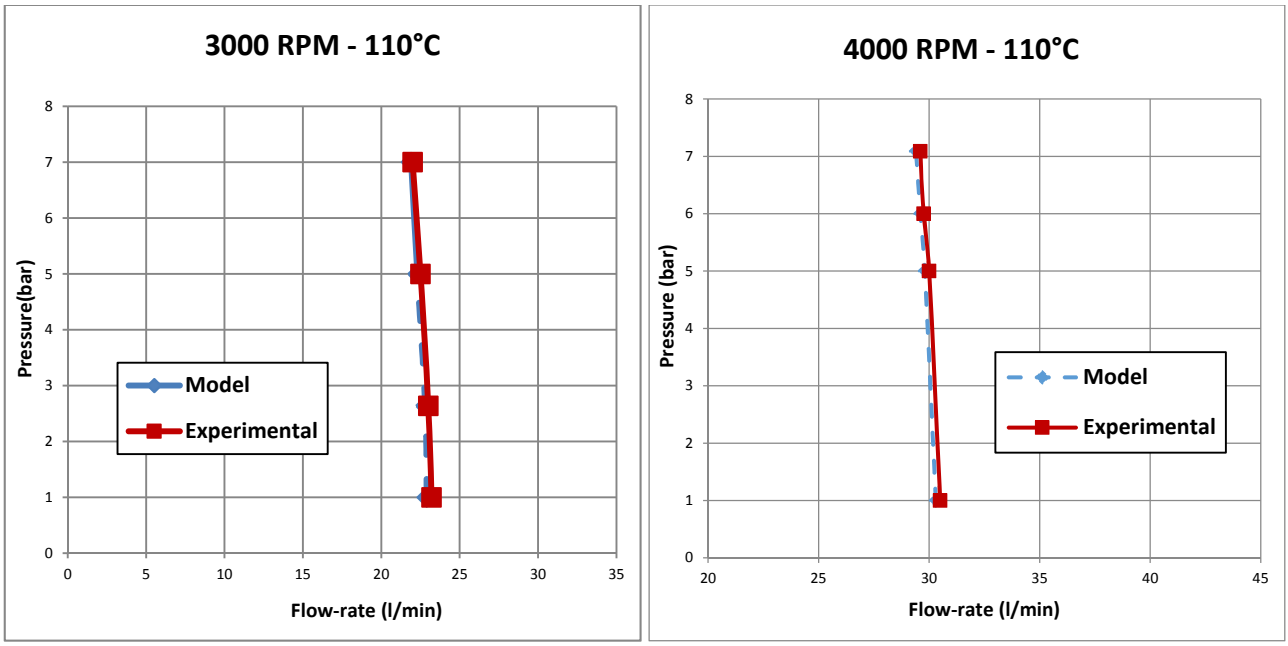

FIGURE 2.59: MODEL/EXPERIMENT RESULTS COMPARISON AT 110°C

From the analysis of the graphs in figures 2.58 and 2.59, it can be noted that the numerical model curves slope, with respect to the pressure axis, is very similar to the experimental results. This confirms that the software correctly simulates the pump and captures all main leakages, inter-gears losses and side losses between rotors and pump casing (figure 2.60).

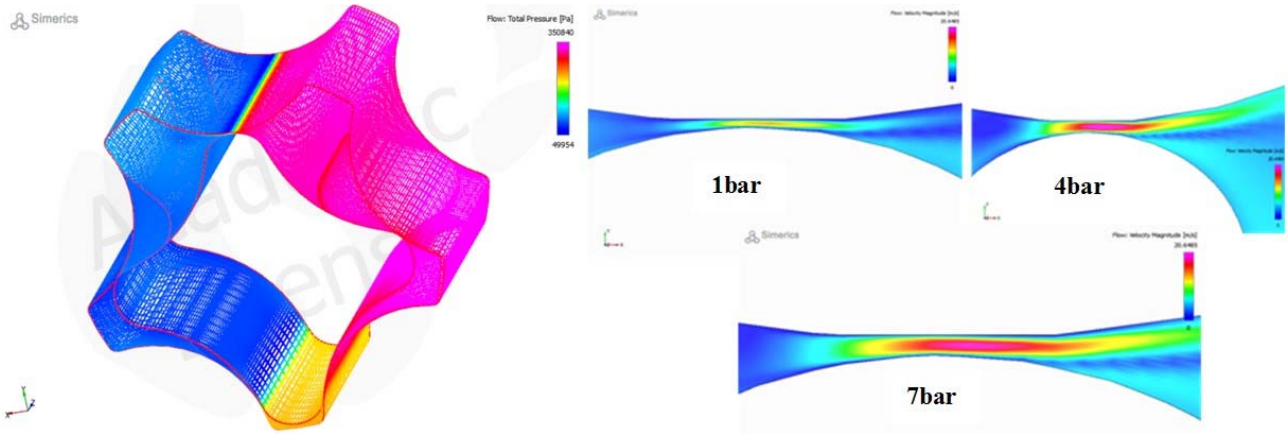

FIGURE 2.60: MEAN VELOCITY OF FLOW IN LEAKAGE AT 1000RPM

For all the analyzed running conditions, i.e. 1000, 1500, 2000, 2400, 2800 and 3000 rpm rotational speeds, the maximum difference between the model flow - rate data and the experimental one is 9%. This is true also for all the analyzed oil temperatures.

Furthermore, the model allow studying the oil flow - rate behavior versus pump shaft angle. Figure 2.61 shows the flow - rate ripple at two different oil pressures for a pump shaft revolution of 3000rpm.

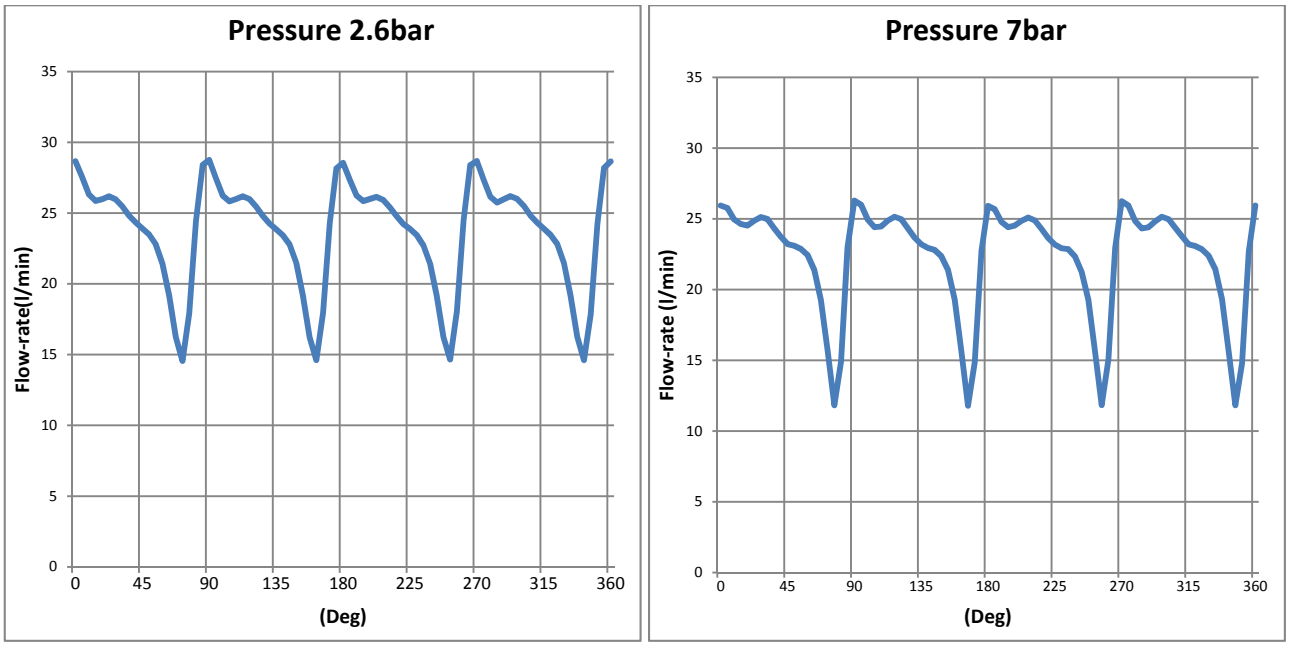

FIGURE 2.61: FLOW - RATE AT 3000RPM

2.3.5 Conclusions

The research presented in this paragraph shows another application of the a tridimensional CFD modeling methodology described in this PhD thesis. The pump, in fact, is a Gerotor one with two pumping volumes, one suction port and two delivery ports one for the lubrication circuit one for the cooling one. The study is focused on the simulation of the main leakages due to inter-gears losses and side losses between rotors and pump casing. The model has made up with a commercial tri-dimensional code, which allows, starting from the pump geometry, to evaluate the pump performance, taking into account all the phenomena that occurs during the pump operation, including cavitation. The pump model results have been compared with experimental data performed in a hydraulic pump test bench of the Department of Industrial Engineering of University of Naples "Federico II", showing a good correlation between experimental and simulated data. Model results confirm the accuracy of the methodology with a good prediction of the pump working. Therefore,

also for this application, it possible to affirm that taking into account of the model results (3D visualization) the component can be optimized redesigning critical areas to improve the volumetric efficiency of the pump.

2.4 Engine Lubrication Circuit

2.4.1 Introduction

Following the activity on a gerotor pump, the research described in this paragraph is focused on the study of a lubrication circuit of a diesel engine modeling the pump and all the circuit with a three-dimensional approach. The innovation of this research consist in the fact that the modeling technique described can be applied not only for the improvement of the only pump but of all users of the lubrication circuit without increasing a lot computational time. In this application the pump is a gerotor one; the oil flow rate is compressed and sent through the lubrication circuit to the different users downstream. The technique ability to predict, in an "economic" way, the unsteady hydraulic system such as the lubrication circuit.

First of all, an accurate model of a lubrication circuit oil pump will be described. The model has been validated with data from an experimental campaign carried out in the hydraulic laboratory of the Industrial Engineering Department of the University of Naples.

Secondly, the oil pump model has been coupled with a tri-dimensional model of the entire lubrication circuit, in order to compute all the hydraulic resistances of the network and the oil consumption rate of the circuit components

2.4.2 Engine and Pump Description

Before proceeding with the description of the simulation model, it is worth describing the engine architecture and pump characteristics. The considered diesel engine has a 2500 cm^3 displacement, four in-line cylinders and a maximum revolution speed of 2800 rpm.

Figure 2.62 shows the oil path inside the lubrication circuit; the oil pressured by the pump goes through a filter - exchanger and then feeds the engine block with all its users (crank - shaft bearings, piston cooling jets, cam - shaft bearings, etc.) and the engine head (inlet and outlet valves tappets).

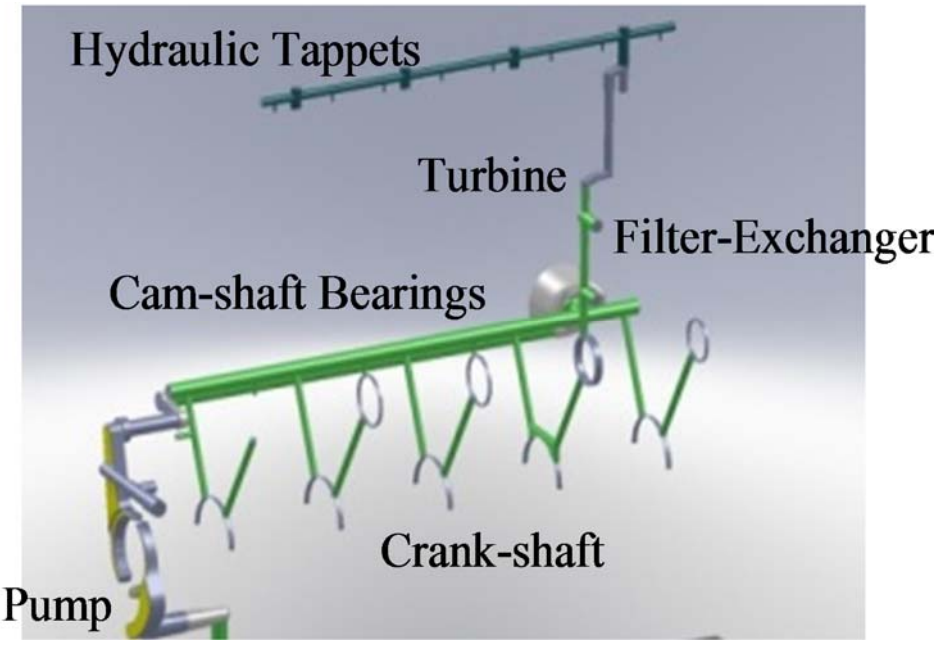

FIGURE 2.62: LUBRICATION CIRCUIT

The gerotor volumetric oil pump has a displacement of 13 cm^3; the lubrication oil is energized inside the pump and sent to the lubrication circuit.

The lubrication pump consists of two gears (figure 2.63), with the inner rotor rotating off-center, creating 13 vanes evolving during one complete revolution from a minimum to a maximum volume during the suction phase and vice versa during the discharge phase. The rotors have 12 and 13 teethes respectively, the outer rotor rotates with an angular velocity that is equal to 12/13 of the inner rotor velocity (the transmission ratio between the rotors is 12/13).

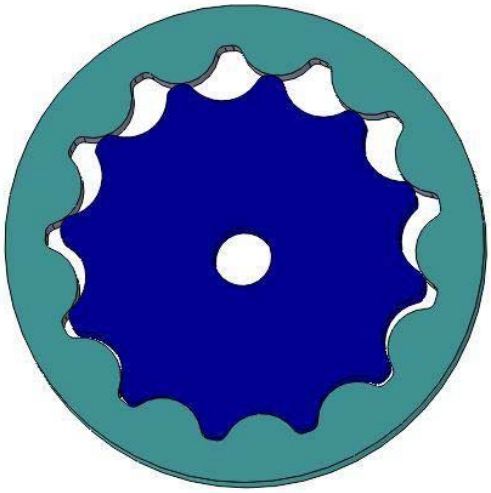

FIGURE 2.63: PUMP ROTORS

2.4.3 Three - Dimensional CFD Pump Model

Starting from the pump 3D geometry, the fluid volume has been extracted and meshed. Figure 2.64 shows the binary tree mesh of the considered pump. In the boundary layer, the binary tree approach can easily increase the grid density on the surface without excessively increasing the total cell count.

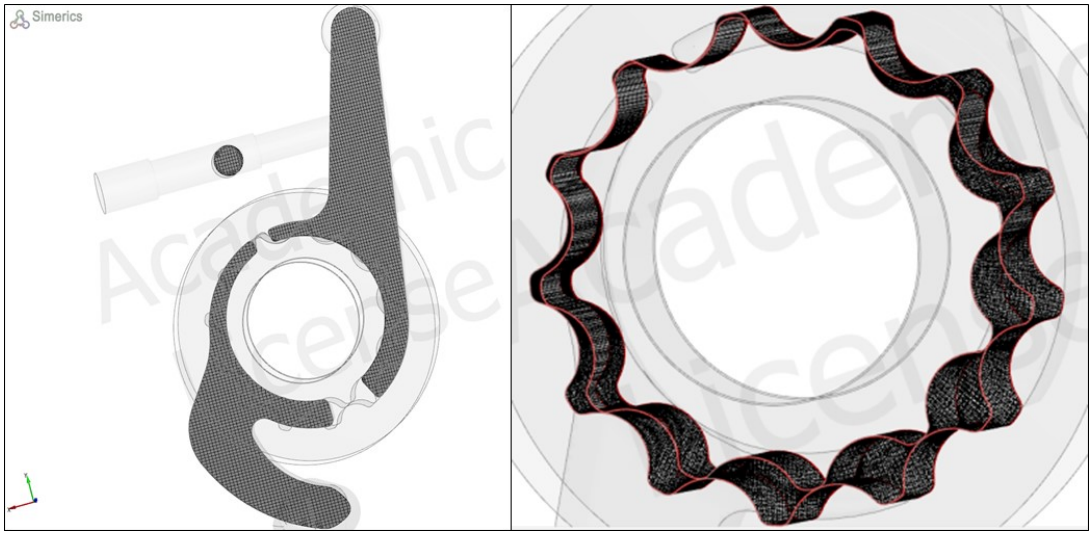

FIGURE 2.64: PUMP MESH

The model of the considered pump consists of a 302.000 3D cells (448.288 nodes). Once created the model, simulation have been run for oil temperatures of 60°C, 80°C and 110°C. Figure 2.65 shows the pressure distribution in the pumping volume and the ports.

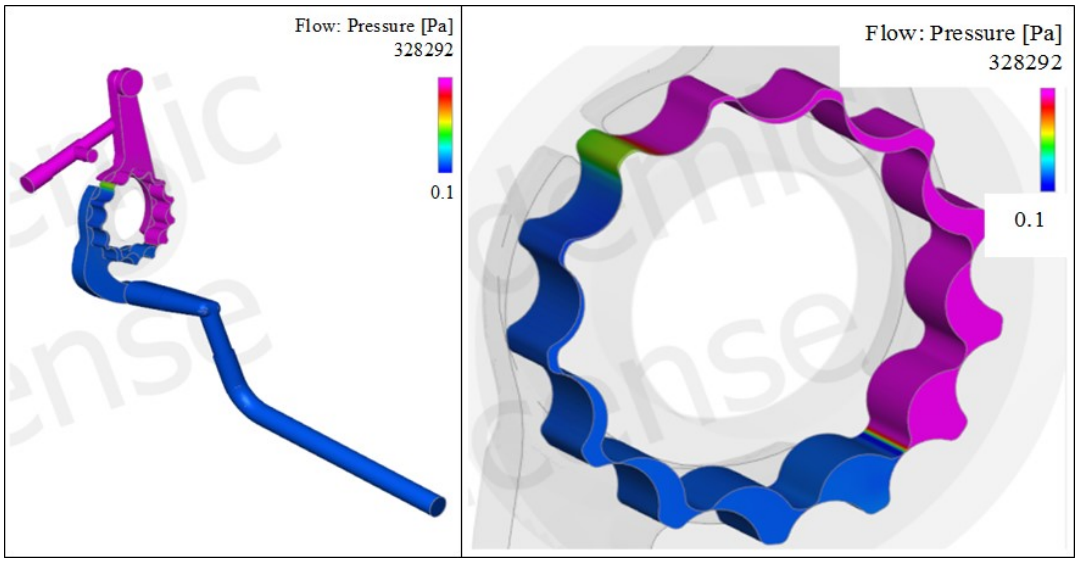

FIGURE 2.65: PRESSURE DISTRIBUTION IN THE FLUID VOLUME AND IN THE PUMPING CHAMBERS

From figure 2.65 it is possible to observe the pressure distribution from the pump suction port to the delivery one and also the distribution inside 13 fluid chambers where the oil is pressurized and sent into the lubrication circuit. Two areas of pressure transaction are clearly shown. These areas are colored by green. In the pump has integrated a relief valve therefore if the pressure is too high a portion of the delivered oil flow rate has been recirculated.

2.4.4 Three - Dimensional CFD Pump Model Validation

The pump model validation has been performed, as already mentioned, using data from an experimental campaign held at the Department of Industrial Engineering of University of Naples "Federico II". The test bench hydraulics scheme has been presented in figure 2.53 of paragraph 2.3. A 5W40 grade oil that complies with API SL, JASO MA-2, and ACEA A3 specifications, was used for the tests.

The tests allowed to determine the full pump characteristics map, in terms of pressure/flow rate curves (figures 2.66 – 2.68) as a function of rotational speed and oil temperatures of 60°C, 80°C and 110°C. Graphs are normalized by their maximum value.

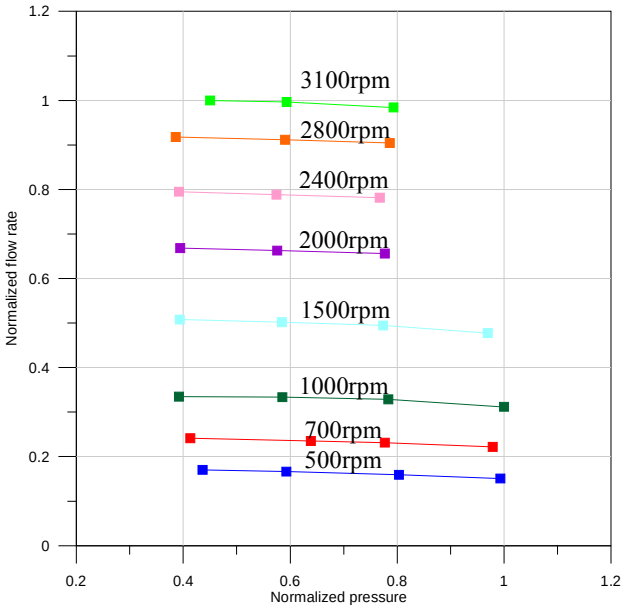

FIGURE 2.66: P-Q CURVES AT 60°C

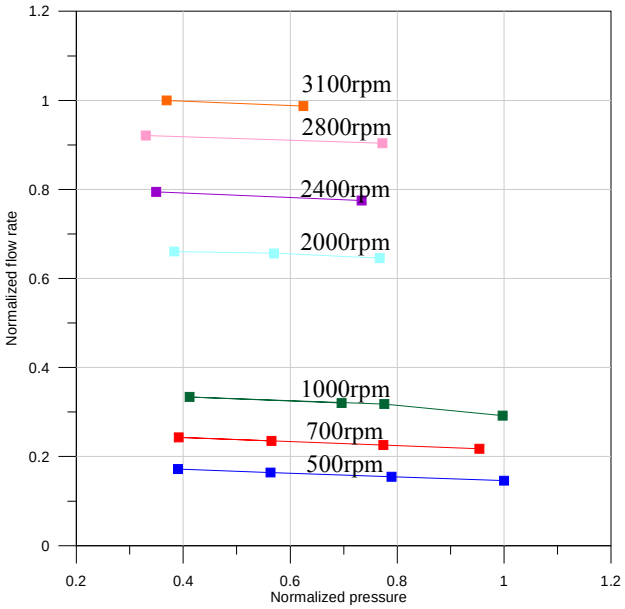

FIGURE 2.67: P-Q CURVES AT 80°C

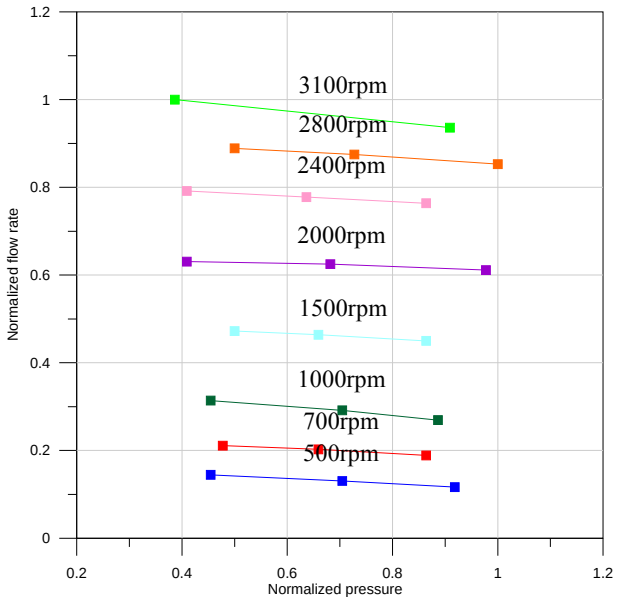

FIGURE 2.68: P-Q CURVES AT 110°C

The experimental curves show a soft slope versus the oil pressure and this trend is appreciable in all the tested conditions.

The model validation has been carried out comparing model results with experimental data at the different rotational speeds and oil temperatures (60°C, 80°C and 110°C). Plots in figures 2.69 – 2.71 show the comparison between numerical model results (dashed lines) and experiments (continuous line).

For all simulations, it was necessary to run from 4 to 5 complete revolutions to achieve regime conditions. Calculation times for each working point were always less than 4 hours.

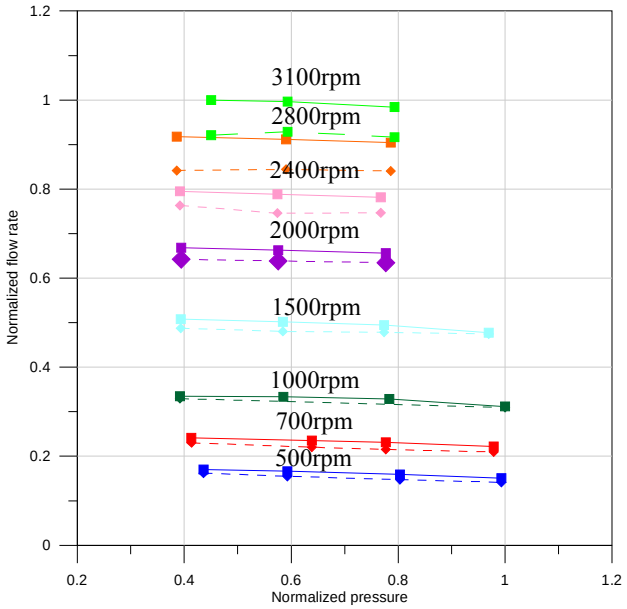

FIGURE 2.69: MODEL/EXPERIMENT RESULTS COMPARISON AT 60°C

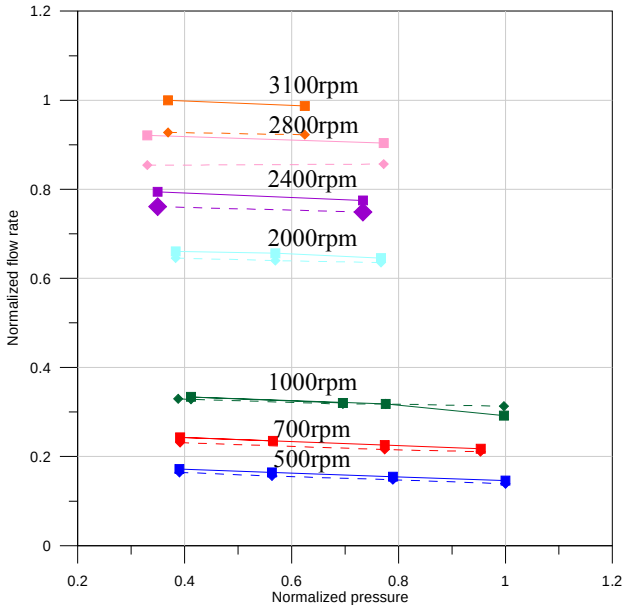

FIGURE 2.70: MODEL/EXPERIMENT RESULTS COMPARISON AT 80°C

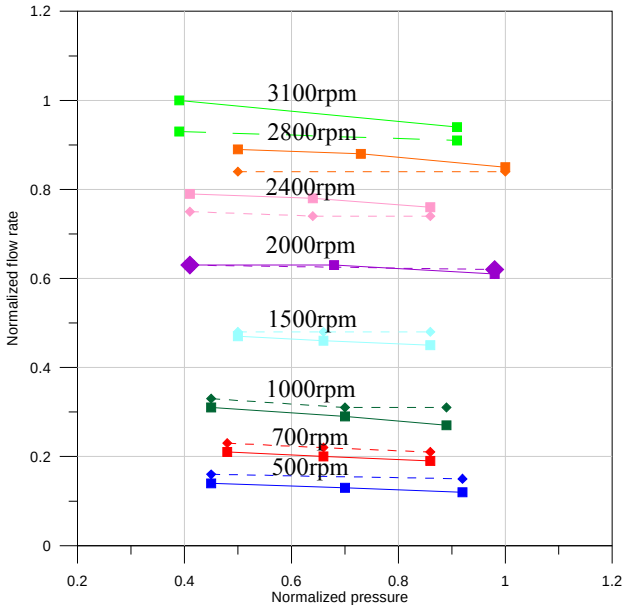

FIGURE 2.71: MODEL/EXPERIMENT RESULTS COMPARISON AT 110°C

From the analysis of the above plots (figures 2.69 – 2.71), it can be noted that the numerical model curves slope, with respect to the pressure axis, is very similar to the experimental results. This confirms that model correctly simulates the pump and captures all main leakages, inter-gears losses and side losses between rotors and pump casing (figure 2.72).

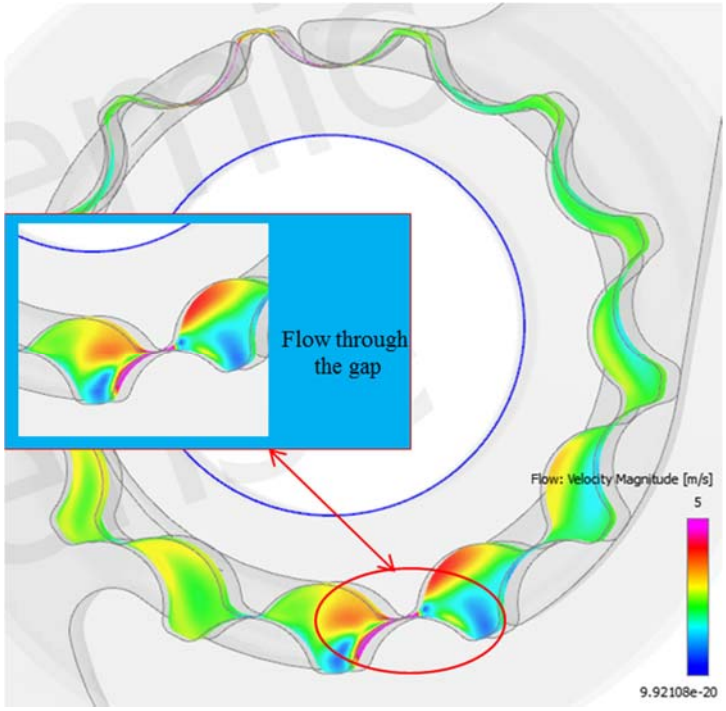

FIGURE 2.72: LEAKAGES

For all the operating conditions simulated, i.e. 500, 700, 1000, 1500, 2000, 2400, 2800 and 3100 rpm rotational speeds, the maximum difference between the numerical model flow - rate estimate and the experimental data is 8.5%. This is true also for varying oil temperatures as shown in figures 2.73 and 2.74.

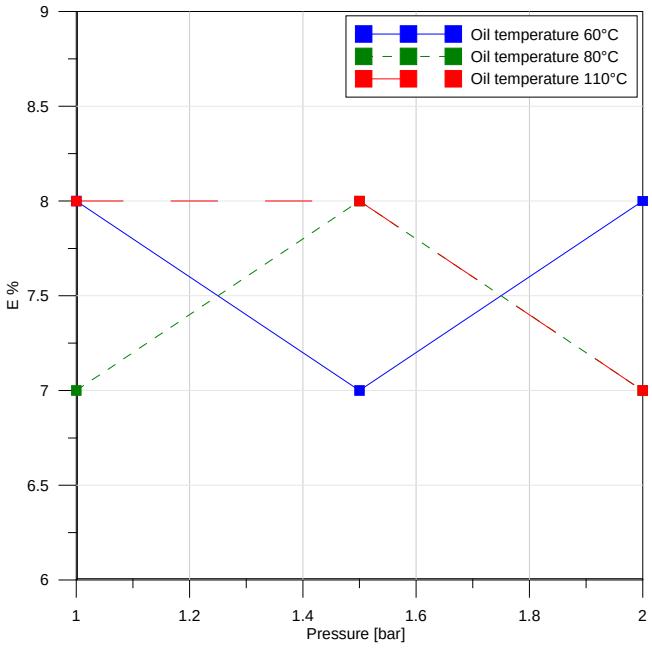

FIGURE 2.73: MAXIMUM % DEVIATION AS A FUNCTION OF DELIVERY PRESSURE WITH VARYING OIL TEMPERATURE

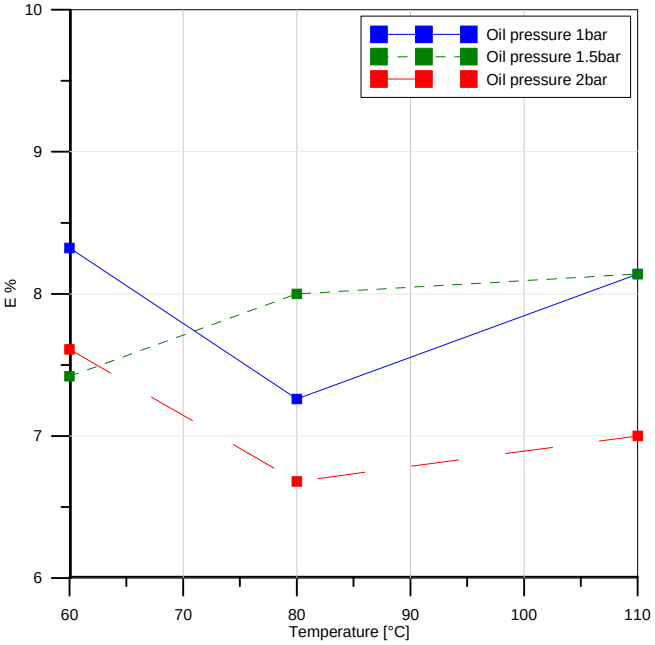

FIGURE 2.74: MAXIMUM % DEVIATION AS A FUNCTION OF OIL TEMPERATURE WITH VARYING DELIVERY PRESSURE

Figures 2.73 and 2.74 show that there is no significant trend for the percentage error, both versus oil pressure and temperature.

2.4.5 Three - Dimensional CFD Lubrication Circuit Model

The lubrication circuit model has been set-up as done for the oil pump.

In the complete model set-up, both the cavitation model, described previously chapter 1, and the turbulence model have been included.

The model will be described from all oil path through the engine crankcase and head-lines towards and different lubrication users.

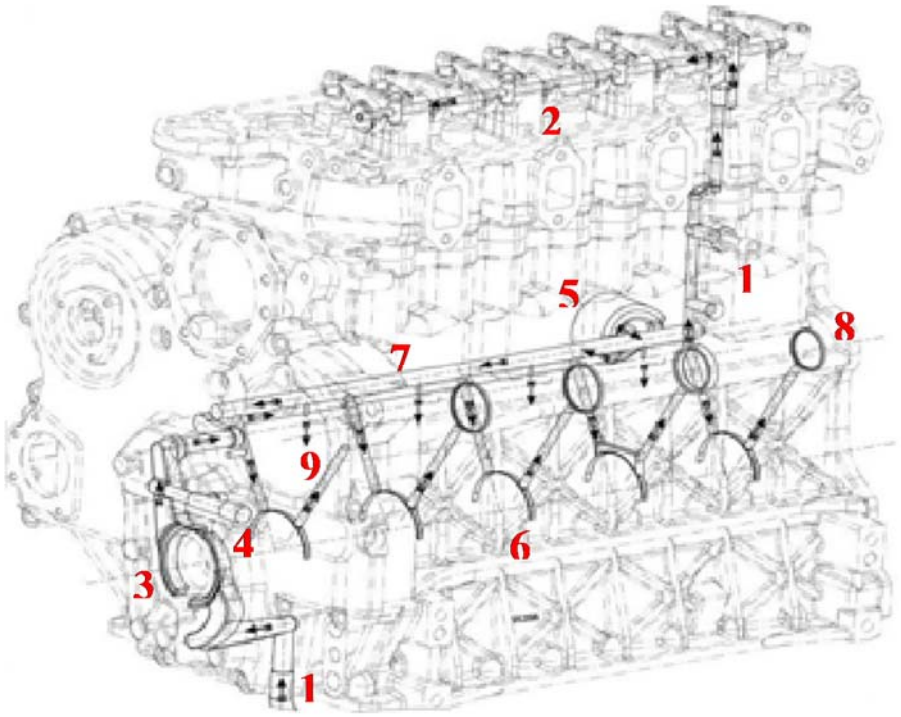

FIGURE 2.75: OIL PATH

The lubricant fluid goes from the oil pan to the suction pipe (point 1 in figure 2.75) and it is then processed by the pump (3). A by-pass is positioned on the pump delivery port, with a pressure relief valve (4).

Once passed the valve, the oil lubricant goes through the filter-exchanger (5) and arrives in the “main gallery”. Five branches depart from the gallery, to feed oil into the five crank - shaft bearings (6), the four piston cooling jets (7) and the middle distribution gear.

At the exit of the crank - shaft bearings, through some internal engine block lines, the oil lubricates the 4 cam-shaft bearings (8). This engine, in fact, uses a rod and rocker arm distribution system. The last crank - shaft bearing, above the middle distribution

gear, lubricates a plain shaft bearing (9).

From the second cam - shaft bearing, starts the engine head feeding line. This duct also feeds the turbine (10).

As the oil reaches the cylinder heads, some of it leaks through the four fastening screws of the rocker arm pin, while the rest lubricates the valve control and the bushing.

All lubrication circuit users have been modelled in detail; starting from the component executive drawing, a 3D geometry has been generated with a CAD program, exported in STL format and finally meshed in the CFD code PumpLinx®.

The complete model, shown in figure 2.76, consists of 1.848.669 cells. Transient simulations (6 pump revolutions) have been run on a multi-core Windows® 64bit PC (CPU Intel(R) Xeon(R) X5650, 12Gb RAM) and the computational time for each rotational speed is of 16 hours.

FIGURE 2.76: COMPLETE MODEL

Each lubrication circuit user will be described in detail by following. A specific focus will be dedicated to piston cooling jets, intake and exhaust valves tappets and to crank - shaft and cam - shaft bearings. In a first step, some simulations have been made on single sub-models users, in order to optimize and validate these simulation models.

Piston Cooling Jets Model

The modeling of the piston cooling jets has been performed, realizing first a 3D geometry starting from the executive drawing of the component. The realized geometry is shown in figure 2.77. It consists of two ducts, with different diameters, inclined at an angle with respect to the main gallery axis.

FIGURE 2.77: PISTON COOLING JET MODEL

A CFD model of the component has been set-up and run. Consequently, the simulation output has been compared with the pressure/flow rate curves provided by the manufacturer (figure 2.78).

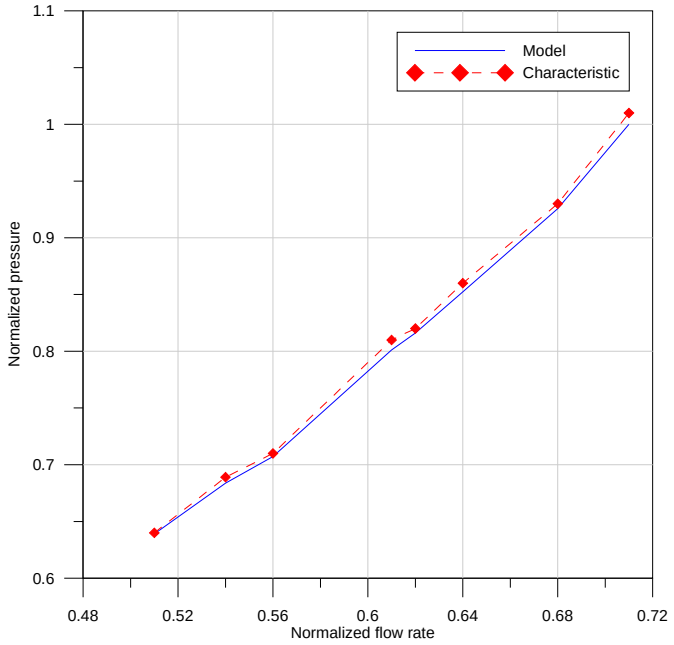

FIGURE 2.78: PRESSURE AS A FUNCTION OF FLOW - RATE FOR THE PISTON COOLING JETS

The trend confirms the good accuracy of the piston cooling jet sub-model: the percentage error is lower than 2% in all the examined conditions.

Hydraulic Tappets Model

Intake and exhaust valves tappets are fed directly from the engine head through a duct that runs inside the rocker arm of the valve control.

The oil enters the bushing as in figure 2.79, lubricates it and leaves through a duct inclined by 108° degrees from the inlet duct.

FIGURE 2.79: TAPPET BUSHING MODEL

Similarly to what has been done for the cooling jets, for the valve tappets the manufacturer's pressure/flow rate curves have been used for comparison with the component simulation results (figure 2.80).

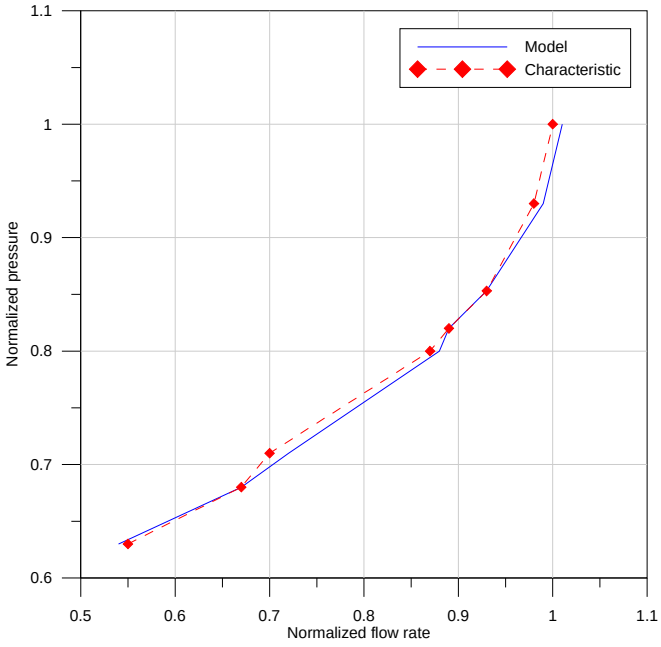

FIGURE 2.80: TAPPETS PRESSURE AS A FUNCTION OF FLOW-RATE

Crank - Shaft and Cam - Shaft Bearings Models

For bearings crank - shaft and cam - shaft modeling, it was followed a different approach. As it is well known, the modeling of such complex components requires specific and accurate calculations, often carried out with dedicated software. Therefore, it has been realized a detailed simulation model of the oil pump and circuit; the creation of detailed model of the circuit users was not among the research objectives.

In the complete model, the bearings have been modeled using equivalent areas, in order to estimate the oil flow - rate consumption of the single component.

Bearings oil consumption have been evaluated analytically using the Warner-Sommerfeld theory [20].

The Warner-Sommerfeld theory [20], used for this calculation, assumes that the total volumetric flux processed by a bearing is given by the sum of two parts:

- The minimum flow rate that goes through the groove/hole, given by the following equation:

$$Q_h = 0.5Vh(h_d - h_u) \tag{2.18}$$

- The pressurized flow rate Q_p that changes according to the type of bearing.

In the specific case, the crank - shaft bearings present a groove in the upper semicircle. Hence, the pressurized flow rate has been calculated with the following equation:

$$Q_p = \frac{c^3 p_s}{\eta}\left[\left(\frac{1.25-0.25*\left(\frac{l}{L}\right)}{6\left(\frac{L}{l}-1\right)^{0.333}} f_1\right) + \left(\frac{\frac{D}{L}}{6\left(1-\frac{l}{L}\right)} f_2\right)\right] \tag{2.19}$$

where the coefficients f_1 and f_2 are determined from the graph in figure 2.81 using the eccentricity ratio and the groove extend β as inputs.

For the cam - shaft bearings, with a single intake hole, the following equation has been used [20]:

$$Q_p = 0.675\frac{p_s {h_s}^3}{\eta}\left(\frac{d_h}{L} + 0.4\right)^{1.75} \tag{2.20}$$

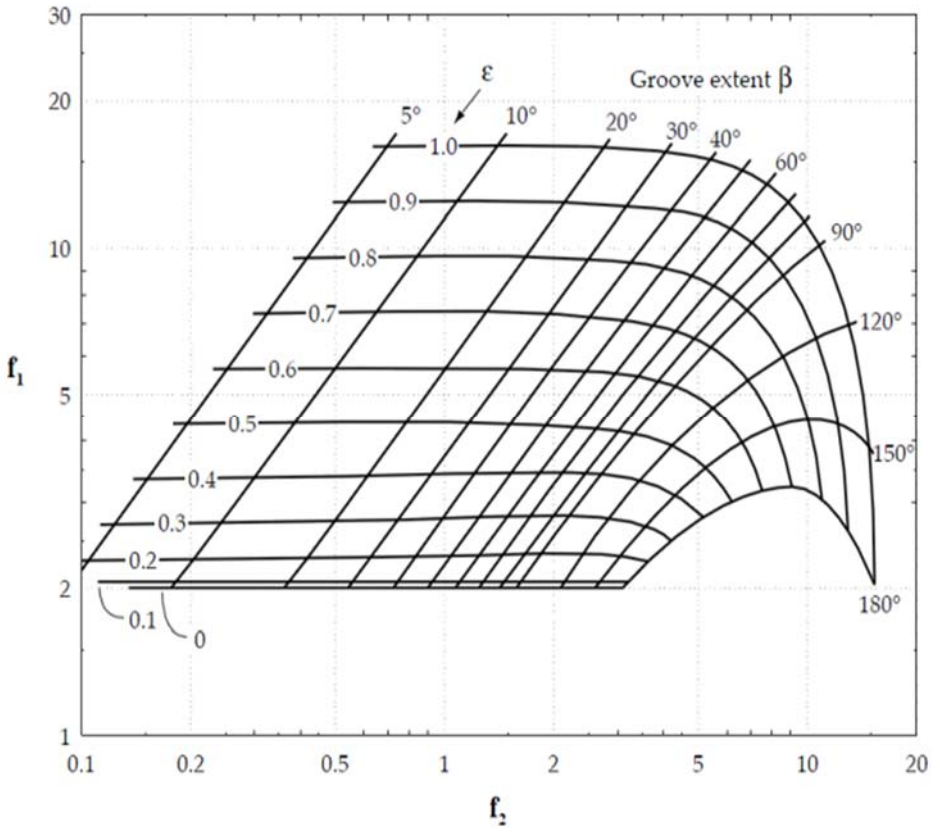

FIGURE 2.81: COEFFICIENTS F_1, F_2 [20]

Consequently, implementing formulas 2.18 and 2.20 and using the geometrical data and the oil running conditions, it was first evaluated the oil consumption of the cam-s haft and crank - shaft bearing and then an equivalent area that allows to take into account the oil consumption of these components.

2.4.6 Three - Dimensional CFD Lubrication Circuit Model Validation

The validation phase of the entire model has been made starting from experimental data, performed by the engine manufacturer on an engine test bench. The experimental tests have been carried out at different rotational speeds (from 1000 to 2800 rpm) at full load, measuring oil pressure in the main gallery, near the oil filter.

In figure 2.82 the comparison between the model results and experimental data is shown: the oil pressure behavior versus rotational speed, in the main gallery, has been monitored. The data are presented normalizing the oil pressure with respect to the experimental maximum value.

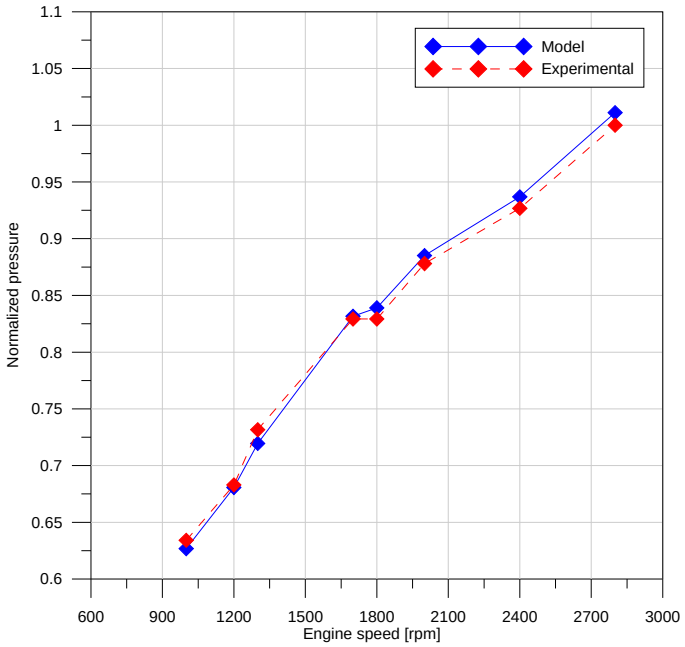

FIGURE 2.82: WHOLE MODEL VALIDATION - "MAIN GALLERY"

The error is always very little, less than 2%, for all the rotational speeds, and there are no significant differences varying form idle conditions to maximum speed.

In figure 2.83, a first application result of the 3D model is shown. It is possible to appreciate the oil pressure distribution along the lubricant circuit, at 1700 engine rpm. It starts from atmospheric pressure (101 MPa, in blue) and reaches the maximum value (300 MPa, in red), while in the engine head it stabilizes at about 1,6MPa (in green).

In figure 2.84, the oil flow - rate consumption is examined, showing the oil mean velocity (m/s) at the different circuit users, in order to evaluate and compare the oil consumption in the different zones of the model. It is clear that the higher oil consumption is estimated for the crank - shaft bearings.

Furthermore, in figure 2.85, the mean flow velocity (m/s), in the circuit ducts, is presented, showing the streamlines which allow to analyze the critical zones where the circuit presents the major pressure drops. It can be noted that the maximum velocity is reached upstream the main gallery, where the fluid has to overcome all the circuit resistances.

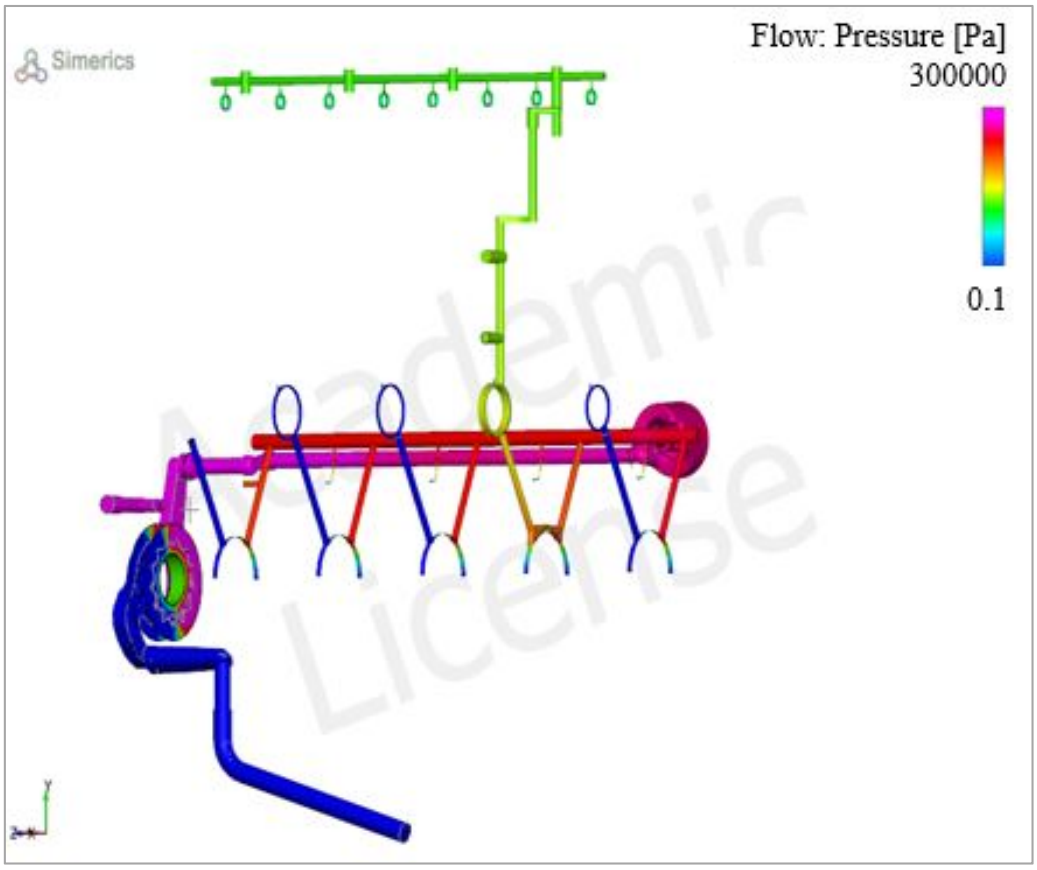

FIGURE 2.83: PRESSURE DISTRIBUTION

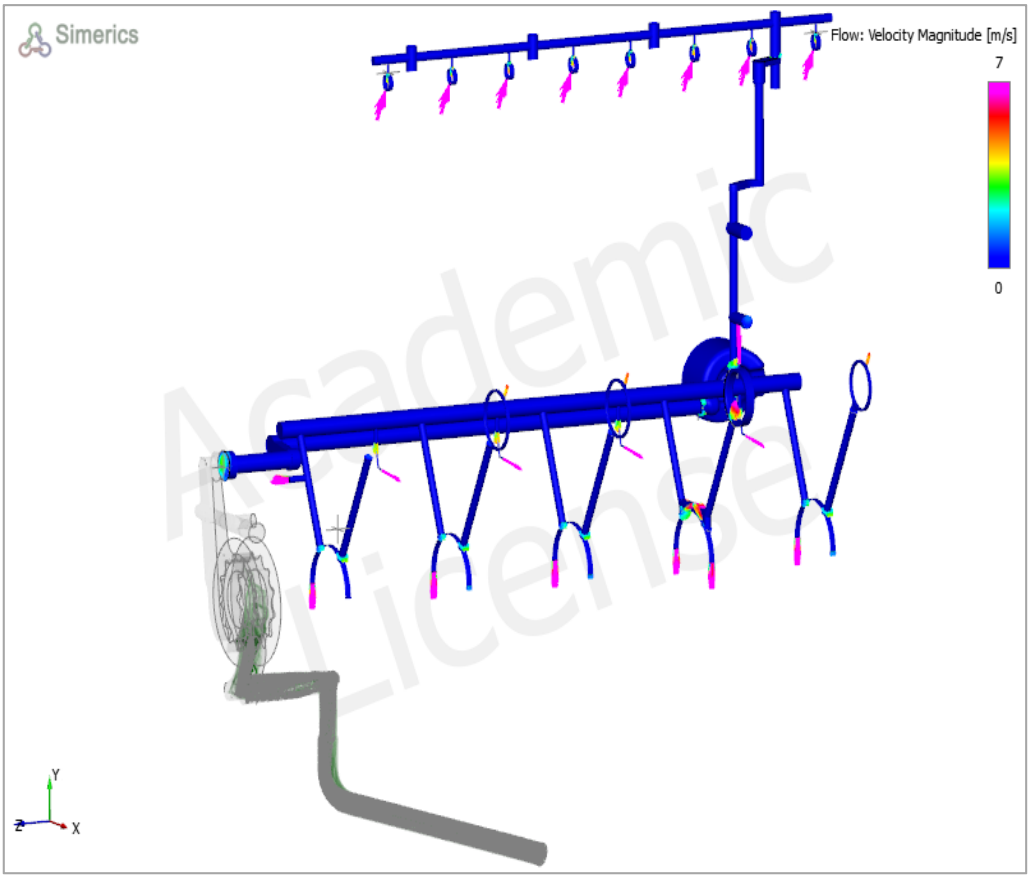

FIGURE 2.84: OIL MEAN VELOCITY

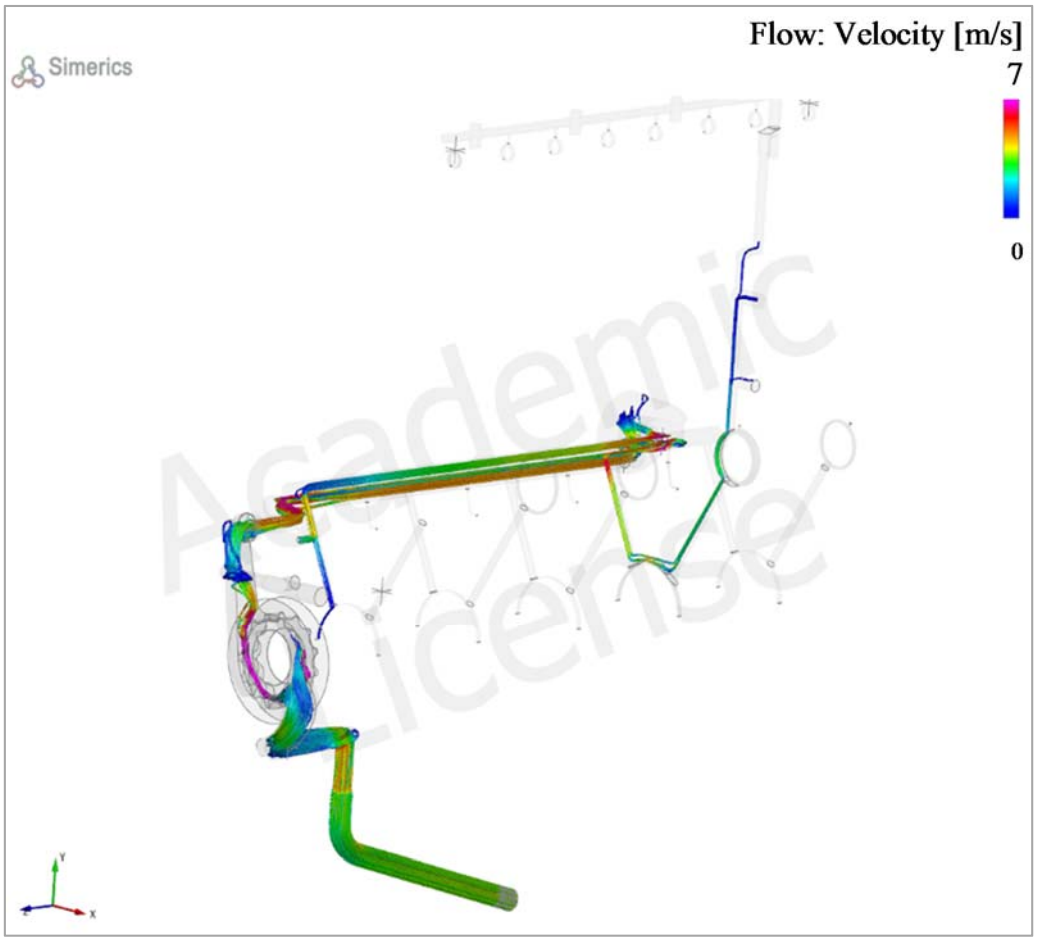

FIGURE 2.85: TYPICAL STREAMLINE COLORED BY VELOCITY MAGNITUDE

Analyzing and post-processing the simulated data is possible to obtain useful information about the running conditions of the whole circuit.

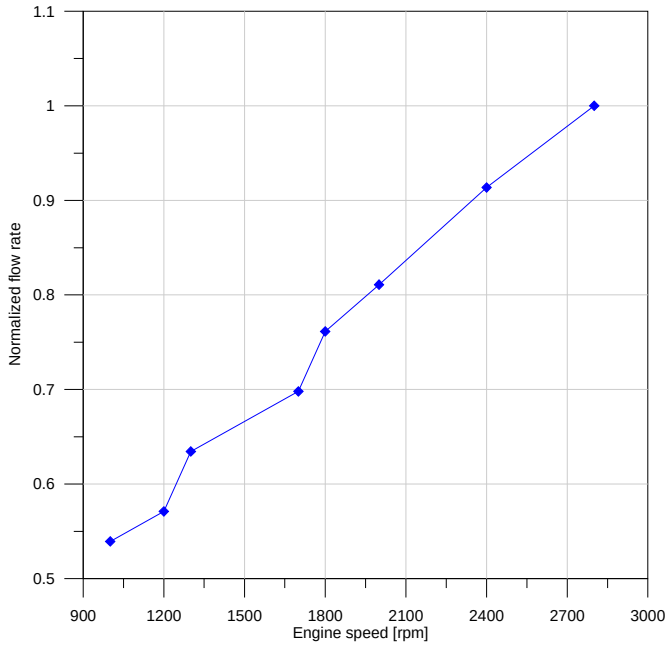

FIGURE 2.86: FIRST CRANK - SHAFT BEARING OIL CONSUMPTION

In figures 2.86 and 2.87 shown respectively the oil consumption of the first crank shaft bearing and the oil flow rate behavior that reaches the engine head, to lubricate the turbine and the hydraulic tappets, both in function of the engine speed. It can be noted that the curve slopes for figures 2.86 and 2.87 are quite different, pointing out the different running condition for the different areas of the circuit.

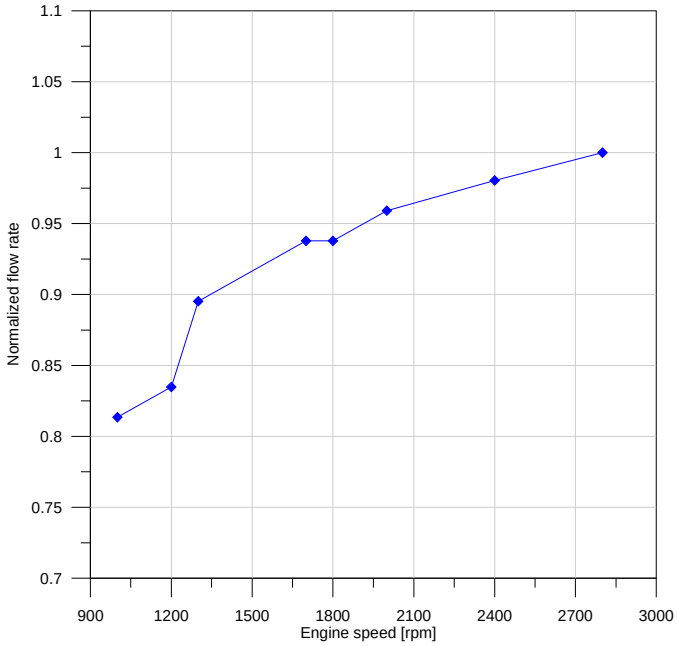

FIGURE 2.87: TURBINE AND HYDRAULIC TAPPETS OIL CONSUMPTION

2.4.7 Conclusions

A accurate analysis of a lubrication circuit of a diesel engine has been shown in this paragraph. The study has been performed by using the modeling approach described in this PhD thesis.

This model has been built up with a commercial tridimensional software. The pump model results have been compared to experimental data obtained at an hydraulic pump test bench of the Department of Industrial Engineering of University of Naples "Federico II", showing a good correlation between experimental and simulated data.

Then the model of the entire circuit has been analyzed. The model simulates all the ducts and pipes of the oil lubricant circuit while users have been modeled using different techniques, which made possible to take into account their oil consumption. In particular, some user types, as piston cooling jets, have been modeled reproducing

the exact geometry of the component. Other more complex users, as the crank - shaft bearings, have been modeled using an equivalent area. The procedure allows to easily model complex components like crank - shaft bearings.

By the end, the pump and circuit models have been coupled together. Several runs have been performed for the complete system, at varying revolution speeds.

The entire model have been validated by experimental data, performed on the lubrication circuit in an engine test bench. In all examined engine operating condition, model results fit very well the experimental data, showing a very low error percentage.

Therefore, this methodology developed by the Engine Hydraulic Research Group of the Department of Industrial Engineering of University of Naples “Federico II” demonstrated to reproduce with a high accuracy also complex systems like lubrication circuits of engine. It can be adopted during the design phase of a new engine, assisting engineers for the pump and ducts design optimization.

The complete model consists in less than 2 million of 3D cells and it run, unexpectedly, in only 16 hours. The cells number is, in fact, low if compared to the high complexity of the system but it has allowed to achieve an overall accuracy less than 2% that is a surprising result.

2.5 Pumps as Turbine (PAT)

2.5.1 Introduction

Electricity generation presents many issues and is studied with different techniques in order to reduce its production cost and environmental impact. Conventional production with fossil fuels presents problems associated with the high cost, rapid depletion and detrimental environmental effects of these fuels. Renewable energy is probably the best solution for the environmental issues, and many solutions have been developed since the last century, such as hydropower, hydrogen, fuel cells, biofuels, and solar power generation.

Among the renewable sources, small hydropower represents a very attractive source of energy generation. In many countries, small and micro hydropower is an important means of electricity generation. An efficient solution, from the point of view of energy efficiency, is the adoption of a turbine, but the purchase and maintenance costs of turbines render their application economically unattractive, especially for small hydropower [21 - 28].

Reverse-running centrifugal pumps (also called PAT, pump as turbine) are a solution for generating and recovering power in small and micro hydropower situations. Pumps are relatively simple machines, inexpensive (compared to a hydraulic turbine), and readily available worldwide. It is estimated that the capital payback period of a reverse-running pump in the 5-50 kW range is less than two years [29, 30]. Moreover, the use of PAT could be suitable because manufacturers of turbines worldwide are less numerous than pump producers, the market for turbines is small compared to that for pumps, and pumps are mechanically simple and require less maintenance. Moreover, an integral pump and electric motor can be purchased for use as a turbine and generator set; pumps are available in a wide range of heads and flows and in a large number of standard sizes. Generally, pumps have short delivery times, spare parts (such as seals and bearings) are easily available and the installation can be done using standard pipes and fittings.

The use of a pump running in reverse mode to generate electricity is not new; the first applications started almost 80 or 90 years ago and many theoretical and experimental studies have been done [23 - 28, 31, 32]. Much research is still being conducted, especially to predict the operating conditions and the efficiency of centrifugal pumps running in reverse [33].

The selection of a proper PAT for an existing site represents a critical issue because pump manufacturers do not supply the characteristic of the pump running in reverse. Many methods have been used to predict the inverse characteristic of a pump, based on numerical models, experiments, or theoretical procedures [27 - 28].

Several studies based on a modeling approach with CFD code are available and generally showed good agreement with the available experimental data [26, 32]. A study [26] carried out with a computational model of a PAT is based on the concept called “flow zone”. The flow regime within a PAT is divided into four major flow regions (volute casing, impeller, casing outlet and draft tube). A comparison was made between the experimental and numerical results of a single stage end suction centrifugal pump that was operated in turbine mode at a speed of 800 rpm. CFD predictions of the hydraulic parameters were in good agreement with the experimental results, but deviations (within 5% to 10%) were found at certain load regions. Nautiyal et al. [27] carried out a study on the application of CFD and its limitations for PAT using cases reported by previous researchers [26, 31, 32]. The study reported that CFD analysis was an effective design tool for predicting the performance of centrifugal pumps in turbine mode and for identifying the losses in turbo-machinery components such as the draft tube, impeller and casing, but there was some deviation between the experimental results and the CFD modeling results. Barrio et al. [33] carried out a numerical investigation on the unsteady flow in commercial centrifugal pumps operating in direct and reverse mode with the help of CFD code. The results of their simulation were in good agreement with the experimental results. The study revealed that in the reverse mode, the flow only matched the geometry of the impeller at nominal conditions; re-circulating fluid regions developed at low flow rates (near the discharge

side of the blades) and high flow rates (near the suction side). Many correlations based on theoretical approaches are available to predict the performance of a PAT. Several researchers (Stepanoff, Childs, Sharma, Wong, Williams, Alatorre-Frenk, and others) have presented correlations for predicting the performance of a pump-as-turbine [27]. These correlations were based upon either pump efficiency or specific speed. However, the deviation between experimental and predicted reverse operation of standard pumps has been found to be more than 20% [34]. The objective of these correlations is to calculate the best efficiency point (BEP) of pumps for operation in turbine mode by using the pump operation data provided by the manufacturer. In 1962, Childs [35] presented a PAT prediction method based on the efficiency of the pump. A similar approach was then presented by McClaskey and Lundquist [36] and Lueneburg and Nelson [37] in 1976 and 1985, respectively. Hancock [38] stated that for most pumps the turbine BEP lies within 2% of the pump mode BEP. Grover and Hergt [39, 40] proposed a PAT prediction method based on specific speed for the turbine mode (obtained similar to the specific speed for a pump). Grover's method is applicable for the turbine mode specific speed range 10-50 [39]. A comparison between experimental results and the methods proposed by the above researchers show relatively large deviations; therefore, the use of these formulae has been confined to approximate selection of PATs.

Finally, a large number of experimental studies can be used to evaluate the inverse characteristic. These are often limited to the specific pumps tested, so that they cannot serve as a valid tool for pump selection, but are very useful for tuning and validating theoretical and modeling analyses.

By following it will be shown the methodology for obtaining the reverse characteristic of a pump, starting from the results of three-dimensional CFD models. The results are compared with data available in the literature.

2.5.2 Prediction method

The applied methodology is based on the results of already described 3D CFD modeling approach applied to simulate centrifugal machines. In this paragraph, a short

description is given of several prediction methods available in literature. These methods will be used to analyze the proposed methodology and to discuss the results.

The following equations summarize different methods to predict the pump inverse characteristic. They are based on theoretical or experimental analysis [26, 34].

a) Stepanoff:

$$\frac{H_t}{H_p} = \frac{1}{\eta_p}\ ; \frac{Q_t}{Q_p} = \frac{1}{\sqrt{\eta_p}}; \ \eta_T = \eta_P; \ N_{st} = N_s\eta_p \tag{2.21}$$

b) Alatorre and Frenk

$$\begin{cases} \frac{H_t}{H_p} = \frac{1}{0.85{\eta_p}^5+0.385}; \\ \frac{Q_t}{Q_p} = \frac{0.85{\eta_p}^5+0.385}{2{\eta_p}^{9.5}+0.205}; \\ \eta_t = \eta_p - 0.03 \end{cases} \tag{2.22}$$

c) Sharma

$$\frac{H_t}{H_p} = \frac{1}{{\eta_p}^{1.2}}; \frac{Q_t}{Q_p} = \frac{1}{{\eta_p}^{0.8}}; \ P_t = P_{p;}; \ \eta_t = \eta_p \tag{2.23}$$

d) Schmiedl

$$\frac{H_t}{H_p} = -1.4 + \frac{2.5}{\eta_p}; \frac{Q_t}{Q_p} = -1.5 + \frac{2.4}{{\eta_p}^2}; \frac{\eta_t}{p} = 1.158 - 0.265N_{st} \tag{2.24}$$

e) Grover

$$\begin{cases} \frac{\mathrm{H_T}}{\mathrm{H_P}} = 2.693 - 0.0229\mathrm{N_{ST}} \\ \frac{\mathrm{Q_T}}{\mathrm{Q_P}} = 2.379 - 0.0264\mathrm{N_{ST}} \\ \frac{\mathrm{H_T}}{\mathrm{H_P}} = 0.893 - 0.0466\mathrm{N_{ST}} \end{cases} \tag{2.25}$$

f) Hergt

$$\frac{\mathrm{H_T}}{\mathrm{H_P}} = 1.3 - \frac{6}{\mathrm{N_{ST}}-3}; \ \frac{\mathrm{Q_T}}{\mathrm{Q_P}} = 1.3 - \frac{1.6}{\mathrm{N_{ST}}-5} \tag{2.26}$$

g) Childs

$$\frac{H_t}{H_p} = \frac{1}{\eta_p}; \frac{Q_t}{Q_p} = \frac{1}{\eta_p}; \ \eta_t = \eta_p \tag{2.27}$$

Derakhshan and Nourbakhsh [40] introduced a method based on theoretical analysis to evaluate the BEP of an industrial centrifugal pump. This method is based

on the geometrical and hydraulic characteristics of the pump in direct mode. The final formula to evaluate the turbine's maximum efficiency is:

$$\eta_t = \frac{P_{nt}}{\gamma \cdot Q_t \cdot H_t} = \frac{\gamma \cdot Q_t \cdot H_t - P_{vt} - P_{lt} - P_{et} - P_{it} - P_{mt}}{\gamma \cdot Q_t \cdot H_t} \quad (2.28)$$

The presented methods are very different and based on different hypotheses. Each method can be used only for a limited set of pumps and none of them allows the reverse running conditions to be accurately predicted for all geometries and over a wide range of pump specific speeds.

2.5.3 Three - Dimensional CFD Model

Three different centrifugal pumps have been modeled in order to obtain the data necessary to predict the performance of the pumps by the described procedures. The analyzed pumps are commercial ones and have three different specific speeds. The main characteristics are summarized in table 2.3.

	Impeller diameter [mm]	Delivery outlet diameter [mm]	H_{bep} [m]	Q_{bep} [m^3/s]
(N_s 37.6)	190	80	39	148
(Ns 20.5)	200	70	60	45.4
(Ns 64.0)	120	80	3.9	54

TABLE 2.3: PUMPS CHARACTERISTICS

It was decided to use pumps with different heads (from 3.9 to 60 m) and flow rates (from 45.4 to 148 m^3/s) to have different geometries and operating conditions to better test the prediction method.

The simulation models have been built using the three-dimensional CFD modeling approach presented in this PhD Thesis.

Figure 2.88 the fluid volume is shown in green while figure 2.89 shows the mesh the entire geometry.

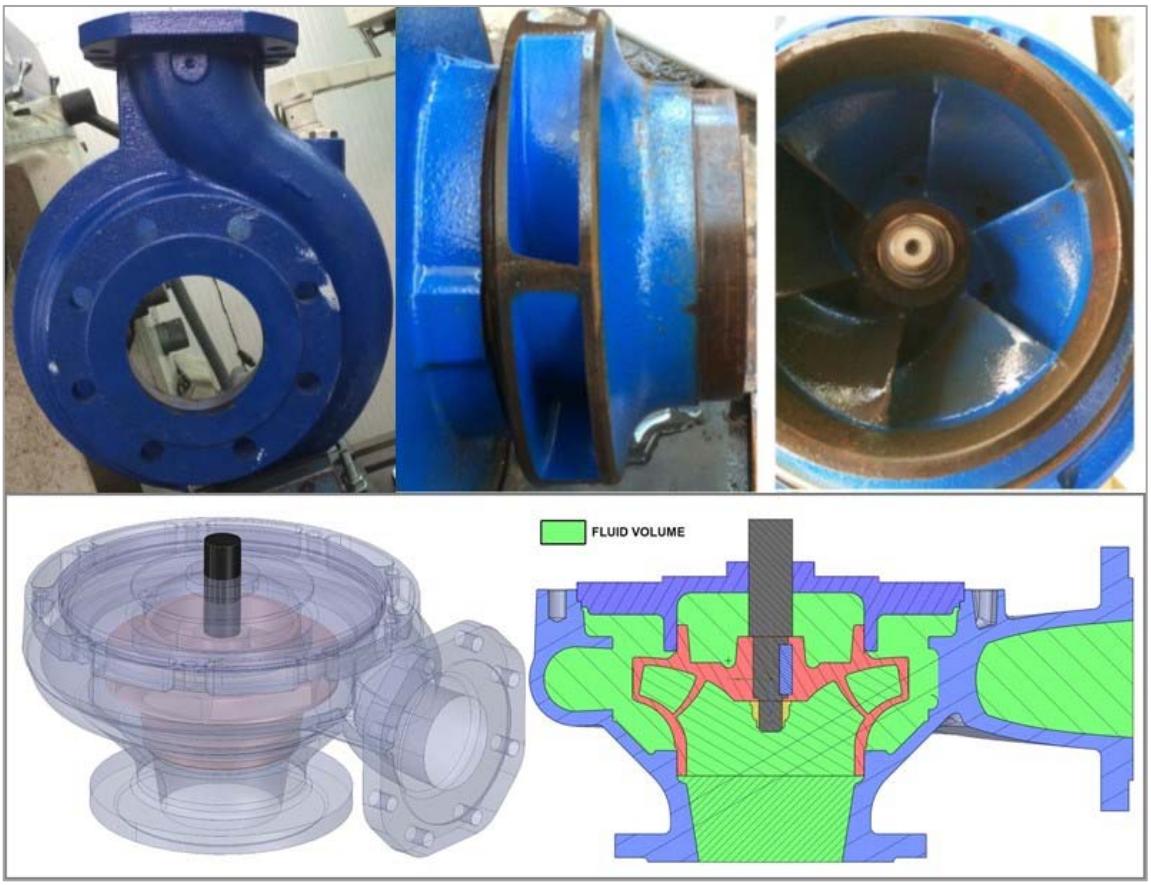

FIGURE 2.88: GEOMETRY AND FLUID VOLUME

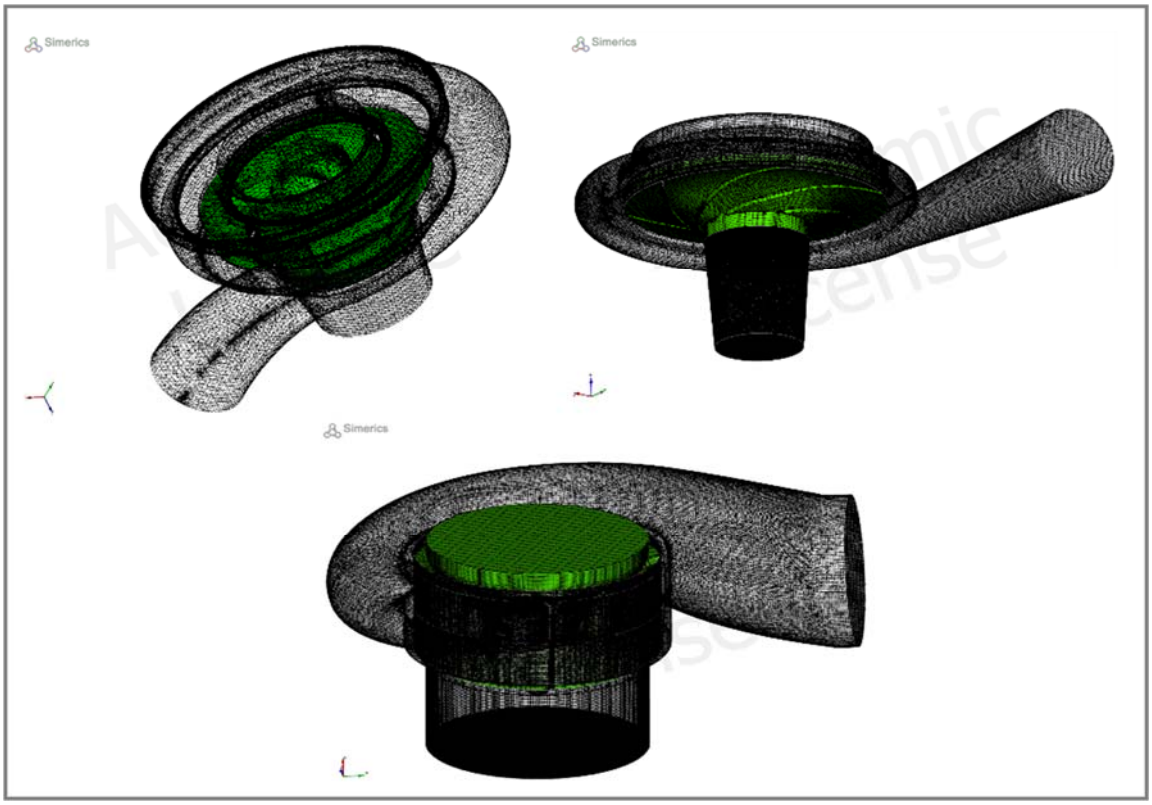

FIGURE 2.89: BINARY TREE MESH FOR THREE PUMPS

The details of the three-dimensional grids for each pump are shown below. Simulations have been run with an Intel(R) Xeon(R) CPU 2.66GHz (2 processors).

PUMP 1 (N_S=37.6):

- Total number of cells : 851.673
- Total number of faces : 3.383.745
- Total simulation time: 8.9 h as Pump, 9 h as PAT

PUMP 2 (N_S=20.5):

- Total number of cells: 1.039.450
- Total number of faces: 3.926.412
- Total simulation time: 4.2 h as Pump, 4.8 h as PAT

PUMP 3 (N_S= 64):

- Total number of cells: 324.596
- Total number of faces: 3.348.318
- Total simulation time: 4.5 h as Pump, 4.8 h as PAT

As said, using the presented models it is possible to investigate the internal fluid dynamics in the direct (as pump) and reverse (as turbine) modes. Model results for Pump 1 are shown in figure 2.90; in figure 2.90a the pressure distribution at the BEP is presented for both working modes in the pressure range (0 ÷ 9) bar.

Figure 2.90b shows the velocity vectors in the fluid volume; the velocity range (0 ÷ 32) m/s is the same for the direct and reverse modes. In this picture (figure 2.90b), it is possible to visualize the flow evolution inside the machine and the acceleration/deceleration of the fluid.

Both figures confirm that the velocity is higher in the reverse mode.

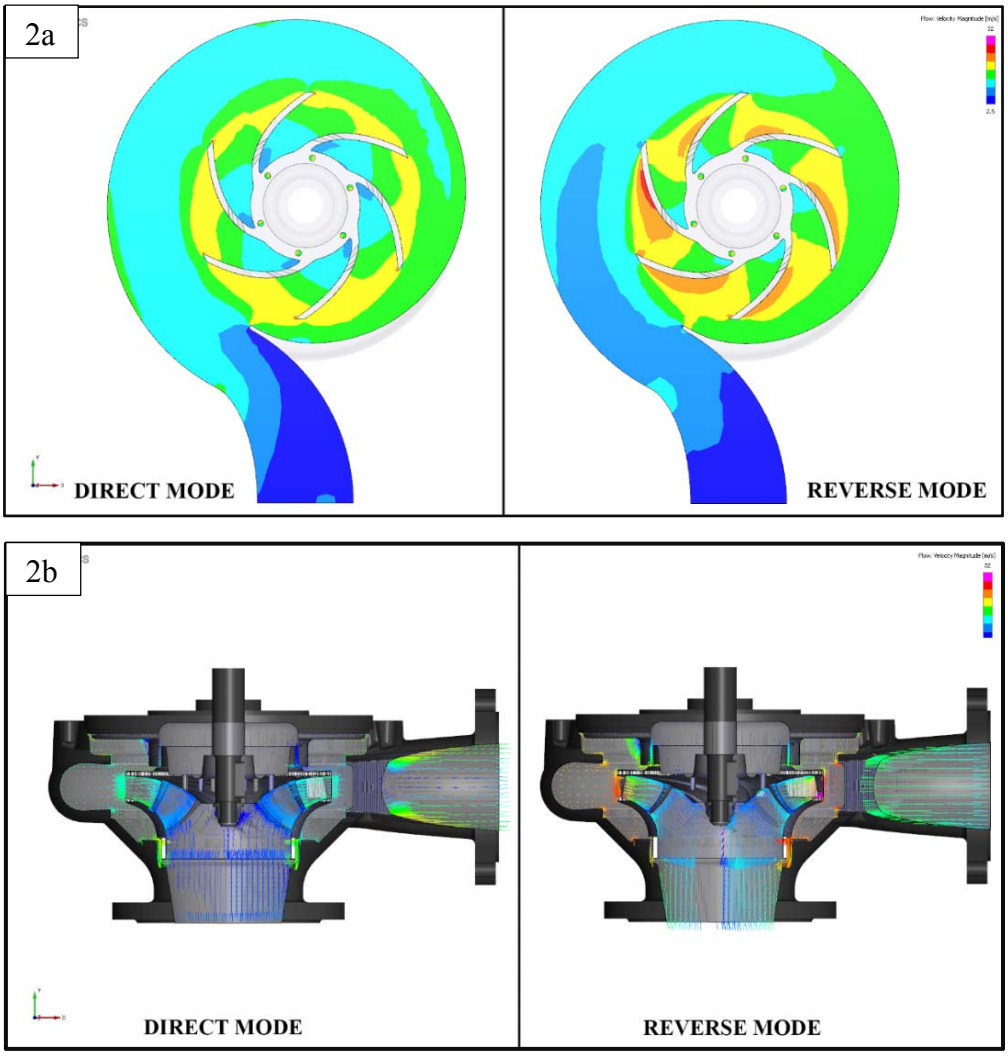

FIGURE 2.90: MODEL RESULTS PUMP 1 (N_S = 37.6)

Similarly, figure 2.91 shows the pressure distributions for pump 2 (N_S= 20.5) and pump 3 (N_S= 64).

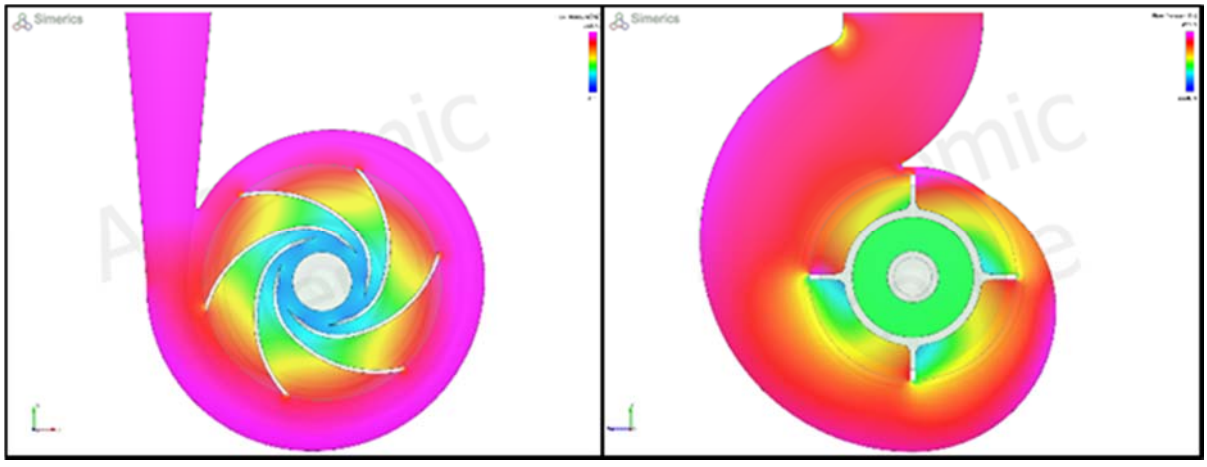

Ns= 20.5 Ns= 64

FIGURE 2.91: PRESSURE DISTRIBUTION IN THE FLUID VOLUME OF PUMPS 2 AND 3

For the direct mode, CFD models have been validated using the data supplied by the pump manufacturers. In Figure 2.92, the head vs. flow rate plot (as the blue curves) are shown. Across the range of flow rates (30 – 207 m^3/h), the head varies from 47 to 3 m. Plots in Figure 4, the model results is in red.

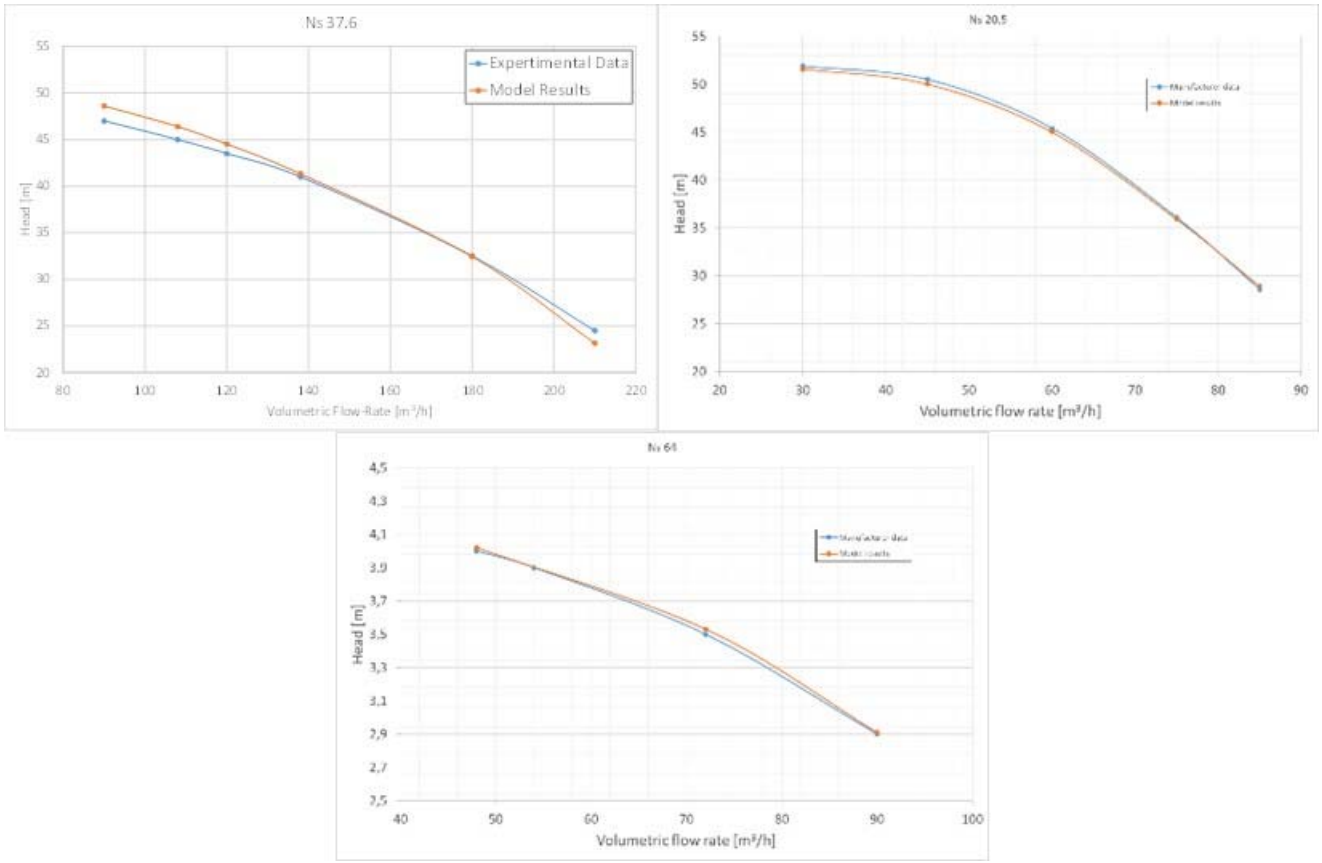

FIGURE 2.92: MODEL VALIDATION: COMPARISON BETWEEN MANUFACTURER DATA AND MODEL RESULTS

The comparison in Figure 2.92 demonstrates the accuracy of the adopted methodology; in fact, the percentage error is always less than 4% while for many points the error is near zero.

Ns 37.6 Pump Model Validation

Once the model had been validated in the pumping mode, it was decided to validate it also in the reverse mode, to assess whether the model reproduces the turbine mode well. Because the proposed methodology is based only on the results of the CFD model in reverse conditions, the validation in reverse condition was necessary to confirm the entire methodology.

The model of centrifugal Pump 1 has been validated with data from an experiment performed in a dedicated test bench that enables testing a centrifugal pump running in reverse mode. The aim of this activity was to further validate the simulation model in reverse conditions.

The test bench reproduces a full-scale hydraulic network, made up of four nodes (figure 2.93). An external pump increases the water pressure to simulate the behavior of a real urban network while an air chamber stabilizes the flow rate. The tested pump has been installed in one node where two pressure-reducing valves (PRV) regulate the water flow rate and the pressure at the inlet and outlet of the pump.

The electric motor of the pump is linked to an inverter and the produced electrical power is connected to the urban power grid. In the node, two pressure transducers, P_1 and P_2 (Burkert® model 8314), and a flow meter Q (Siemens® mag 500) have been installed. All test bench data have been acquired by a home-made acquisition system. Furthermore, a 360-tooth encoder has been installed on the electrical motor to acquire the shaft speed.

Experiments have been performed only in steady-state conditions, varying the water flow rate and the pressure at the inlet of the pump, for different shaft speeds. In particular, the flow rate has been varied between (8 - 21) l/s, and the shaft speed between 300 and 2200 rpm. During the test, pressure at the inlet and outlet of the pump have been acquired at a sample frequency of 1 Hz.

As stated above, the tests have been done in steady-state conditions, running the pump in reverse mode. The flow rate, the pressures at the inlet and outlet of the pump and the shaft rpm were measured. In figure 2.94, all results of the experimental campaign are shown.

To examine the PAT performance, the total head [m] versus shaft rpm is reported, varying the water flow rate for all the examined conditions. Results confirm what is known from the literature: the PAT head increases with the rpm and with the flow - rate, and it can be easily noted that, for the tested conditions, the head varies between 0.1 and 1.8 meters.

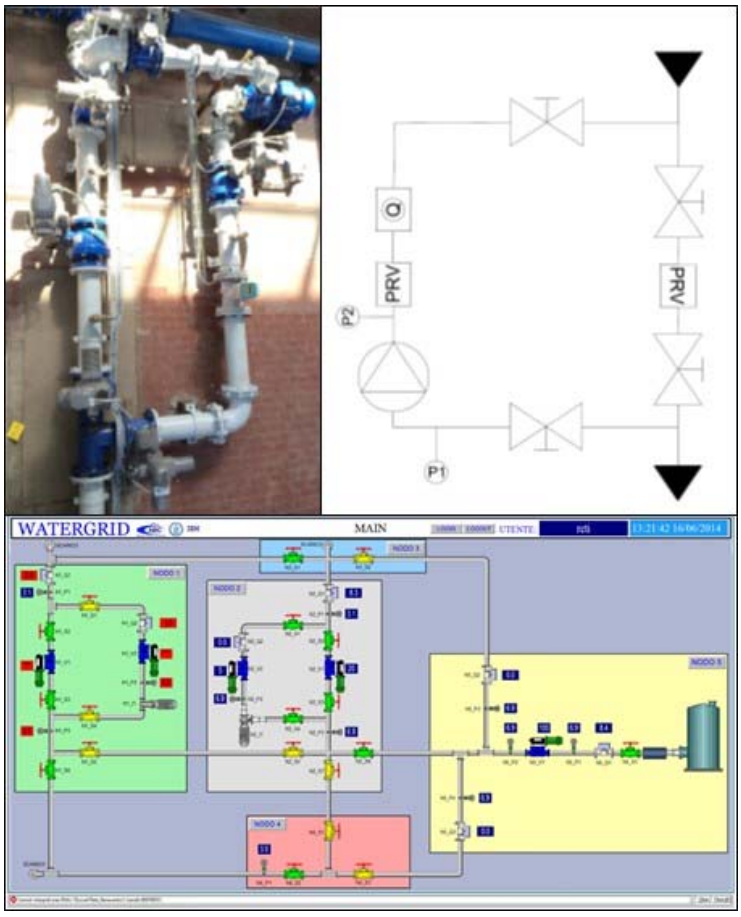

FIGURE 2.93: TEST BENCH: WATER GRID

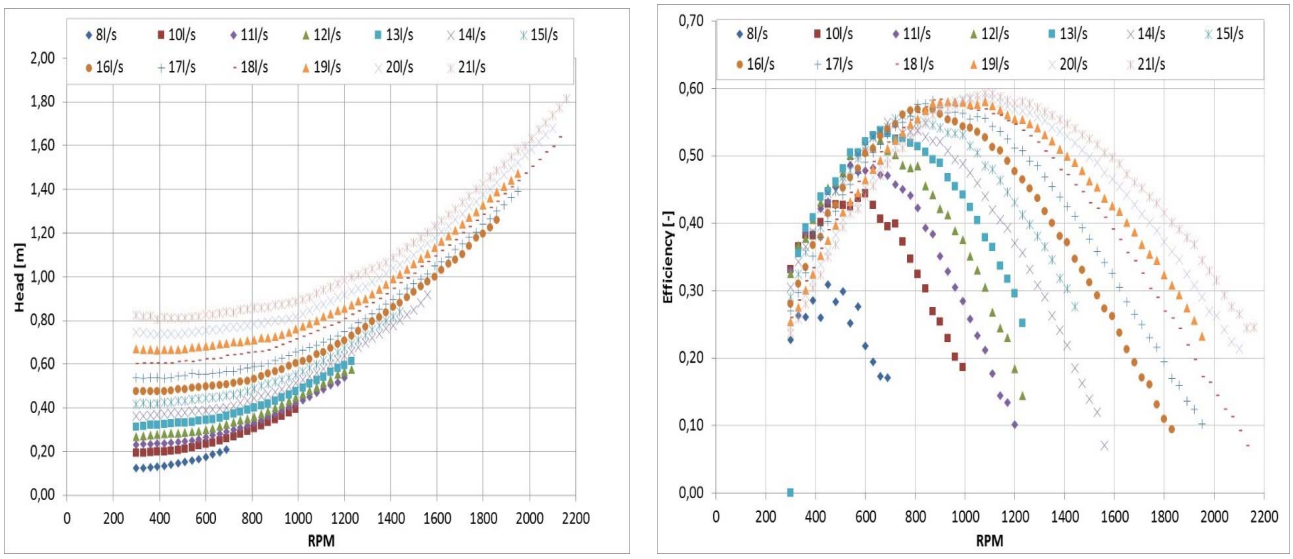

FIGURE 2.94: EXPERIMENTAL RESULTS

In figure 2.95 the whole validation of the simulation model is shown: it shows that the model reproduces the experimental data well with very small differences between the experimental and the model results for all the running conditions that were

analyzed.

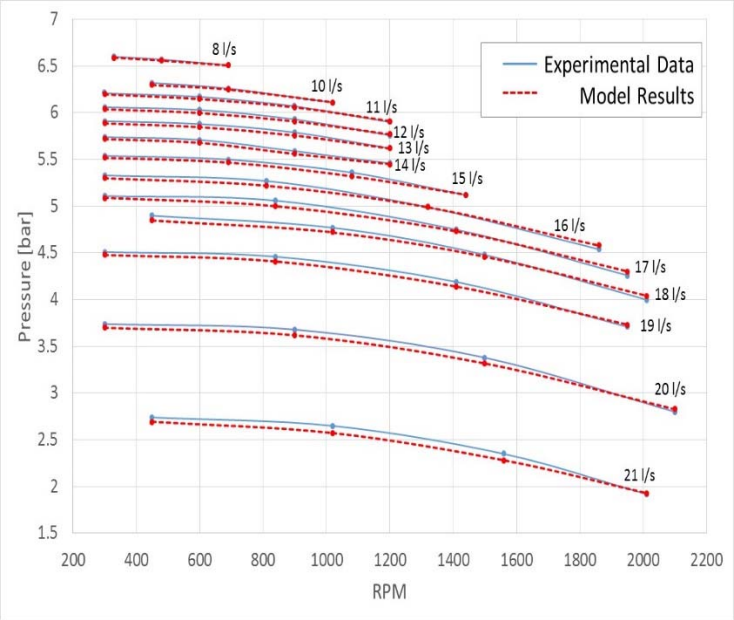

FIGURE 2.95: MODEL VALIDATION

After the validation phase in pump and turbine mode, simulation models have been used to predict the efficiency curves of the three analyzed pumps. Then, all the simulations have been performed to obtain the data necessary to evaluate the inverse characteristics. In the following, specific head, specific capacity, specific power and efficiency are defined as:

$$\psi = \frac{gH}{n^2 D^2} \quad \text{Specific head} \quad (2.29)$$

$$\varphi = \frac{Q}{nD^3} \quad \text{Specific capacity} \quad (2.30)$$

$$\pi = \frac{P}{\rho n^3 D^5} \quad \text{Specific power} \quad (2.31)$$

$$\eta = \frac{P}{\rho Q H} \quad \text{Efficiency} \quad (2.32)$$

where H [m], Q [m^3/s], and P [W] are the head, flow rate and power, respectively. The rotational speed is n [RPS] and D [m] is the impeller diameter. In the reverse mode simulation, the boundary conditions in pump and PAT mode were the same (declared data in pump mode). The boundary conditions in reverse mode are summarized in table 2.4.

BOUNDARY CONDITIONS	PUMP 1	PUMP 2	PUMP 3
Outlet pressure	1.9 bar	1.9 bar	1.9 bar
Inlet Volumetric Flow	90 ÷ 210 m^3/h	30 ÷ 85 m^3/h	48 ÷ 90 m^3/h
T_{in}	293.15 °K	293.15 °K	293.15 °K
P_{sat}	2886 Pa	2886 Pa	2886 Pa

TABLE 2.4: BOUNDARY CONDITIONS

The specific head, the specific power and the efficiency have been evaluated for both pump and turbine mode and for all the studied pumps. These are plotted versus specific capacity in figure 2.96.

It is clear that at high capacity the specific head in reverse mode is always higher than in direct mode. In reverse mode, pumps have a larger power range than in direct mode. The trends are quite different and the curves arising at low flow rate and at higher capacities have a higher power value than in direct mode. In pump mode, the efficiency has a typical “bell shape” while in PAT mode its profile resembles that of a Francis turbine: it increases at low flow rates and reaches a maximum value at high flow rates.

Moreover, the pump with the low specific speed works with low flow rates but high heads in direct mode. In reverse mode at high flow rates, the head is higher than the direct-mode value.

The pump with the high specific speed works at high flow rates but low heads. In reverse mode, working with the same flow rates, the maximum head is also higher than the direct-mode value.

For all pumps, the maximum value is lower than the direct-mode value. For low – specific speed pumps, this maximum value is approximately equal to the direct - mode value, while for high – specific speed pumps, it is lower.

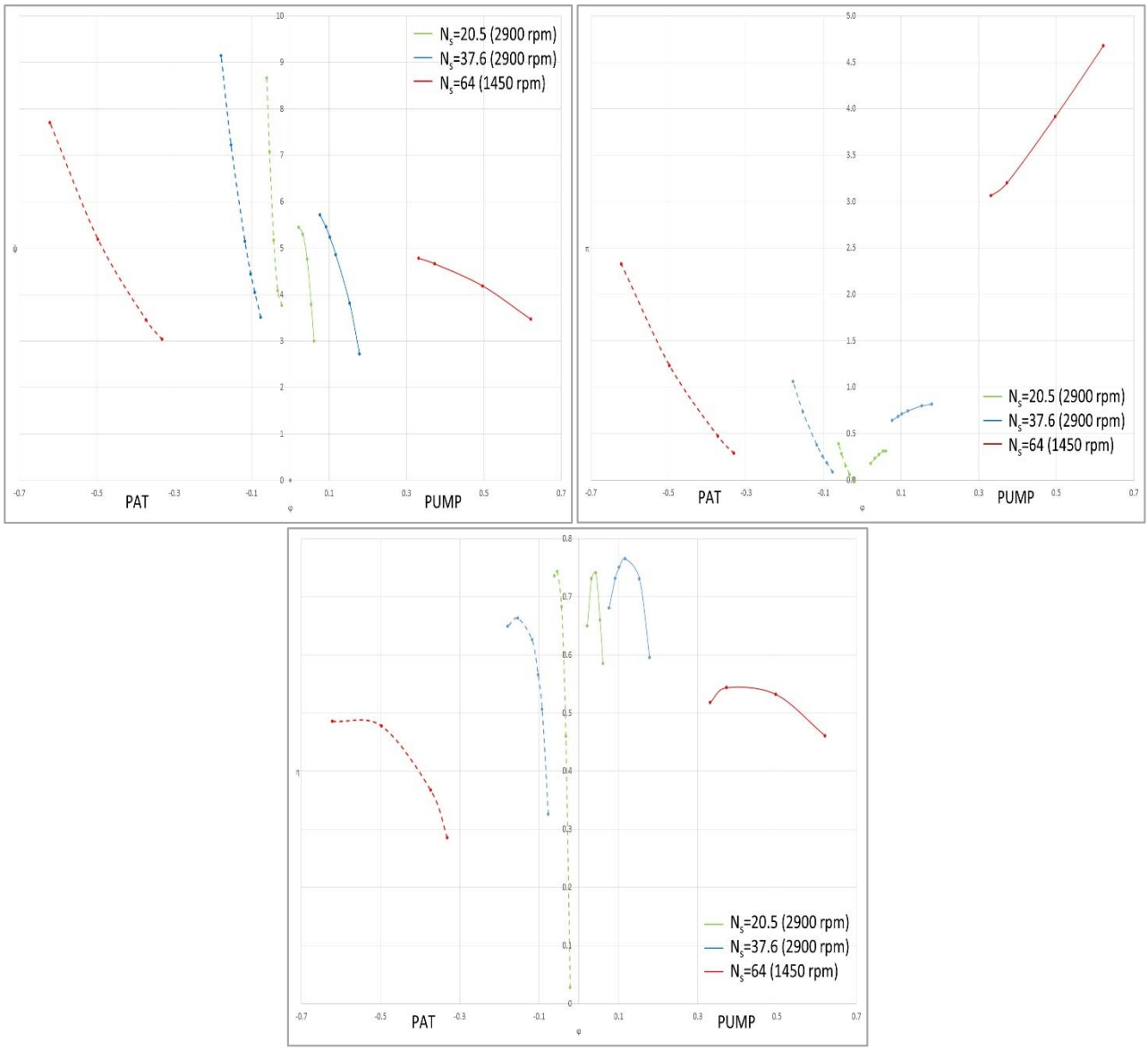

FIGURE 2.96: SPECIFIC HEAD, SPECIFIC POWER AND EFFICIENCY

In conclusion, in table 2.5, the BEP values are summarized:

BOUNDARY CONDITIONS	PUMP 1		PUMP 2		PUMP 3	
	Direct mode	Reverse mode	Direct mode	Reverse mode	Direct mode	Reverse mode
Head [m]	39	61	45.4	67	3.9	4.6
Capacity [m^3/s]	0.041	0.05	0.017	0.021	0.015	0.022
Power [kW]	20.5	19.98	10.01	10.24	1.05	0.75
Efficiency	0.787	0.663	0.743	0.741	0.543	0.487

TABLE 2.5: BOUNDARY CONDITIONS

2.5.4 Comparison of Prediction Methods

After the evaluation of the inverse characteristics, the results of the proposed methodology have been compared to the prediction methods available in literature. To this end, all the previously discussed methods have been applied to the three analyzed pumps. Some methods predict only the head and flow rate, while others also predict power and efficiency. In table 2.6, all the results are shown for pump 1.

METHODS	H [M]	Q [M^3/S]	P [KW]	H
Model results	**61.42**	**0.05**	**19.98**	**0.663**
Stepanoff	49.55	0.0463	22.5	0.787
Alatorre-Frenk	42.79	0.091	28.92	0.757
Sharma	51.99	0.0498	20.5	0.807
Schmiedl	43.94	0.0514	16.82	0.759
Grover	78.59	0.0657	36.92	0.729
Hergt	41.90	0.0508	-	-
Childs	49.55	0.0522	19.96	0.787
D&N	58.56	0.0411	18.17	0.769

TABLE 2.6: COMPARISON FOR PUMP 1

The flow rates calculated using the methods of Sharma and of Hergt and Schmiedl are very close to those of the proposed CFD methodology. Grover's and Alatorre-Frenk's methods overestimate this value while the other methods underestimated the value by a margin of 10-15%. All methods underestimate the head value except for Grover's. These values diverge with errors of up to 30%.

Evaluating the percentage deviation as:

$$percentage\ deviation = \frac{predicted\ value - cfd\ value}{cfd\ value} \cdot 100 \qquad (2.33)$$

In figure 2.97 the deviations between the predictions of these methods and the simulated data are plotted vs. the pump specific speeds for all three pumps.

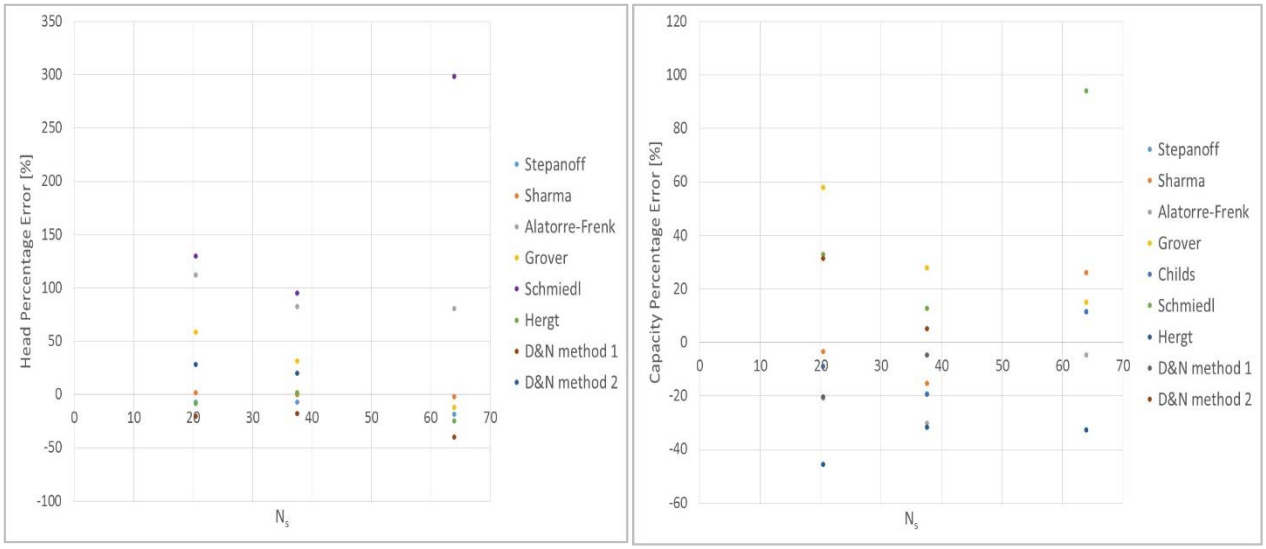

FIGURE 2.97: PREDICTION METHODS COMPARISON

It easy to observe that in some cases the deviation is very high.

To evaluate the Derakhshan and Nourbakhsh efficiency [24], the CFD model results were used as shown in figure 2.98. In this figure, the relative velocity magnitude [m/s] is shown and the angle between the relative and absolute velocity is highlighted in red, at BEP conditions and in pump mode.

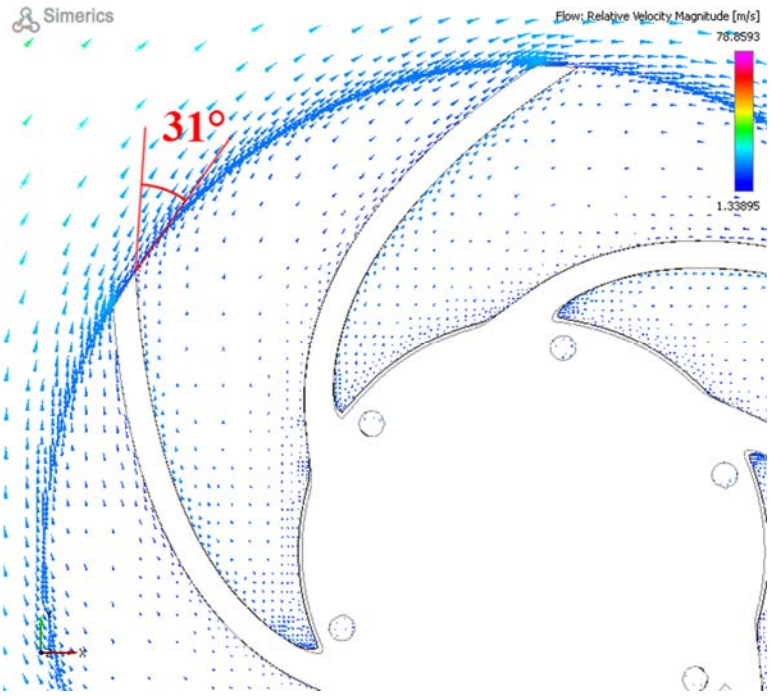

FIGURE 2.98: RELATIVE VELOCITY MAGNITUDE

2.5.5 Conclusions

A methodology to predict the inverse characteristic of a centrifugal pump has been presented. This methodology is based on the results of a three-dimensional simulation model build with the technique proposed in this PhD Thesis. Three industrial pumps have been analyzed, with different specific speeds. First, the simulation models have been validated with data supplied by the pump manufacturers. Then the results of an experimental campaign have been used to validate a model simulating the pump working in reverse conditions.

Starting from the CFD model results, the specific head, capacity, power and efficiency have been evaluated and the best efficient point of all the analyzed pumps was found. Furthermore, several prediction methods have been applied to the tested pumps and their predicted values were compared with those of the proposed methodology. Some methods (e.g., Childs' method) are not in accord while others (e.g., Stepanoff's method) show small relative differences.

2.6 Directional Spool Valve

2.6.1 Introduction

In this paragraph, the three-dimensional computational fluid dynamics (CFD) methodology proposed has been applied for the study of directional spool valves. In recent years, many studies were initiated to improve proportional valve performance [41 - 61]. However, the scientific understanding of how such valves operate is limited because of the lack of three-dimensional computations fluid dynamics capability, especially the lack of computational codes intended for these applications. As pointed out by Amirante et al. [41, 43, 45, 47], the preliminary estimation of the fluid flow-rate and the flow forces is crucial for the design of hydraulic valves.

An important research study was made by Noah D. Manring [62, 63] modeling a spool-valve to study the flow forces, the same author in another scientific paper well showed the experimentally investigation made on an hydraulic spool valve to measure the pressure transient force action on the valve's spool. Both papers demonstrated the importance of the fluid-dynamic forces' study by testing and modeling approaches. All the mentioned research activities were mainly focused on the study of the flow force while no studies regarding the spool spin effect and induced fluid torque are available. Thus, the study was focused on the analysis of the influence of the internal geometry on the spool spin effect.

Using a computational fluid dynamics (CFD) technique with an accurate turbulence model, it is possible to improve the valves' internal geometry to reduce the internal flow vorticity [59].

The proportional valve is designed in compliance with ISO4401-05 (CETOP 05) standard to be mainly applied in industrial fields. For this valve, the internal spool is stroked into the valve body by means of two opposed proportional solenoids, with electrical currents that are modulated by the embedded electronic device mounted on the top of the valve. Two springs on the side mechanically define the spool neutral position. A LVDT sensor provides position feedback to the electronic device to

perform closed loop position control, to improve valve stability with working condition changes, reduce hysteresis, increase repeatability and improve dynamic behavior. This type of valve is mainly used to control the speed and direction of hydraulic actuators, especially when high dynamic performance is required.

The main purpose of the embedded electronics in the spool is to control the spool position despite changes in working conditions. A low sensitivity to external perturbations is required especially under highly dynamics conditions, to achieve robust performance. Thus, it is desirable that the forces, especially the hydrodynamic ones, would have a small effect on the spool. To achieve this goal, the Hydraulic Research Group of University of Naples "Federico II" and the Center for Compact and Efficient Fluid Power the University of Minnesota developed this study. A novel feature of this study is that it focuses on spool torque at high oil flow rate, also analyzing the internal fluid dynamic behavior of the oil throughout the spool valve.

Starting from a baseline spool and core case, the geometry has been modeled and analyzed using a CFD software. The models were validated using experimental data measured in the hydraulic laboratory of the University of Naples. A dedicated test bench was realized for this application: the adopted layout is an innovative solution and represents an innovative configuration to measure the spool torque. Test and simulation are steady state; the spool was fixed at the maximum opening position where the fluid-dynamic forces are highest and the torque is maximum [64]. Even if in this application the optimization was been sufficient for the worst condition (maximum opening) this methodology can be applied in other analyses i.e. in transient conditions, studying of the internal fluid dynamic effects by changing the spool position [65 – 68]. Three different core designs were tested to compare and prove the effectiveness of this approach.

2.6.2 Three - Dimensional CFD Model

The mathematical model was performed with the commercial CFD code PumpLinx® (developed by Simerics Inc.®). From the proportional spool valve 3D

geometry, the fluid volume has been extracted. The extracted volume is shown in figure 2.99. In this figure the entire internal valve fluid volume is shown.

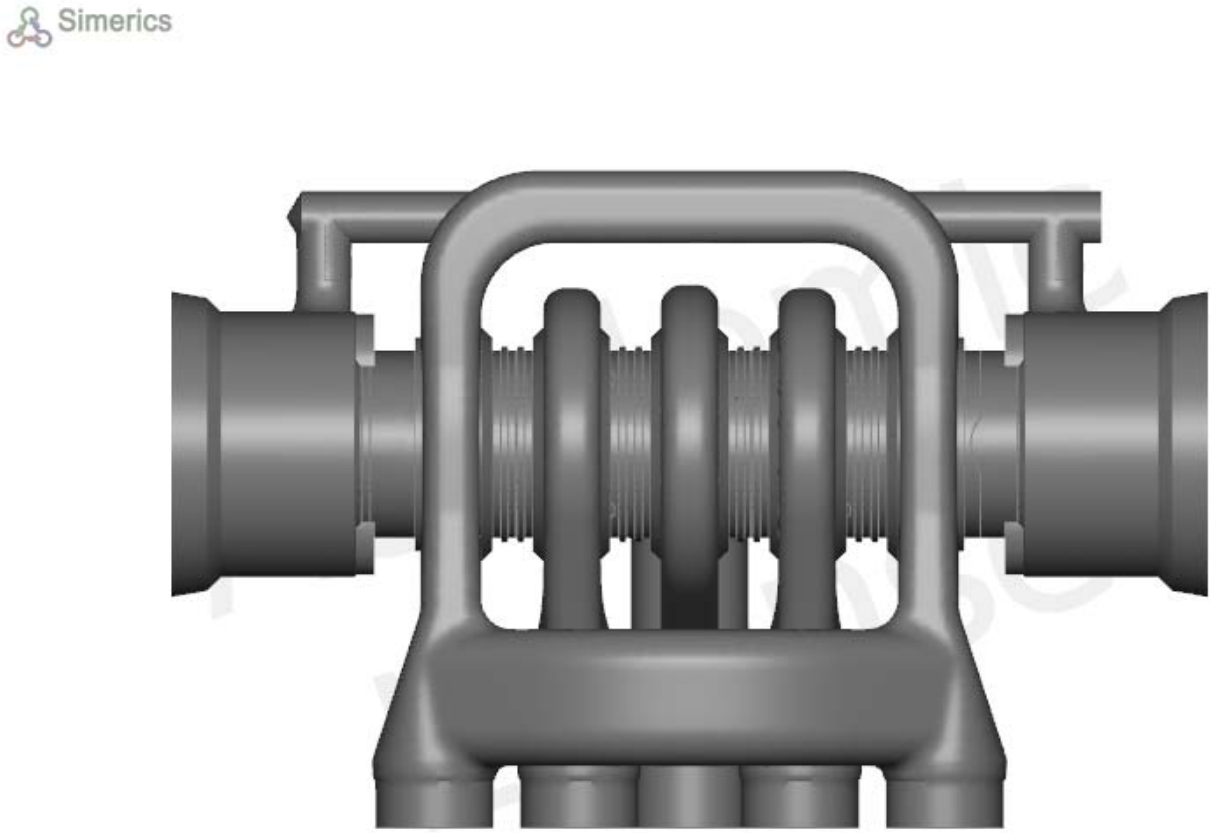

FIGURE 2.99: PROPORTIONAL SPOOL VALVE FLUID VOLUME

A mesh sensitivity analysis is normally a good practice for any new problem to be studied with a CFD solver. In this specific case the mesh size of around half a million cells allows for excellent accuracy (in comparison with experimental tests) and for computational efficiency.

However, a grid-independence analysis was made on the model. Three different models have been studied:

- A model with 200000 cells mesh
- A model with 500,000 cells mesh,
- A model with 1,000,000 cells mesh.

Results of this analysis are showed in figure 2.100. In the graph, the torque on the spool [Nm] in function of the flow - rate [l/min] is presented. All the data are compared with experimental data obtained on the analyzed valve.

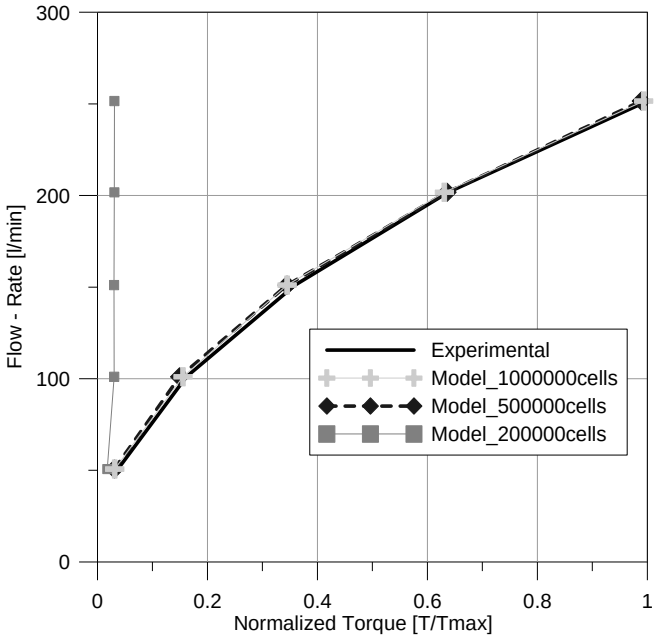

FIGURE 2.100: GRID ANALYSIS

Figure 2.100 shows that by changing the mesh size, code's results significantly vary. Important differences are visible comparing the experimental data with the results of the model with 200,000 cells.

Model results in figure 2.100 underline that there are no appreciable difference between the model with 500,000 cells and the model with 1,000,000 cells. Both models present the same percentage differences with the experimental data. For this reason, the presented model has 500,000 cells.

Figure 2.101a shows the binary tree mesh in a section plane of the considered proportional spool valve.

The model of the proportional spool valve consists of about 550,000 cells mesh as shown in figures 2.101a, 2.101b and 2.101c. In particular, figure 2.101a shows the grid in a valve cross section, for this figure it is clear the different grid adopted for each valve's part; the spool grid density is more high than the valve's core because this area is more important for the present analysis. Figures 2.101b and 2.101c while, show the grid of the entire body and the particular of spool's grid. The sensitivity analysis on the mesh to find the best practice is not explained. This analysis was made by the author in order to validate the 3D CFD model with a comparison between the experimental

data, made on the first prototype, and the model results. Find the best practice mesh, it was used for all the other models confirming in each case the accuracy of the solution.

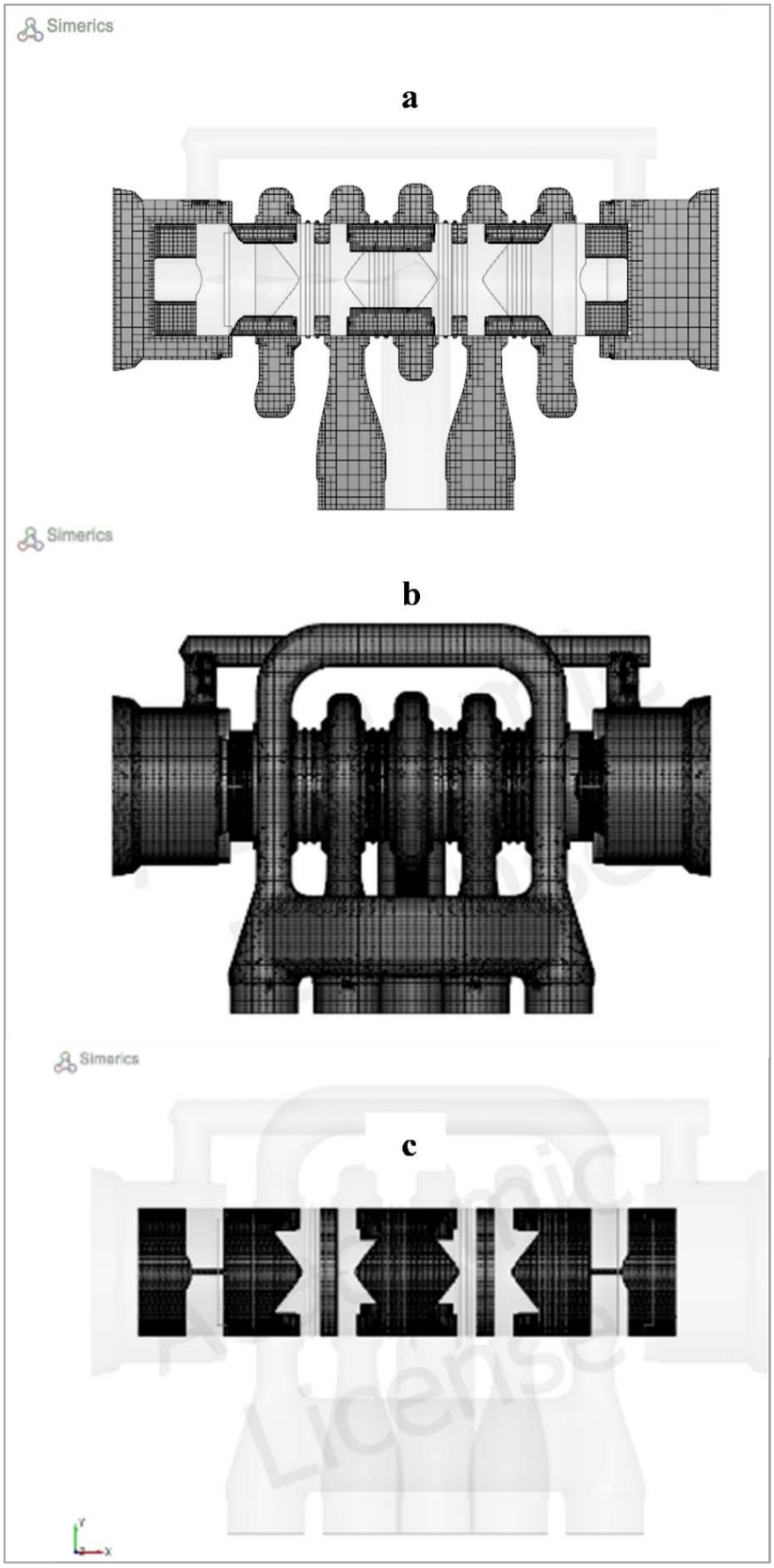

FIGURE 2.101: BINARY TREE MESH FOR THE PROPORTIONAL SPOOL VALVE CROSS SECTION

Turbulence models for computing effective liquid viscosities are important at high Reynolds numbers.

Results will be shown at the maximum displacement of the spool, which obviously consist on the higher high flow rate condition.

The boundary conditions were the same for the model and the experimental tests. In particular it was analyzed a flow rate range between 50 and 250 l/min at an oil temperature of 40 °C.

In figure 2.102, as an example, the pressure distribution in one valve fluid volume is shown, at 70 bar inlet pressure.

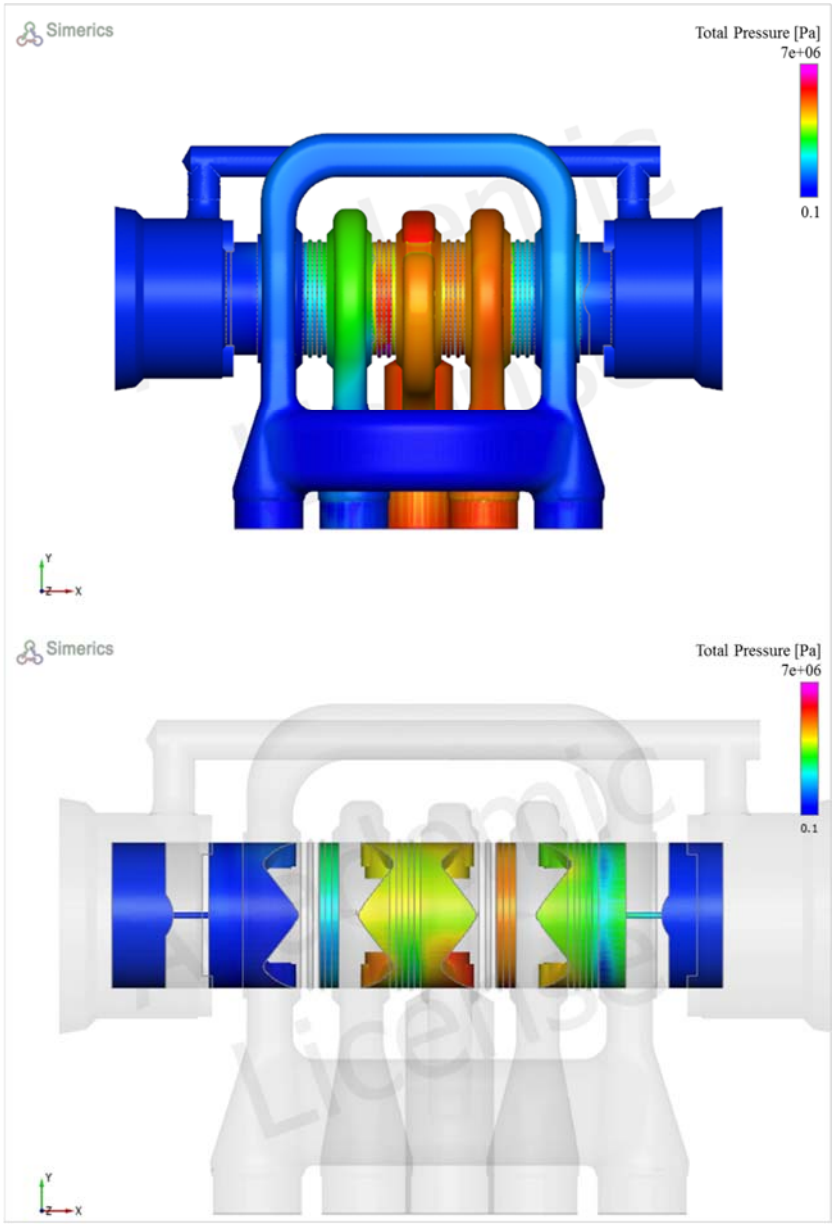

FIGURE 2.102: PRESSURE DISTRIBUTION IN THE FLUID VOLUME

2.6.3 Experimental Data and Model Validation

A preliminary hydraulic model validation was performed by the researchers of the University of Naples "Federico II" on a hydraulic test bench to determine the valve pressure drop characteristic [61, 69, 70]. The test bed layout is shown in figure 2.103 where a relief valve (1), two pressure transducers (2), the tested valve (3) flow-rate transducer (4), and lamination valve (5) are indicated. The test bench layout is an innovative configuration to measure the torque of the valve's spool. The bench design was completely study by the engineers of both universities.

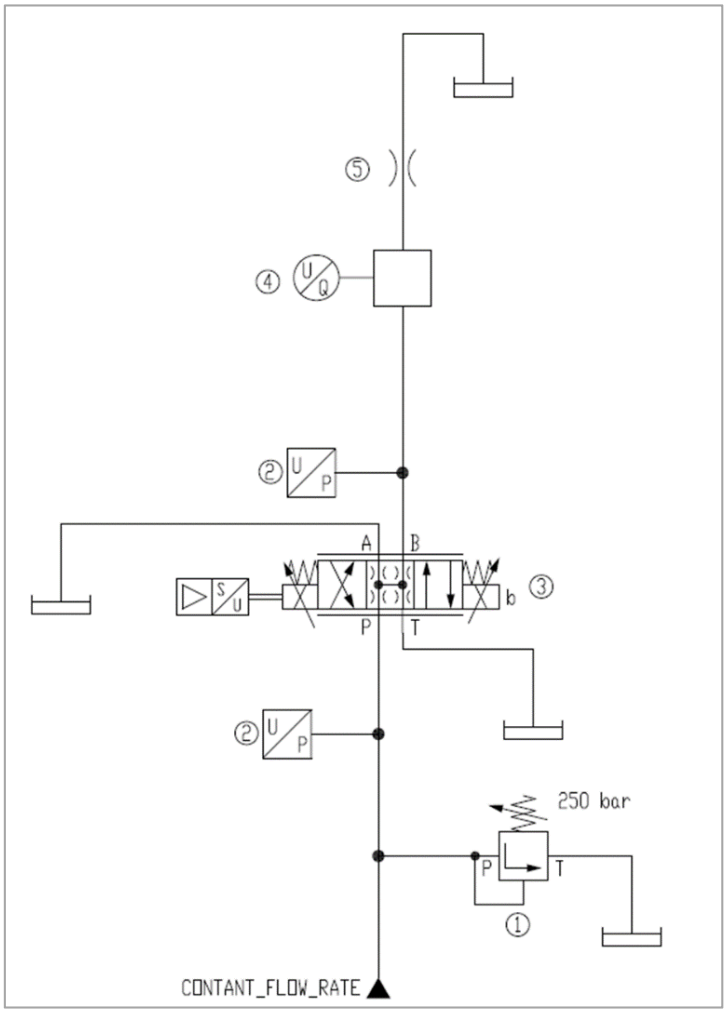

FIGURE 2.103: TEST BENCH HYDRAULIC SCHEMATIC

The flow rate transducer (VS10GPO12V manufactured by VSE.flow®) characteristics are shown in table 2.7, the pressure transducer (type HDA 4400, manufactured by Hydac®) characteristics are shown in table 2.8 and the torque meter

(type 4503A manufactured by Kistler®) characteristics are shown in table 2.9. The transducers output signals were acquired and processed using a National Instruments® system (DAQ Card TM - 6062E). A constant temperature of 40°C and Mobil DTETM 25 (ISO VG 46) hydraulic oil was used in all tests.

The flow rate transducer – VS10GPO12V - VSE.FLOW®	
Max flow-rate [l/min]	525
Accuracy	>0.3% of the measurement value
Repetition accuracy	± 0.05% under the same operating conditions
Max. operating pressure	420bar

TABLE 2.7: FLOW RATE TRANSDUCER CHARACTERISTICS

The pressure transducer - HDA 4400 - Hydac®	
Range	0 – 400bar
Accuracy	±0.5%. FS
Hysteresis	0.4% FS
Repeatability	0.1% FS
Operating temperature range	-25 +85°C

TABLE 2.8: PRESSURE TRANSDUCERS CHARACTERISTICS

The torque meter transducer – 4503A - Kistler®	
Range	0 – 2Nm
Max speed	12000rpm
Accuracy class	0.2
Linearity error	0.2 [%FSO]

TABLE 2.9: TORQUE METER TRANSDUCER CHARACTERISTICS

The tests were performed in steady state, with different oil flow rates and with constant lamination valve position. The spool was fixed in its maximum opening position where the forces are highest. A special steel manifold was constructed, with a ground plane, to obtain the correct alignment between the spool and torque meter axes (figure 2.104). In this figure, it is shown that the measuring side of the torque meter is coupled to the valve spool, while the other side is fixed to the manifold. All the tests were made at the maximum spool opening position with different oil flow rate conditions [72].

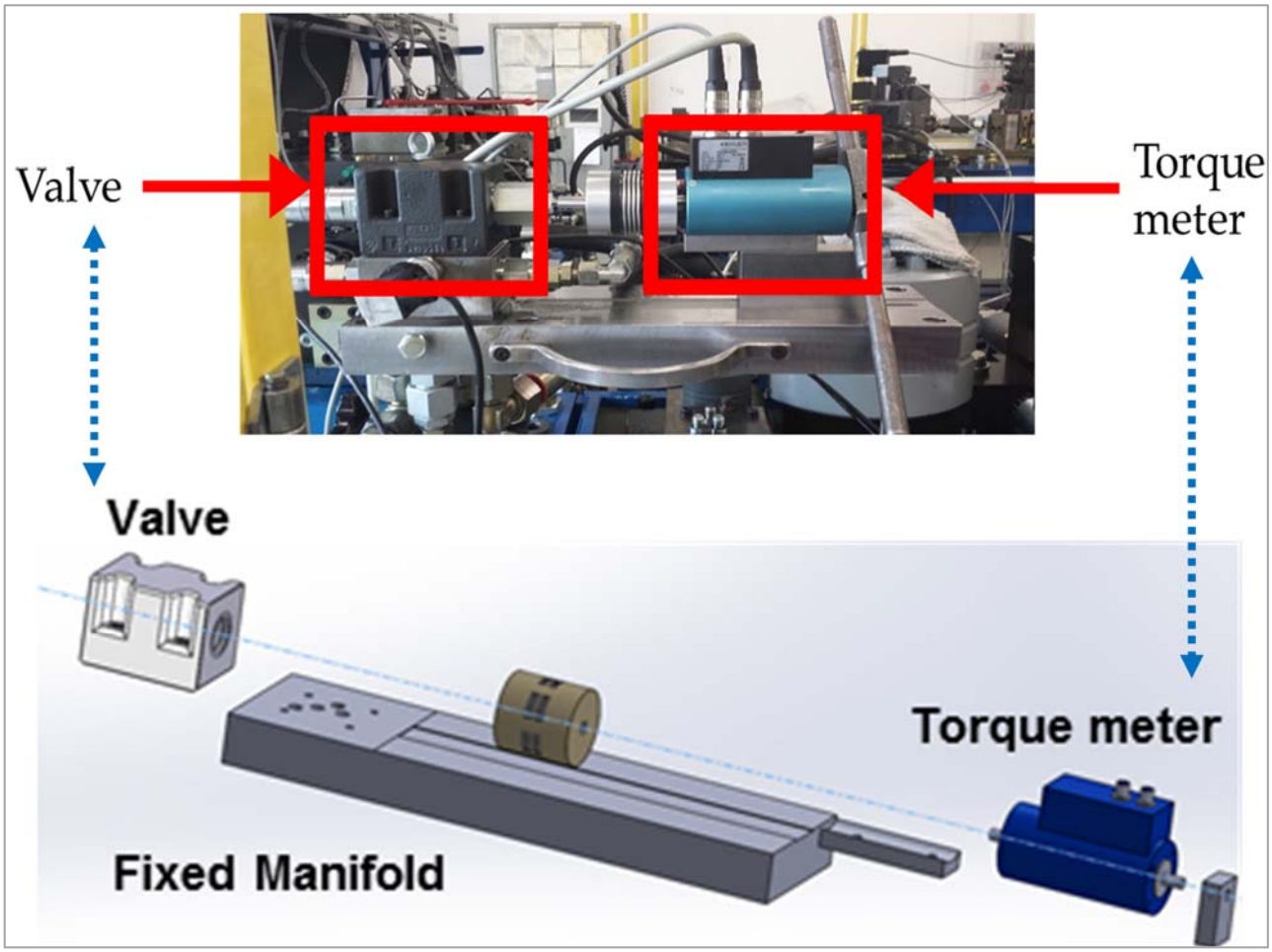

FIGURE 2.104: TESTED PROPORTIONAL SPOOL VALVE

All the experimental tests were carried out, connecting the port P to port B while ports A and T were at atmospheric pressure as shown in the hydraulic schematic of the tests bench (figure 2.103). In figure 2.105, oil pressure versus flow rate is shown.

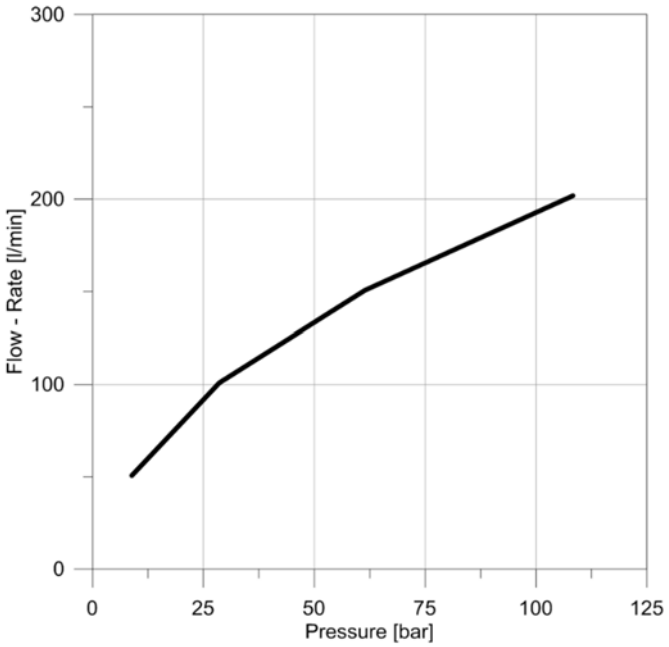

FIGURE 2.105: FLOW RATE VERSUS PRESSURE

Using the experimental data, the valve model was validated comparing the experimental data with the model results. The model validation consists in a comparison between the torque measured and modelled value (see figure 2.106). The torque in figure 2.106 is normalized on the maximum value.

As shown in figure 2.106 the toque value, as expected, increases with the flow-rate from 50l/min to 200l/min.

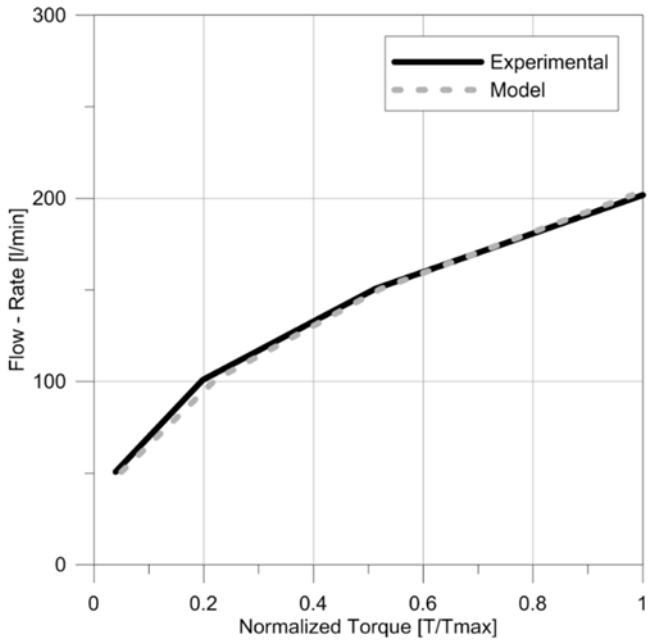

FIGURE 2.106: COMPARISON OF MODEL AND EXPERIMENTAL RESULTS

The boundary conditions in the model were the same as the experiments. These includes the oil flow rate at port P, pressure at port B, atmospheric pressure at ports A and T, and an oil temperature of 40 °C. In figure 2.106 the numerical model results is the dashed line, while the experiments is the continuous line.

The trend confirms the accuracy of the proportional spool valve model. The error is less than 2% in all of the examined conditions.

Starting from the described CFD valve model, many studies were made to reduce, as possible, the torque on the spool. This value is always over zero for all the flow - rate conditions. The results of this study are shown in the following paragraphs where using the three-dimensional CFD technique a new valve body was designed. The new valve core has a torque on the spool near zero in all the flow - rate conditions.

2.6.4 Model Application

Simulation results were deeply analyzed to investigate on the effect of the fluid turbulence on the valve. All the observations are results of the fluid internal vorticity study that is possible to make well especially by using the presented modelling approach. As already said, the goal is the reduction of the torque value on the valve' spool for all the operating conditions by an optimization of the internal fluid-dynamic.

The following figures will better describe the criteria adopted to achieve the study goal. All figures relate at the first valve geometry, each port will be well described to analyze the fluid vorticity, velocity, and pressure in each port a cross section [73].

The analysis consists in an accurate study made on each port of the valve core geometry, only the results in port P and B will be shown, because as already said test and simulation port A and T were at 1 bar. As is possible to see comparing figures 2.107 and 2.108 with figures 2.109 and 2.110, it is clear that the main contribution to the spool torque comes from stresses generated in port P, where the pressure drop and the fluid velocity are largest (as shown in figures 2.107 and 2.08). An analysis of the oil pressure distribution and oil velocity distribution in ports P and B will be compared

to show how the methodology is used to analyze the torque phenomena on the spool. The results have been evaluated for the following valve operating conditions:

- Oil flow - rate at port P is 200 l/min,
- Pressure at port B is 108 bar,
- Atmospheric pressure at ports A and T,
- Oil temperature is 40 °C.

In the next four figures (figures 2.107 – 2.110), several 3D model results for ports P and B are reported, these results are the only way that can be used to study this particular torque phenomena. Only by the investigation of the internal flow distribution it is possible to reduce issues present on this valve. This methodology, in fact, permits one to visualize the pressure and flow in all conditions. The first model result is presented in figure 2.107 where the pressure distribution inside port P is shown. The pressure reaches, as expected, its maximum in the suction area and decreases inside the fluid volume. in fact, there are a no uniform pressure distribution in the spool fluid volume. This volume has a high pressure in the bottom left area and a low pressure (yellow area) on the top right corner. This not uniform distribution will has an important weigh on the torque value.

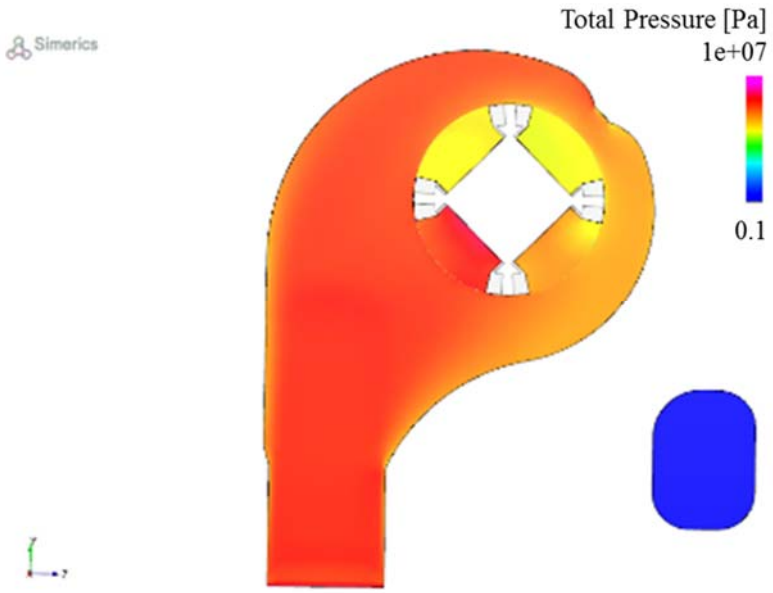

FIGURE 2.107: PRESSURE DISTRIBUTION INSIDE PORT P

The results showed in figure 2.107 are confirmed in figure 2.108 where the flow streamlines, color coded by mean flow velocity (m/s), in valve port P, are presented. Showing the streamlines can help analyze the critical zones where vortices are located. The flow conditions inside this port cause spool rotation. Analyzing results in figures 2.107 and 2.108 it is possible to understand that the low pressure areas correspond to the high flux velocity areas while the high pressure areas correspond to the low flux velocity. Comparing both results, it is clear that the critical areas in figure 2.108 are the low pressure zones in figure 2.107.

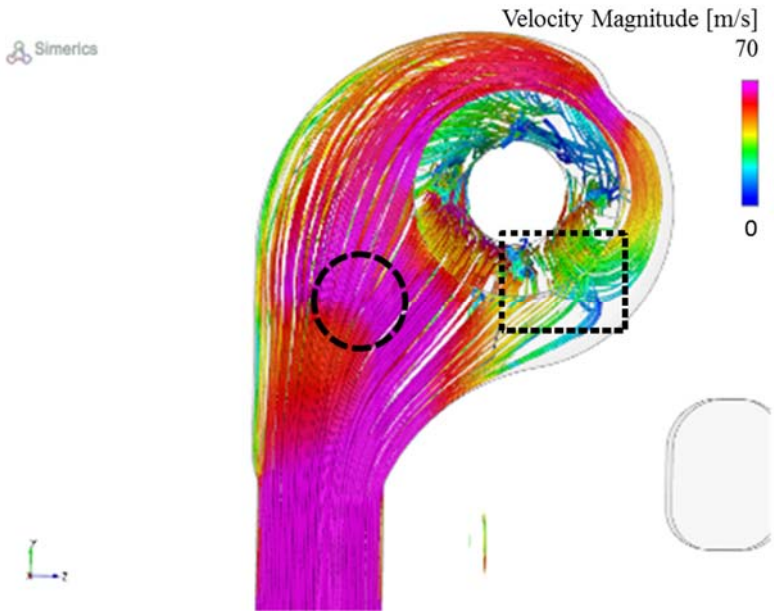

FIGURE 2.108: TYPICAL STREAMLINES INSIDE PORT P

In figure 2.108, two critical areas are underlined. The first one, dash circle, is critical because the flux has a high velocity (magenta color correspond at the highest value of the scale). The fluid conserves a high velocity on the top area around the spool while decrease on the bottom spool side. The fluid no symmetry velocity in this port is cause of the high torque on the spool. The second critical area is underlined with a dash rectangle. As shown, in this area the fluid has a high vorticosity, the target of this study is also a reduction of vortexes in this area.

The following figures (figures 2.109 – 2.110) show pressure distribution and streamlines inside port B. Analyzing the pressure distribution in figure 2.109 it can be

noted that the pressure inside port B is almost axisymmetric; therefore its contribution to the spool torque is less than port P. This is even more evident in figure 2.110 where the streamlines trend confirms the lack of influence of port B internal fluid flow on the spool torque.

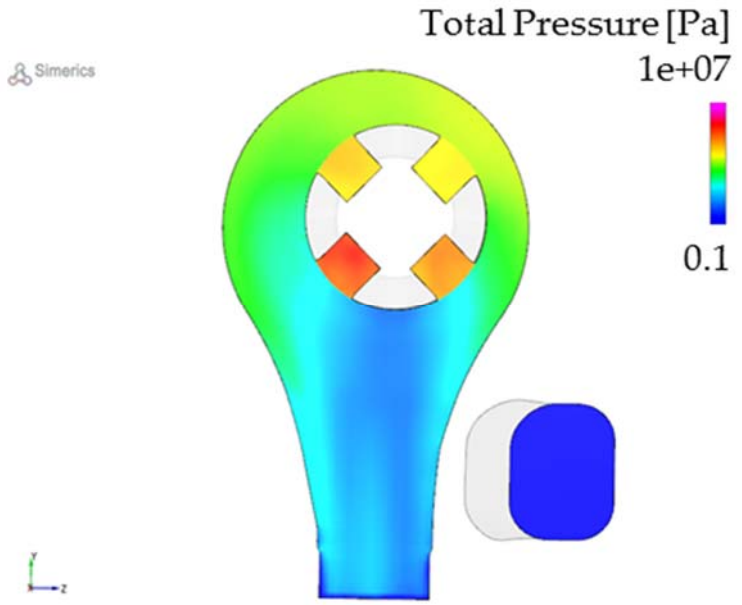

FIGURE 2.109: PRESSURE DISTRIBUTION INSIDE PORT B

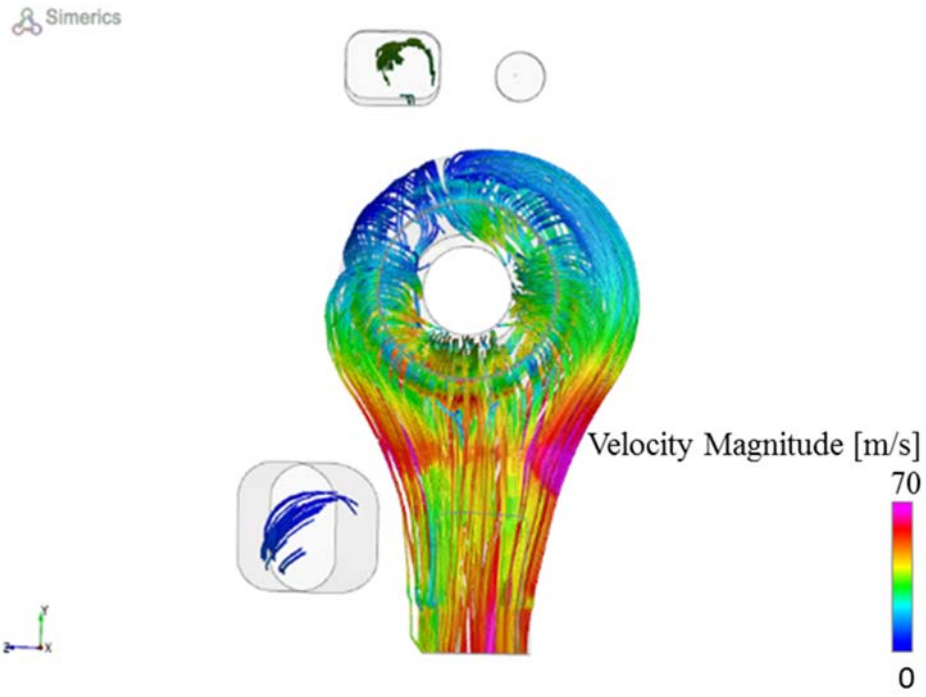

FIGURE 2.110: TYPICAL STREAMLINES INSIDE PORT B

The presented results on each valve ports has clarified that the torque phenomena on the spool depend by the non-symmetry of the flow inside the port P. This deduction represents an important result for this study because with the 3D visualization it has been possible to find the issues in the fluid-dynamic.

Starting from the considerations made in this paragraph with the same approach the component was redesigned to achieve the zero torque target for this analysis eliminating the flux anomalies. In the next paragraph results of the new valve designs will be presented.

2.6.5 New Valve Design

This paragraph will show the steps carried out to approach the problem. This sequent of analysis can be adopted to solve similar problems in other application then on others hydraulic components.

Starting from the considerations made in the previous paragraph, the strategy adopted to achieve the target passes thought the redesign of valve' the internal fluid-dynamic of a proportional spool valve to achieve the reduction of the torque on the spool. The results of simulations carried out on the proportional spool valve will now be shown where the internal geometry of Port P is varied to reduce spool torque. The strategy adopted is based on the analysis of the fluid shown in figure 2.108, the high acceleration in the first area must be reduced by changing the depth of the port allowing the fluid to enter Opinions more slowly without affecting the performance of the valve.

Starting from the base case "Case 1" other three new solution obtained by changing the depth of port P will be presented. The study made using the 3D CFD approach underlines the influence of the depth of port P the inlet dot, therefore for each case the depth of the port P was reduced.

As already said, the goal of this activity is the reduction of the vorticity magnitude close to the spool (see the black circle and the rectangle in figure 2.108). Starting from the base configuration, we analyzed different valve geometries shown in figure 2.111, where Case 1 is the base proportional body valve geometry. In Cases 2, 3 and 4, the port P' depth is reduced by 13%, 17% and 21%.

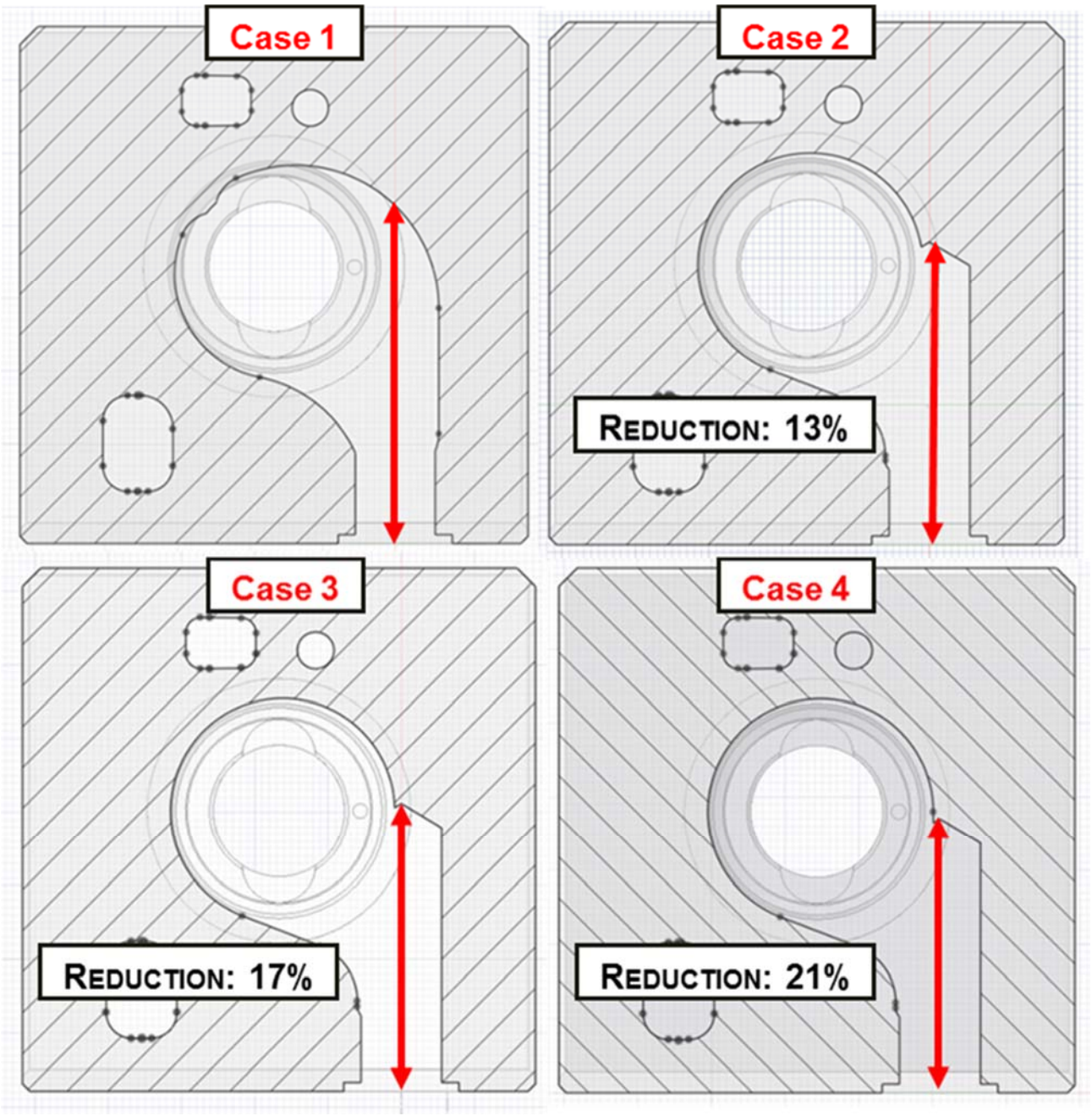

FIGURE 2.111: NEW PROPORTIONAL SPOOL VALVE DESIGN

The port P' depth reduction depend by the fact that, as shown in figure 2.108, the most critical area for the flux's no-symmetry is located in the zone underlined by a circle (figure 2.108) where the fluid has the highest velocity caused by the local low pressure (see figure 2.109). For this reason, in the presented study the three-dimensional CFD model results acting on the port P design will be shown.

The results of this analysis are shown in the following figures. As said, the target for this analysis is to achieve the value of zero torque on the spool for all the flow - rate

conditions, but a design could cause a valve's performance decreases in term of delivery flow - rate changing the pressure. New geometries give a drastically torque's reduction shown in figure 2.112 without any modifications for the valve performance as shown in figure 2.113 (pressure versus flow rate).

Figure 2.112 shows that the new valve's designs (Case 2, 3 and 4) have a torque drastically reduction from the Case 1. With a port P's depth reduction of 13% (Case 2) the torque value is always low than the Case 1 trend, the reduction is most clear comparing the Case 1 with the Case 3 and Case 4 results.

The Case 4, in particular, has a torque curve's trend always near zero (dash purple curve). Only this Case was prototyped and tested to verify the three-dimensional CFD model results.

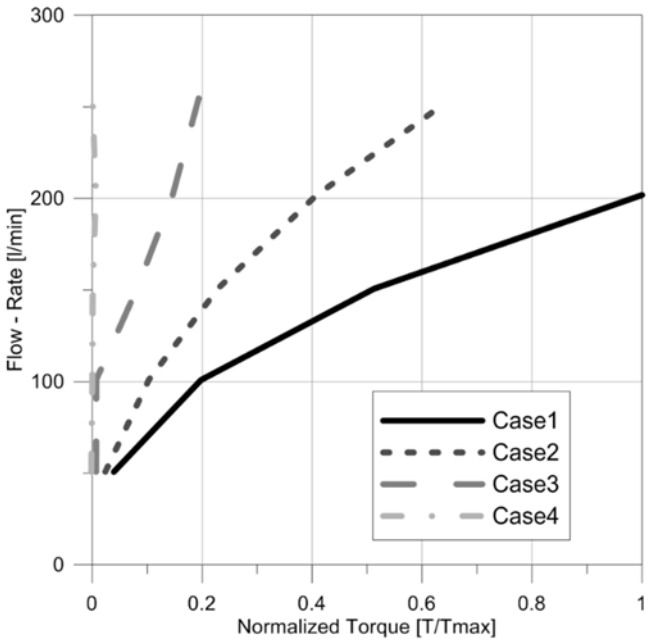

FIGURE 2.112: FLOW RATE VERSUS TORQUE

As said, as consequence of this study, the case 4 prototype was built and tested; new experiments were performed on the same hydraulic test bench in figure 2.103, which confirmed the accuracy of the simulation model and the reduced torque for Case 4. The results of the experimentation made on the prototype of the new valves design were showed in figures 2.114 and 2.115. Those graphs showed the good correlation between model results and experimental data.

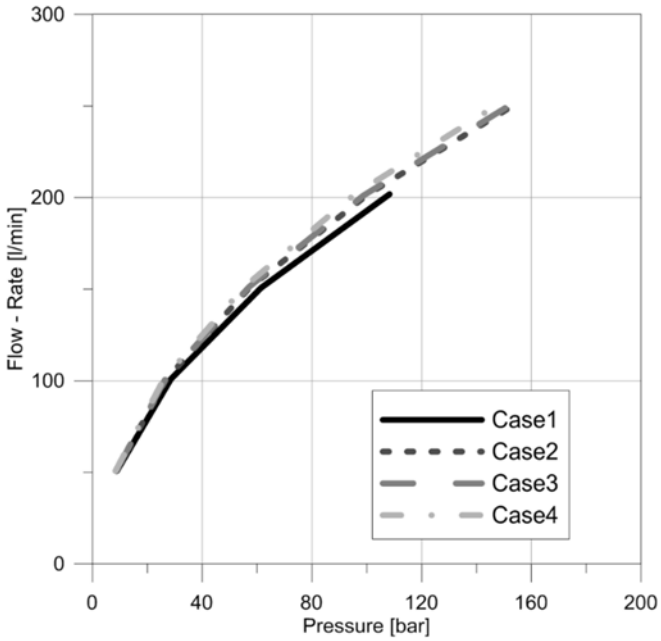

FIGURE 2.113: FLOW - RATE VERSUS PRESSURE

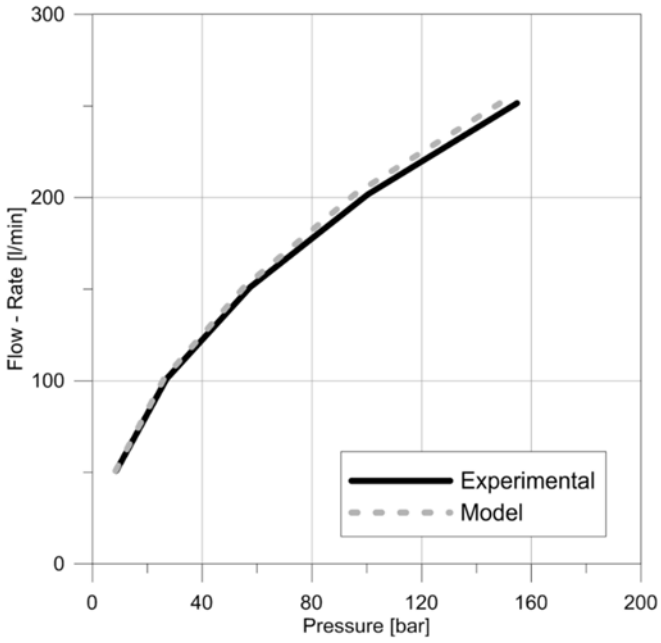

FIGURE 2.114: COMPARISON OF EXPERIMENTAL AND MODEL RESULTS FOR FLOW - RATE VERSUS PRESSURE

As demonstrate in figure 2.113 and then in figure 2.115, the Case 4's torque value is always close to zero. The new valve geometry has therefore centered the target set for this analysis of zero torque on the valve spool. As said, the main geometry modification on the valve body was the reduction of the port P's depth, the reduction from the Case 1 (starting case) and the Case 4 is of 21%.

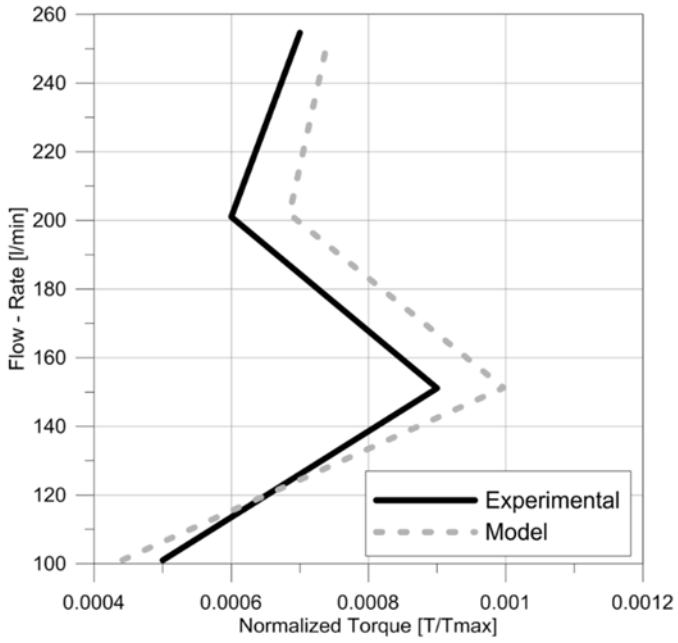

FIGURE 2.115: COMPARISON OF EXPERIMENTAL AND MODEL RESULTS FOR FLOW RATE VERSUS TORQUE

Those torque results was achieved studying the port P internal fluid-dynamic to reduce the no-symmetry of the flow - rate distribution inside this volume.

Figure 2.116 the fluid velocity distribution (streamlines) between the case 1 and case 4 is shown. In both critical areas, evidenced with rectangles and circles, the velocity decreases from Case 1 to Case 4; the fluid is symmetric thus reducing the spool torque. Therefore, results in figure 2.116 are consistent with the spool torque reduction shows in figures 2.113 and 2.115.

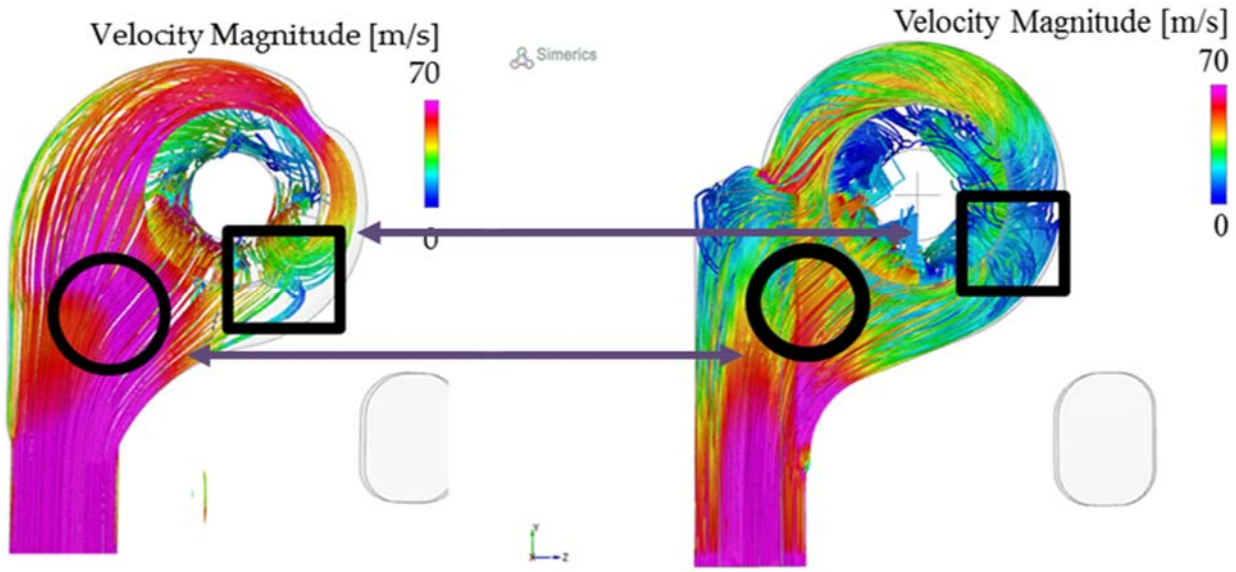

FIGURE 2.116: COMPARISON OF STREAMLINES FOR CASE 1 AND CASE 4

Figures 2.117 and 2.118 show the turbulent kinetic energy for Case 1 and Case 4. In figure 2.117a areas of high turbulence are clearly visible. These areas are mostly located in the zones near the spool generating high vorticity, recirculation and consequently a higher torque value. Figure 2.117b shows the corresponding velocity field. The highest turbulence areas are located where the velocity is high. Comparing the results in figures 2.117 and 2.118 is possible to see that the modified has much lower values of turbulence intensity verifying the improvement made on the valve's internal flow field with the modeling analysis.

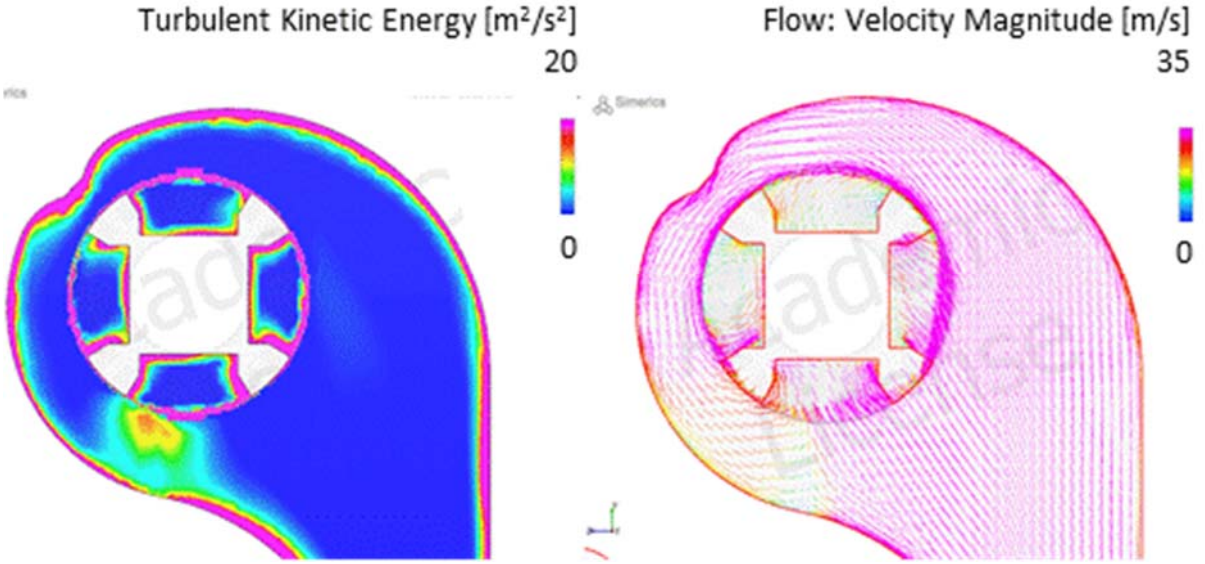

FIGURE 2.117: CASE 1: (A) TURBULENT KINETIC ENERGY AND (B) VELOCITY DISTRIBUTION

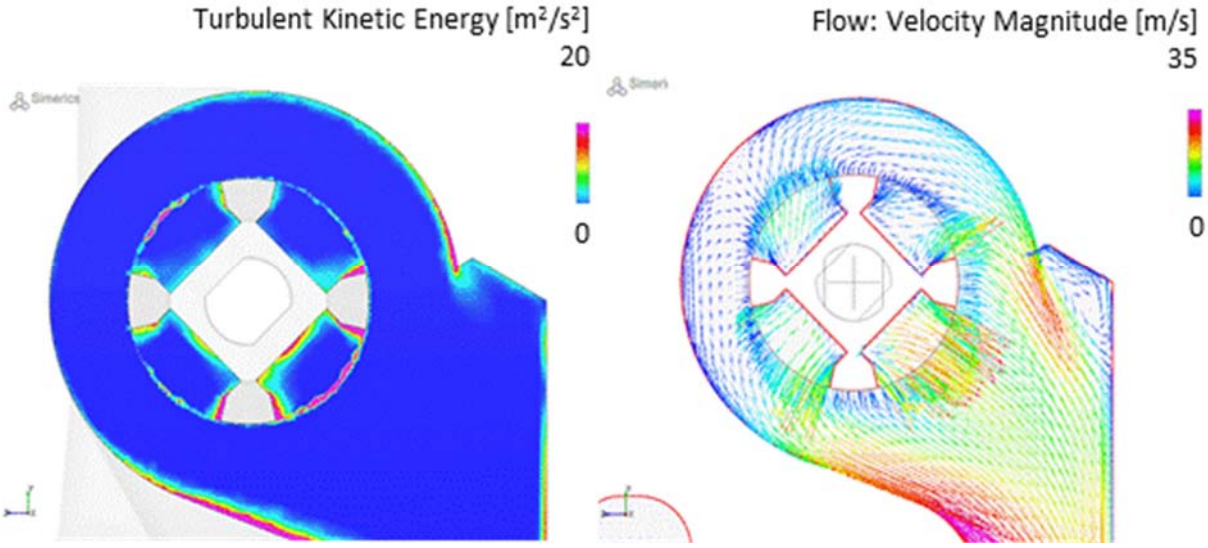

FIGURE 2.118: CASE 4: (A) TURBULENT KINETIC ENERGY AND (B) VELOCITY DISTRIBUTION

Graphs in figures 2.113 and 2.114 confirmed that the new internal fluid dynamic geometries have no effect on the valve performance as shown by pressure versus flow rate curves. This is confirmed by analyzing the pressure distribution inside the valve fluid volume as shown in figure 2.119. The pressure distribution is, for both cases, practically equal. The pressure is high in the port P suction area and then decreases as it approaches the spool fluid volume.

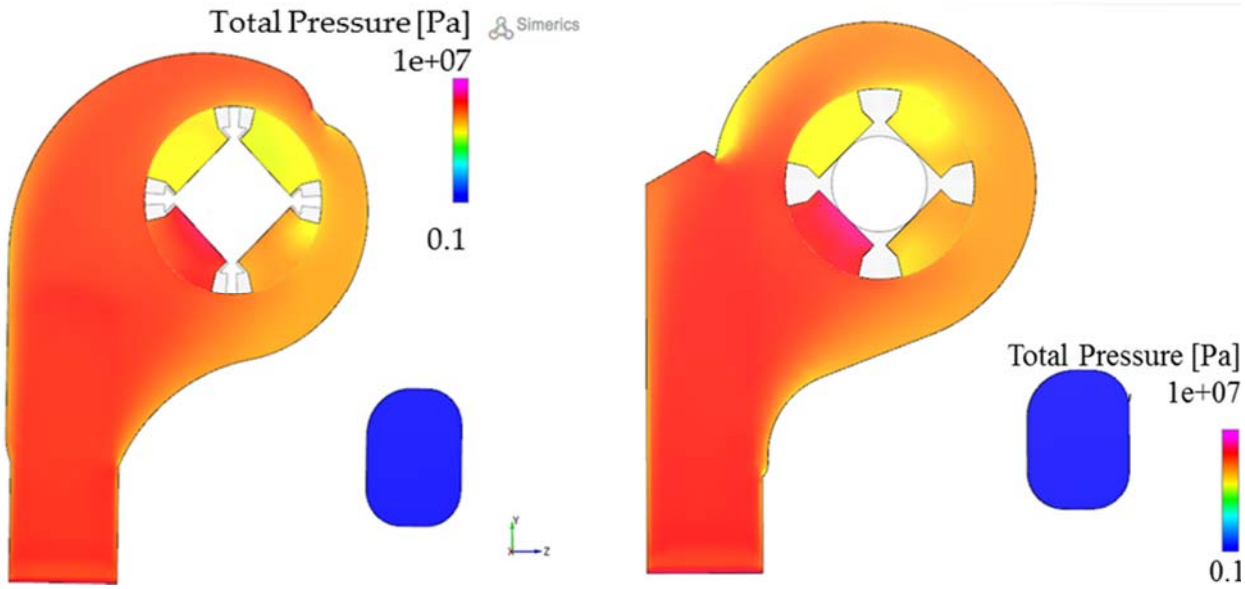

FIGURE 2.119: COMPARISON OF PRESSURE DISTRIBUTION FOR CASE 1 AND CASE 4

In conclusion, the proposed methodology, validated with experimental data, represents the best modelling technique that can be adopted to approach at this type of issues. In this study, in fact, only using a CFD modelling approach the valve internal geometry was presented to reduce, as possible, the fluid-dynamic forces acting on the spool and consequently the torque. This methodology can help to design and optimize a proportional spool valve, providing a great amount of data and insight about the performance of this hydraulic component.

2.6.6 Conclusions

A three-dimensional approach to modeling a new proportional spool valve, by a fluid mechanic study, has been presented in this paragraph. The study shows how to realize a new valve core design with reduced spool torque; the transverse methodology

can be applied in several other application to better understand the internal fluid dynamic of all the hydraulic components.

These components, in the past, were designed based on engineering experience; only in recent years, have some studies for their optimization been started. For this reason, there is little scientific literature in this field.

As said, this study has the main objective to find a new way to better understand the internal fluid dynamics of all valves types. The study has been performed with the modeling methodology studied in this PhD thesis, showing the high flexibility of the technique that demonstrate to be extremely useful also for the improvement of the performance not only of pumps but also of other hydraulic components like valves. The study has allowed the reduction of the internal turbulence through a better core design.

As shown, starting from the initial valve geometry, the new design can obtain a lower spool torque with the same pressure versus flow rate characteristics. The new core design has a modified port P design to give more symmetry to the flow and consequently to reduce the spool torque. The three-dimensional model results were validated with experimental data obtained on an innovative test bench.

The study was approached with a steady state analysis for a spool position where the force on the spool are highest and the torque is maximum.

Using this approach, the internal core valve geometry was re-designed by studying the internal fluid dynamic force and pressure evolution. The flow rate curve derived from the numerical simulations was successfully compared with the experimental flow rate data, showing the high accuracy of this methodology.

The proposed numerical computations demonstrate the high influence of the internal flow-dynamic on proportional spool valve performance. In particular, the results indicate that the unbalanced flow forces acting on the spool influences the spool torque drastically. The goal of this research study was target and the entire fluid-dynamic flux anomalies was find and eliminate.

The possibility to operate with a three-dimensional code, particularly flexible for this type of application, can offer the opportunity to achieve good results in a very low computational time.

2.7 Flow Control Valve

2.7.1 Introduction

As done for in the paragraph 2.6 in this one the 3D CFD modeling approach has been applied for the optimization of a two-way pressure compensated flow control valve. The study is addressed to the reduction of fluid-dynamic forces. During operation, the flow causes forces on the spool. These forces must be correctly balanced. Since these forces cannot be measured, a three-dimensional CFD modeling approach is needed. A case study has been undertaken to verify the approach on the flow control valve. Since forces vary during operation, the analysis must be transient. From the initial zero spool position, the flow goes through the valve causing a spool shift inside the valve's housing until by the spool stops at its final position. Forces depend on the spring reaction, the inlet pressure force, the pressure force of the fluid inside the spool and the spring holder volumes, and the balance of forces influences the outlet flow rate at the final spool position. First, the initial case geometry was modeled, prototyped and tested, and this geometry was studied to verify the model accuracy compared to experimental data. The comparison shows good agreement with a maximum error of 3%. With the same approach several other geometries were designed, but only the best geometry was prototyped and tested. The model was adopted to make several analyses of velocity contouring, streamlines trends, and pressure distribution in the fluid volume. The modeled and tested results achieved the expected performance confirming the effectiveness of the methodology.

2.7.2 Three - Dimensional CFD Model

The valve has been simulated with the commercial CFD program PumpLinx®. From the 3D CAD geometry (figure 2.120), the fluid volume has been extracted (figure 2.121). In figure 2.121 the valve fluid volume is shown [65].

Figure 2.122a shows the binary tree mesh in a section plane of the valve while figures 2.122b show the spool and total volume meshes.

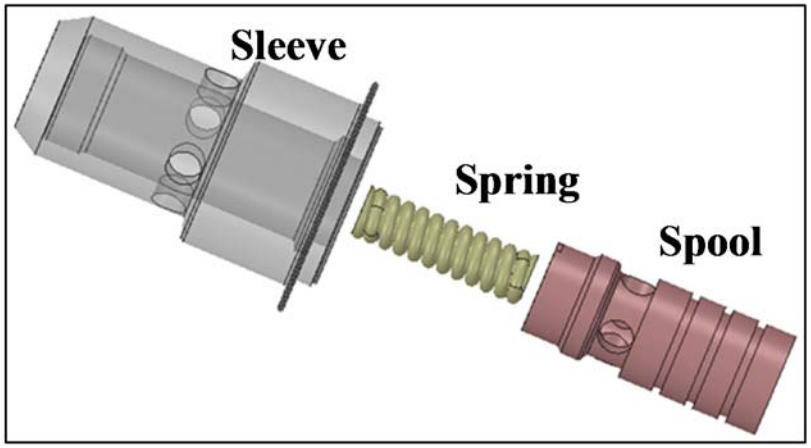

FIGURE 2.120: VALVE CAD 3D

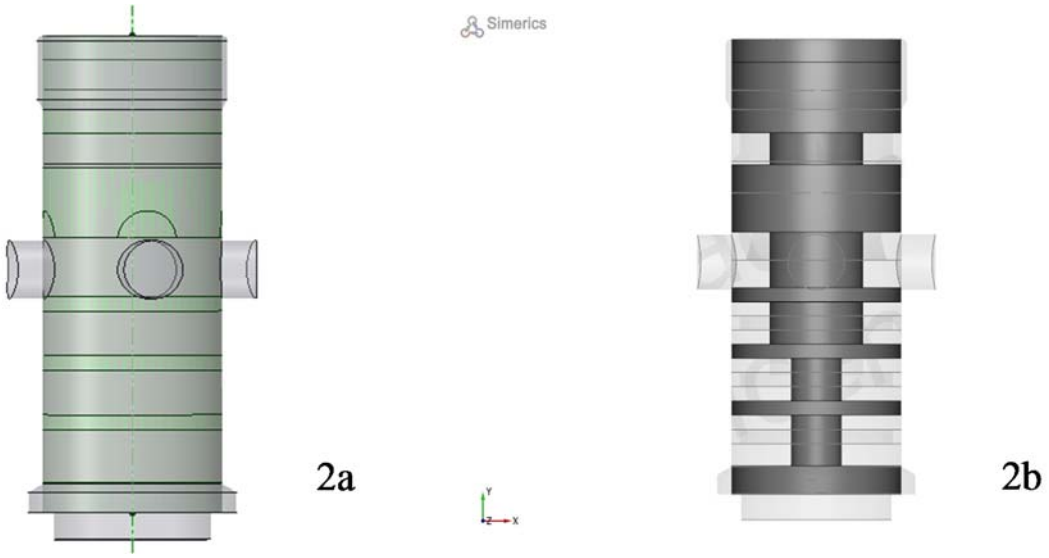

FIGURE 2.121: FLUID VOLUME

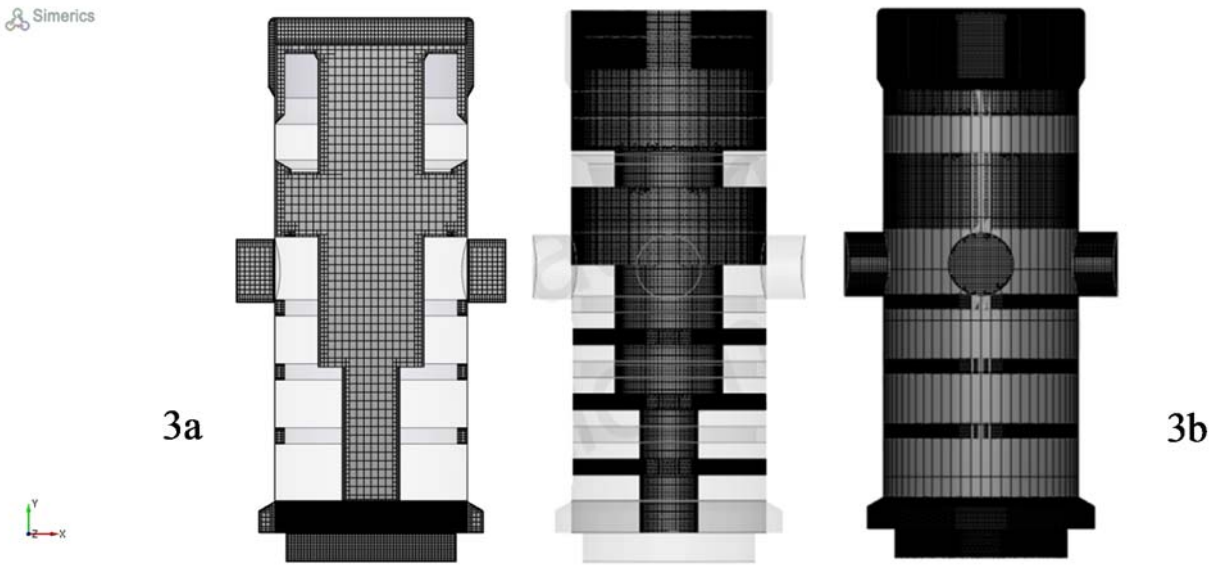

FIGURE 2.122: BINARY TREE MESH – 3A) VALVE SECTION – 3B) SPOOL AND BODY

The valve dynamics is solved taking fluid/solid interaction into account. Due to strong system pressure fluctuations, the coupling between the fluid and valve position can be very stiff. A fully implicit ODE integrator has been implemented in the code to solve the valve dynamics ODE:

$$m\frac{d^2x}{dt^2} = F_{fluid} + F_{spring} + F_{other} \quad (2.34)$$

where x is valve shift, m is valve mass, t is time, F_{fluid} is the integration of fluid forces on valve surfaces obtained from CFD simulation, F_{spring} is the spring forces, and F_{other} accounts for all the other forces applied to the valve. In a transient simulation at each time step, CFD equations are solved. Next, the forces applied to the valve are integrated, and the valve dynamics equation will be solved and the new position of the valve determined. After that, a new valve mesh will be generated based on the new valve position automatically using the function from the valve template, and a new round of simulation will start over.

The boundary conditions were obtained from experimental data performed at an oil temperature of 40°C. Once the model was created, a large number of simulations were run to obtain results for all the internal geometry valve cores at all operating conditions. In figures 2.123, as an example, the pressure distribution in the valve fluid volume is shown. For this simulation, the inlet pressure is at 150bar, the outlet pressure is at 1bar and the spool initial position is zero.

The simulation is a transient analysis therefore the spool is moving inside the valve body until it reaches the final position. The final position, for the settled boundary conditions, is shown in figure 2.123a. The spool final position allows the connection with the output port (at 1bar). The connection areas are underlined in figure 2.123a with two rectangles. In figure 2.123b, the pressure distribution in the oil film between the spool and the valve housing is shown.

The flow streamlines colored by the mean flow velocity (m/s) are shown in figure 2.124. The streamlines can help to analyze the critical zones where vortices are located. In the figure, the spring area and the top volume are shown highlighting the

high vortices present in these areas. By critically analyzing the flow streamlines it is possible to study the forces acting on the valve spool.

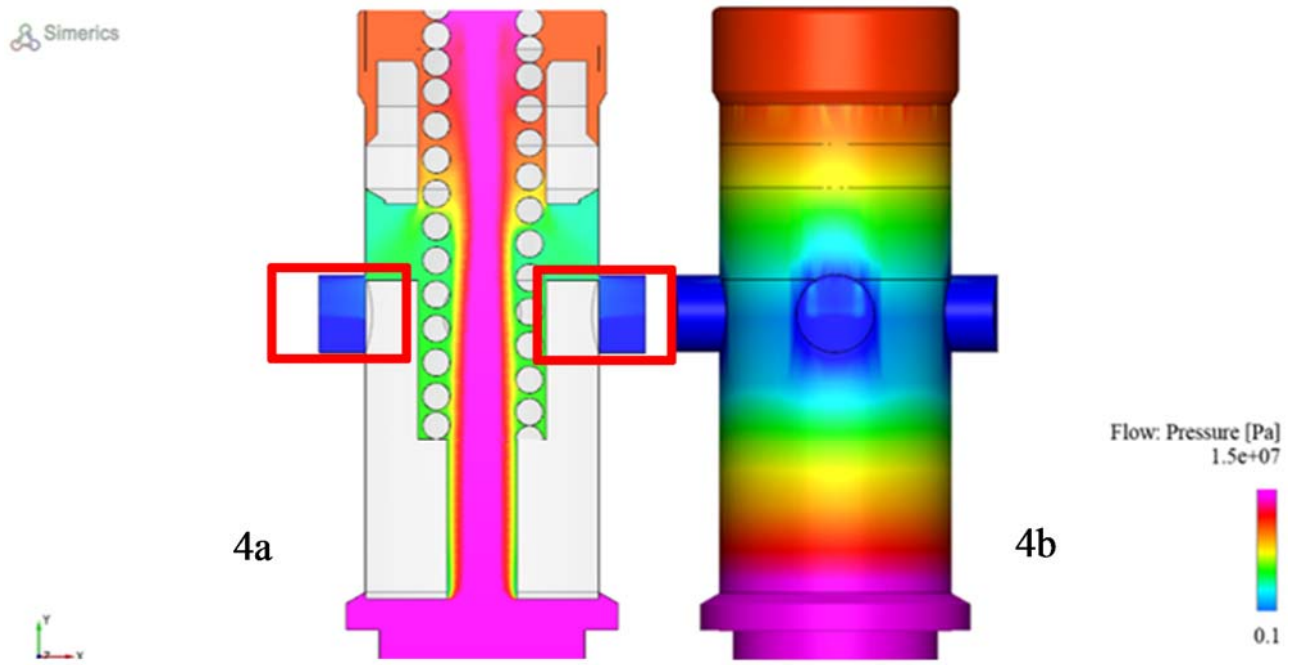

FIGURE 2.123: PRESSURE DISTRIBUTION IN THE FLUID VOLUME

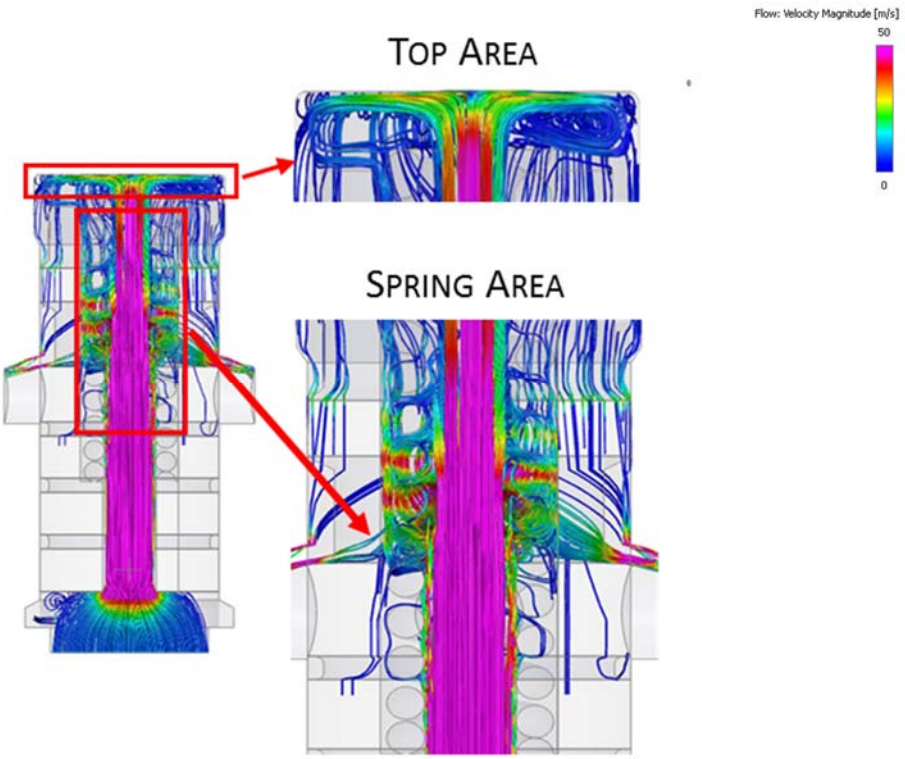

FIGURE 2.124: TYPICAL STREAMLINE COLORED BY VELOCITY MAGNITUDE INSIDE THE SPOOL FLUID VOLUME

By analyzing the results in figures 2.123 and 2.124 it is clear that the main critical area for the valve operation is the duct on the spool inlet side. The pressure distribution and the velocity streamlines confirm that this area must be designed to achieve the expected valve performance.

2.7.3 Experimental Data and Model Validation

The result of the experiments and the valve model validation are now presented.

The experimental data were obtained on the hydraulic test bench of the University of Naples "Federico II".

Experimental Data

The valve model validation has been performed using data from experiments made on a hydraulic test bench; the hydraulic scheme is represented in figure 2.125.

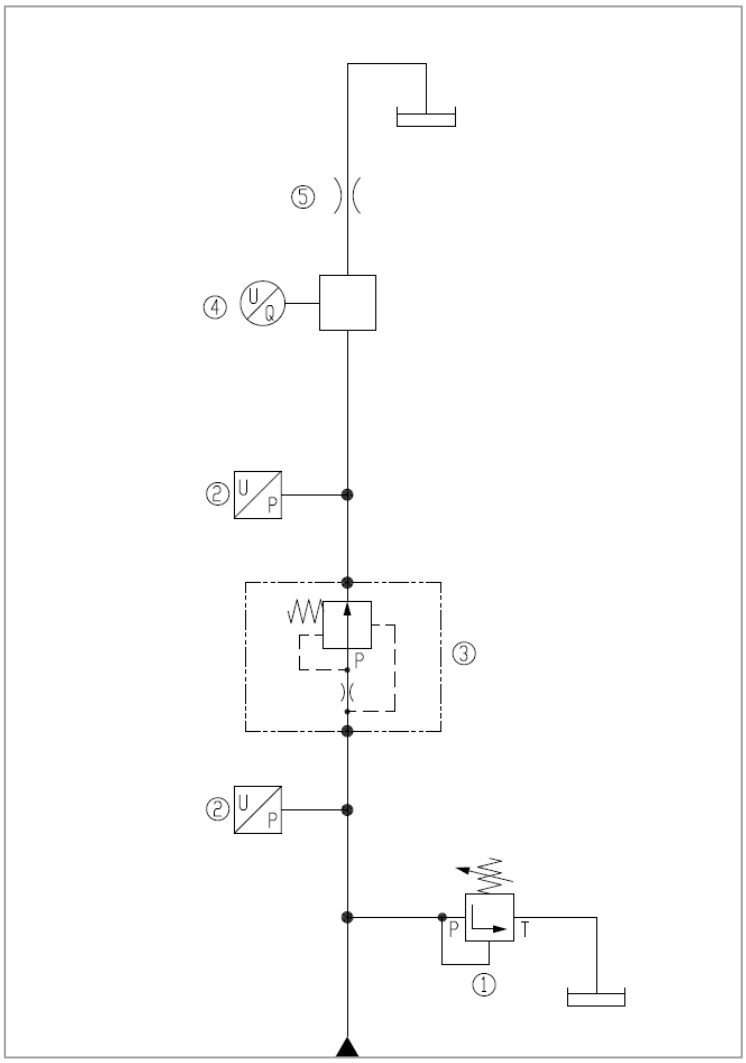

FIGURE 2.125: TEST BENCH HYDRAULIC SCHEME

The test bench is composed of a relief vale (1), two pressure transducers (2), the tested flow control valve (3) a flow-rate transducer (4) and a lamination valve (5). The flow rate transducer is model VS10GPO12V from VSE.flow® with a maximum flow rate of 525 l/min and a maximum operating pressure of 420 bar. The pressure transducer is type HDA 4400 from Hydac® with an operating range of up to 400 bar. The transducers output signals has been acquired and processed by the DAQCardTM - 6062E data acquisition system from National Instruments®. The tests were performed at a constant temperature of 40°C with Mobil DTETM 25 (ISO VG 46) oil.

Model Validation

The model validation is shown in figure 2.126 comparing the experimental data (continue line) with the model results (dashed line).

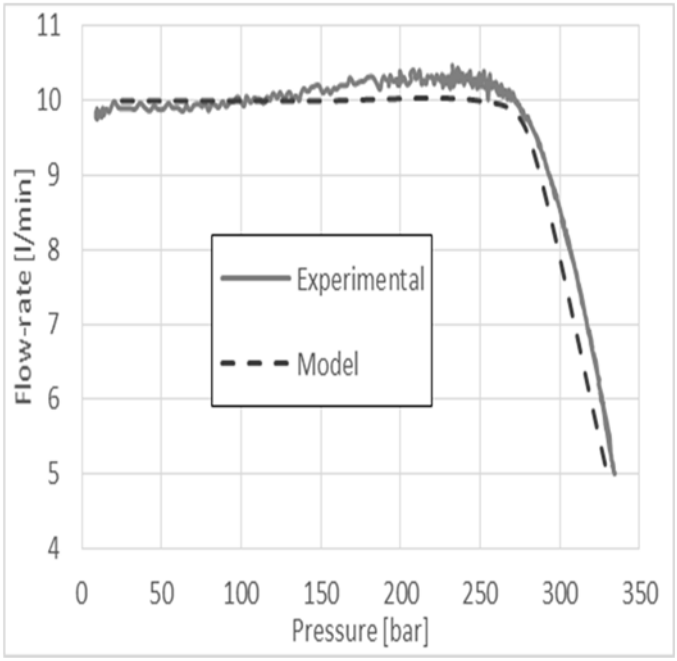

FIGURE 2.126: EXPERIMENTAL/MODEL RESULTS COMPARISON

Overall, the difference between model results and experimental data is less than 2%. Looking at figure 2.126, the flow rate is always near 10 l/min but the target for this valve size is a flow rate of 6.5 l/min. Starting from the initial geometry, the goal of the study is to reduce the flow rate by modifying the valve geometry. It was decided that the flow - rate reduction must be achieved solely by redesigning the valve internal geometry without modifying the spring.

2.7.3 Model Application: New Valve Design

The results obtained with the initial model show a flow rate of 10 l/min. By comparing model results and experimental data it was verified that the error is always less 2%. The methodology has proved to be accurate also is applied on valves. Therefore it was applied to several other geometries. All the principal parts of the valve were critically analyzed using three-dimensional flow visualization. The study demonstrates that the main influence on the performance is the geometry of spool inlet duct. It was also found that the inlet port was one of the most critical zones for vorticity and pressure drop.

Starting from the initial case (called Case1), by varying the inlet spool diameter, two new geometries were created. The main differences in these geometries are shown in figures 2.127 and 2.128. In particular, figure 2.127 shows the solid geometries of core and spool in a cross section.

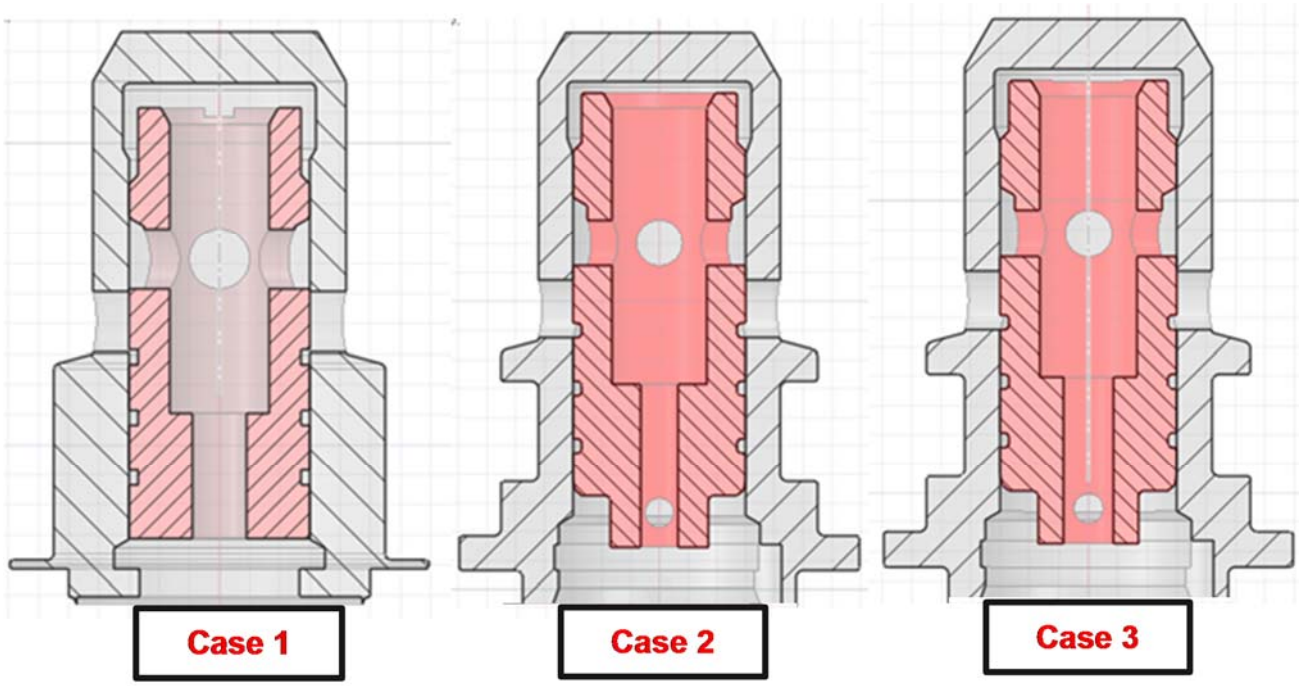

FIGURE 2.127: NEW VALVE DESIGNS

Figure 2.128 shows fluid volumes comparison of all the geometries.

Two important modifications were done:

- The diameter of the connection with the top valve has been reduced from the initial value of 1.8mm to 1.7mm (Case 3) and 1.3mm (Case 2),
- The spool bottom side has been modifies as shown in figure 2.129 with the comparison between the Case 1 and Case 3.

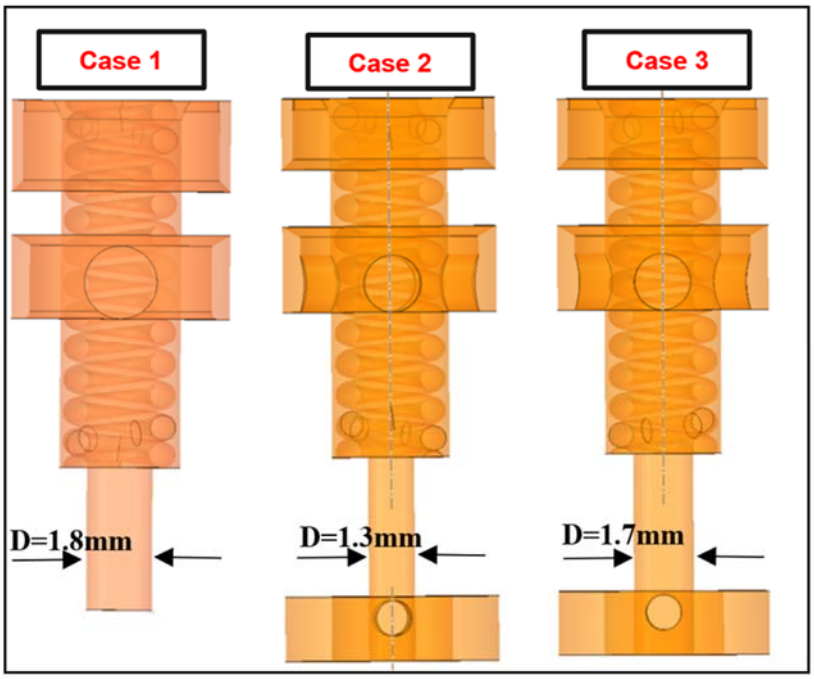

FIGURE 2.128: NEW SPOOL DESIGNS

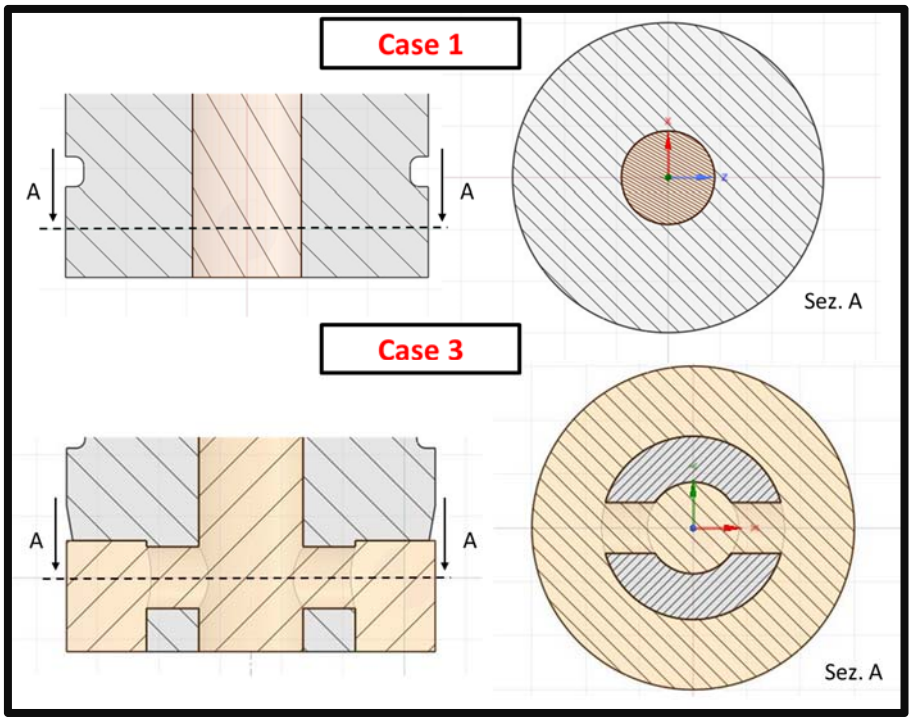

FIGURE 2.129: SECOND GEOMETRY MODIFICATION ON THE SPOOL

The diameter has been changed to reduce the outlet flow rate from the Case 1 while the second modification facilitates the inflow to the spool. The second geometry modification is shown in figure 2.129 where the comparison is only made between Case 1 and Case 3 because the variation in Case 2 is the same as Case 3. In Case 1, the spool is directly connected with the valve inlet by one duct (D = 1.8mm). Cases 2 and 3 have a fluid circular section cross-linked, by four radial ducts, attaching to the main duct. The additional fluid volume improves the valve operation.

For each case the fluid volume was extracted and meshed and models were run with the same boundary conditions as Case 1. Models results are shown in table 2.10. The table reports the comparison with the modeled flow - rate data between each case. The result is a reduction of flow rate from 10 l/min of the Case 1 to 3.2 l/min of the Case 2 and 6.5 l/min for Case 3. Since Case 3 has the desired flow rate of 6.5 l/min, its geometry was used prototyping.

FLOW - RATE		
Case1	Case2	Case3
9.25 [l/min]	3.20 [l/min]	6.51 [l/min]

TABLE 2.10: TORQUE METER TRANSDUCER CHARACTERISTICS

A better understanding of the relationship between flow pattern and performance can be seen by comparing the three cases based on pressure distribution, velocity contouring and flux streamlines. In figure 2.130, a comparison between the streamlines inside the spool fluid volume for each case is shown. This result reveals the areas of high vorticity in the fluid volumes.

The fluid velocity inside the spool decreases from the Case 1 to the others. Comparing Case 1 to Case 3, the velocity in the suction duct decreases from 50 m/s to 40 m/s. Less evident is the velocity reduction of the Case 2. Using this three-dimensional CFD approach, it is also possible to investigate the pressure distribution

in a fluid volume. Figure 2.131a and 2.131b show the pressure distribution in the spool and in the entire fluid volume for each case.

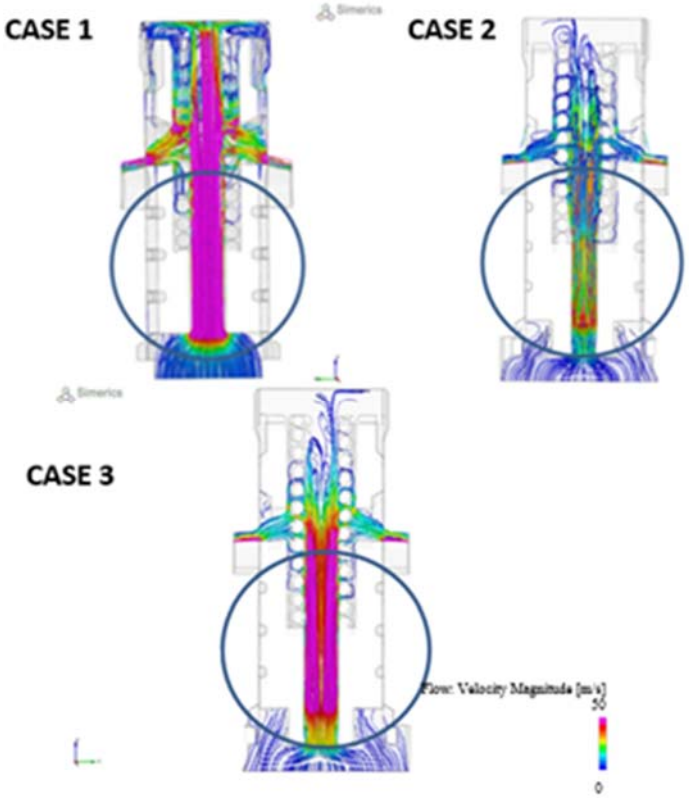

FIGURE 2.130: STREAMLINES INSIDE THE FLUID VOLUME

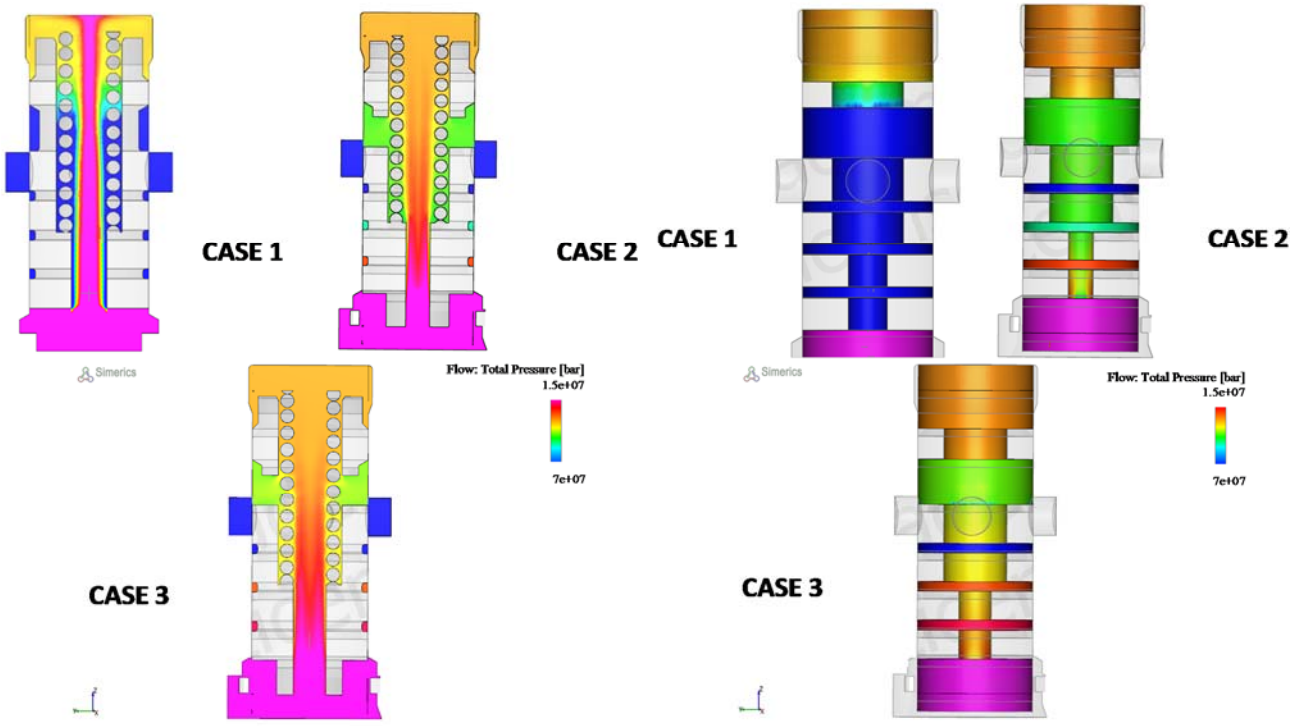

FIGURE 2.131: PRESSURE DISTRIBUTION IN THE VALVE SECTION (A) AND SPOOL VOLUME (B)

The force balance on the spool depends on the spring constant, the inlet pressure force, the pressure force of the fluid inside a top spool area, and the pressure force of the fluid inside the spool. The spool position only depends on the flow forces magnitudes since the spring stiffness has not been changed. Figure 2.132 shows a comparison the pressure distribution in the top volume (fluid volume in the spring chamber, called Volume 3) and the pressure distribution in the bottom volume (fluid volume in the valve inlet, called Volume 1) where Volume 1 and Volume 3 are clearly shown in figure 2.133.

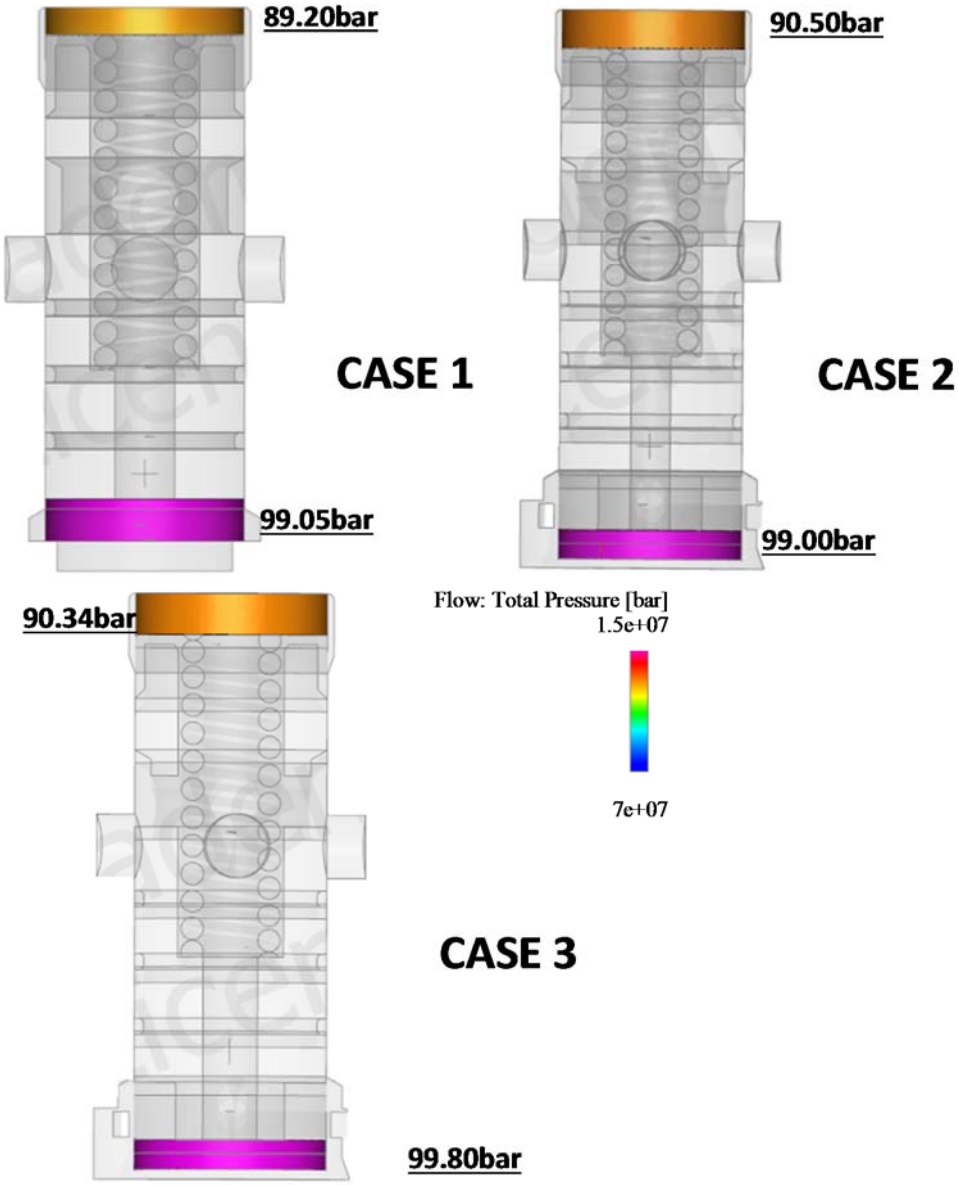

FIGURE 2.132: PRESSURE INSIDE THE TOP AND BOTTOM SPOOL AREA

In table 2.11, the average pressure for Volumes 1 and 3 is shown for the three cases. This table shows that the geometric variations applied do not greatly influence the top and bottom volume pressures. Therefore, the results clearly confirm that the main effect responsible for differing valve operation is the force generated by the spool's internal fluid dynamics. This shows how results obtained from the modeling study have provided an understanding of valve operation without experimentation.

PRESSURE			
CASE	Case 1	Case 2	Case 3
VOLUME 1 [bar]	99.05	99.00	99.80
VOLUME 3 [bar]	89.20	90.50	90.34
ΔPRESSURE [bar]	9.82	8.50	9.46

TABLE 2.11: AVERAGE PRESSURES INSIDE THE TOP AND BOTTOM SPOOL AREAS

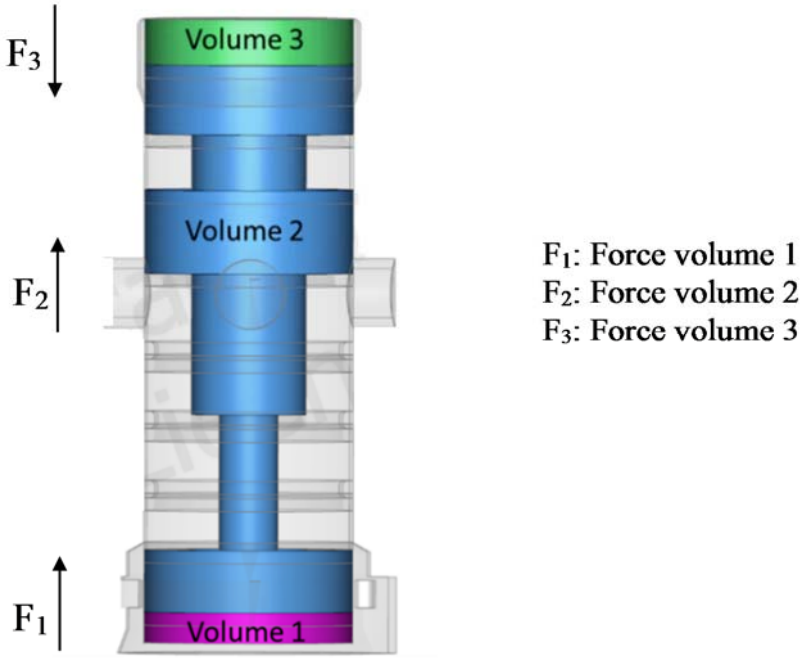

FIGURE 2.133: VALVE FLUID VOLUME – FORCES STUDY

CFD model allows estimating the final spool position inside the valve. For Cases 1, 2 and 3, the spool shift is 1.26 mm, 0.88 mm and 0.93 mm. Other useful model results are shown in figure 2.134 where the spool shift in function of the time is shown. The spool for the three cases has different final position. For all the cases from the zero

position the spool goes up, reaches its maximum height, goes down and, finally stabilized.

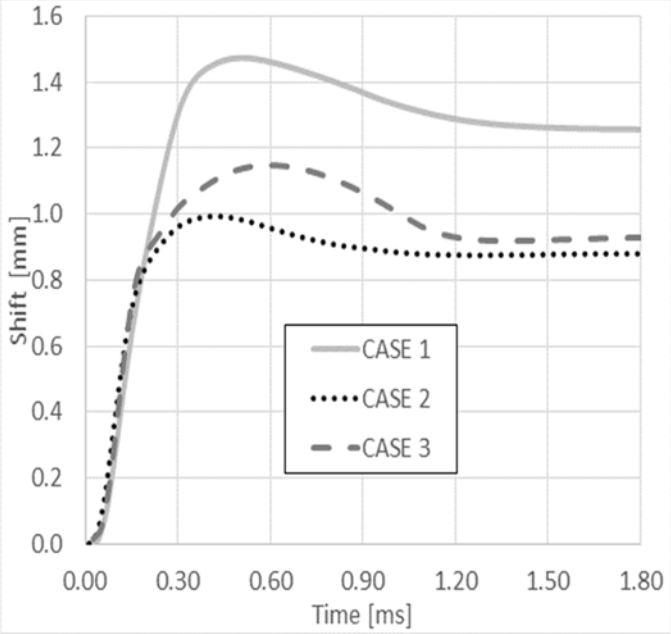

FIGURE 2.134: SPOOL SHIFT VS TIME

The trend is the same for all the cases but maximum shift and the final spool position are reached at different times. In particular, Case 3 has a slower response over 0.30 to 0.60 ms, while the two cases (Case 1 and Case 2) respond more quickly. The more gradual behavior of Case 3 is the result of the spool internal fluid dynamic optimization (figure 2.128) that allows achieving the flow - rate target (see table 2.10).

The spool position is function of the internal forces acting on the spool. The force values are shown in table 2. The forces for Cases 2 and 3 are always less than for Case 1.

Force [N]			
Force	Case 1	Case 2	Case 3
$F_{sring\_preaload}$	-11.8	-11.8	-11.8
F_{other}	-23.0	-14.9	-15.6
F_{fluid}	34.8	26.7	27.4

TABLE 2.12: FORCE COMPONENTS FOR THE THREE CASES STUDIED

Figure 2.135 shows the net force of the three component of the F_{fluid} in table 2.12 [71 - 72].

$$F_{fluid} = F_1 + F_2 + F_3 \quad (2.35)$$

Case 2 has the minimum spool shift value and the flow rate is less than Cases 1 and 3. Results presented in table 2.12 are consistent with the results shown in figure 2.136 where the net force are plotted as a function of the time. This force is sum of three components:

$$F_{net} = F_{fluid} + F_{spring\_preload} + F_{other} \quad (2.36)$$

Forces vary and then fluctuate around zero when the spool reaches the final position. From the initial position, the spool moves within 1 ms to the final position.

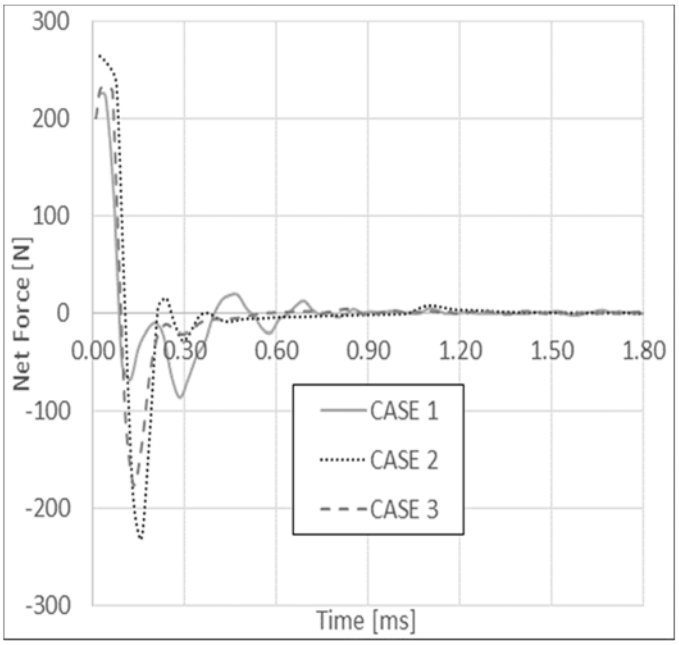

FIGURE 2.135: SPOOL NET FLUID ON THE SPOOL VS TIME

Since the most desirable case is Case 3, a prototype of this design was built and tested. The experiments were performed on the hydraulic test bench at the University of Naples "Federico II". A comparison between the model and the experimental results is shown in figure 2.136, confirming an experimental error of less than 2%. Other studies already made on other hydraulic components [4, 5, 73] show the flexibility of the method where in all cases the accuracy is good. The presented approach is useful

because it allows researchers to study the complex fluid dynamic phenomenon in the hydraulic components revealing details that are extremely difficult to measure experimentally.

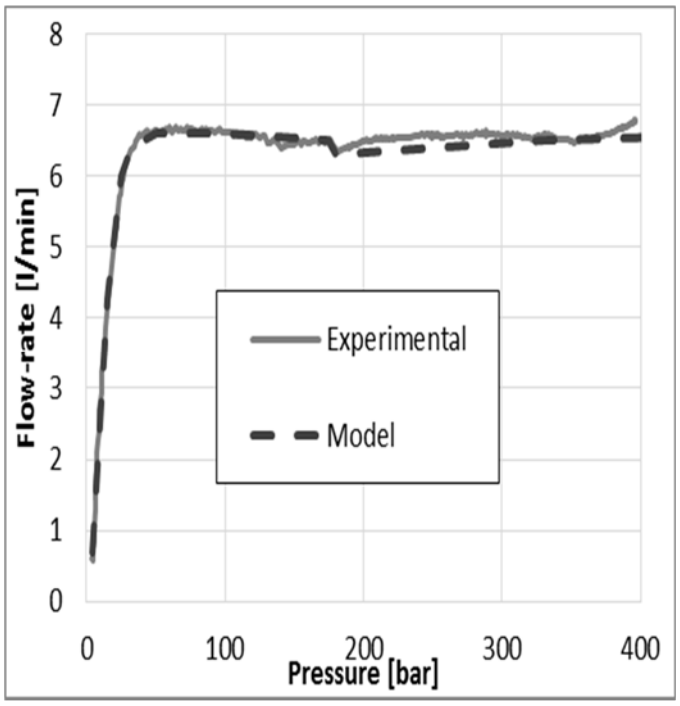

FIGURE 2.136: EXPERIMENTAL/MODEL RESULTS COMPARISON, CASE 3

2.7.4 Conclusions

A new apprilaion of the three-dimensional CFD approach described in this thesis model to model hydraulic components was been presented in this paragraph. With current computational capabilities, three-dimensional computational CFD codes can achieve good results with a very low computational time. As an example, a two-way flow control valve was studied. With this approach, a new spool design enabled the valve to achieve he required flow rate with a large reduction of the vorticity induced by internal geometry features. From the fluid dynamic analysis the flow behavior was improved to create a design with more regular fluid path lines, reducing the flow forces and allowing a more gradual spool shift during the valve actuation.

The three-dimensional flow model results of the initial design were validated with experimental data with a maximum error of 2%. The validated approach was then used to design a new valve optimizing the geometry using the CFD code. The

optimized design was used to construct a prototype and the results agree with the experimental data with an error of less than 3%. Thanks to the three-dimensional CFD visualization, this research activity has allowed our team to gain a thorough knowledge of the complex fluid dynamic phenomena of hydraulic components.

CONCLUSIONS

In this PhD thesis a three-dimensional Computational Fluid Dynamics (CFD) modeling technique has been presented. The methodology has been developed by the Hydraulic Research Group of the University of Naples "Federico II" led by Professor Adolfo Senatore in close collaboration with the Center for Compact and Efficient Fluid Power at the University of Minnesota led by the Professor Kim A. Stelson. The methodology has been applied for the study of hydraulic components used in different applications in the industrial field and on engines for the lubrication circuits. Studies have confirmed that the proposed three-dimensional CFD modeling technique is the best methodology to optimize of the internal fluid dynamics of components. Research have been focused on the design and optimization of:

1) Hydro - Mechanical Transmission,
2) Variable Displacement Vane pump,
3) Gerotor Pumps,
4) Engine Lubrication Circuit,
5) Pumps as Turbine (PAT),
6) Directional Spool Valve,
7) Flow Control Valve.

The study showed in detail all the steps needed for the optimization process starting from the initial design of the component, to the creation of the numerical model and then to the critically analysis of the simulation results. All the three-dimensional model results were validated with experimental data demonstrate a high accuracy.

Thanks to the flexibility of applications, this thesis can be used as a guide for future studies. The wide range of examples presented is only a small subset of possilbe studies of hydraulic components.

As shown, the modeling methodology has the advantage to being able to simulate the real performance of components in a simplified manner. This avoids the need for onerous simulations tasks and experiments. It is also possible to estimate variables that are difficult or impossible to measure experimentally.

From the implementation of particular capabilities, such as the cavitation sub-model, it is possible to anticipate malfunctions and find solutions to avoid them.

The methodology can be applied for both for the design of a new component and for the optimization of an existing one. Several geometries can be modeled to find the best one to prototype and test experimentally.

The proposed technique has demonstrated to give consistent advantage to the study hydraulic components in detail. By analyzing the internal fluid dynamics using three-dimensional simulation, the velocity, kinetic energy and pressure fields in the fluid volume can be known.

NOMENCLATURE

n	Surface normal
k	Turbulence kinetic energy
LVDT	Linear Variable Displacement Transducer
p	Pressure (Pa)
Q	Flow rate (m3/h)
U	Initial velocity
u	Velocity component (m/s)
u’	Component of v’
v	Velocity vector
v’	Turbulent fluctuation velocity
μ	Fluid viscosity (Pa-s)
μ_t	Turbulent viscosity (Pa-s)
ρ	Fluid density (kg/m^3)
τ	Stress tensor
η	Dynamic viscosity [Pa-s]
ρ_g	Gas density (kg/m^3)
ρ_l	Liquid density (kg/m^3)
ρ_v	Vapor density (kg/m^3)
p_s	Oil supply pressure [Pa]
C_c	Cavitation model constant

C_e	Cavitation model constant
f_v	Vapor mass fraction
f_g	Non-condensable gas mass fraction
R_e	Vapor generation rate
R_c	Vapor condensation rate
D_f	Diffusivity of vapor mass fraction
G_t	Turbulent generation term
ε	Turbulence dissipation
S'_{ij}	Strain tensor
RNG	Re-Normalization Group
LES	Large Eddy Simulation
DES	Detached Eddy Simulation
Q_c	Flow at the control port of the HMT
ω_p	Input shaft speed of the VPSU
ω_m	Output shaft speed of the VPSU
D_p	Pump displacement
η	volumetric efficiency
p_c	Pressure control
F_v	Force caused by the pressure difference in the small radius region of the vane
P_i	Power at the input port of the HMT

P_o	Power at the output port of the HMT
T_p	Torque at input shaft speed of the HMT
T_m	Torque at output shaft speed of the HMT
R	Average cam radius
T_n	Torque due to the friction between the vane tip and the cam contour
Z	number of vanes
F_t	Friction force
r	Displacement ratios of the HMT
ω_i	Input shaft speed of the VPSU
ω_o	Output shaft speed of the VPSU
Q_{teo}	Gerotor pump theoretical flow-rate
V_g	Gerotor pump displacement
Q_{eff}	Gerotor pump reeal flow-rate
Q_h	Flow-rate through the groove/hole of a bearing
F_{fluid}	Fluid force due to fluid-dynamic of a spool valve
F_{spring}	Fluid force due to the spring of a spool valve
F_{other}	Other force acting on the spool of a valve
Q_p	Pressurized lubricant flow from the hole or groove [m3/s]
p_s	Oil supply pressure [Pa]
f_1, f_2	Coefficients

h_c	Film thickness at the position of the groove [m]
c	Radial clearance [m];
d_h	Diameter of the hole [m];
L	Axial length of the bearing [m]
l	Axial length of the groove [m]
b	Width of the groove in the sliding direction [m]
D	Diameter of the bush [m]
ε	Eccentricity ratio
N_s	Specific speed
H	pump head
H_t	Turbine head
β	groove

ACKNOWLEDGEMENTS

This research has been supported by: the Department of Industrial Engineering of the University of Naples “Federico II”, the Center for Compact and Efficient Fluid Power (National Science Foundation Engineering Research Center funded under cooperative agreement number EEC-0540834), the Department of Mechanical Engineering of the University of Minnesota, the Italian company Duplomatic Oleodinamica S.p.A. and by the Australian company Mathers Hydraulics®.

I need to thank:

1) The Professor Adolfo Senatore for the human and technical supports. All the above researches come only from him incredible ideas.
2) The Professor Kim A. Stelson to give me the opportunity to study and work at the University of Minnesota for a year. Thanks also to his wife Caren Stelson for her humanity; she welcomed me as one of her daughter making me feel like at home,
3) The Eng. Dario Buono for the technical support. He helped me for all the researches made during the three years of my PhD,
4) The Italian Company Duplomatic Oleodinamica S.p.A. that supported me for the study period at the University of Minnesota. I appreciate the technical support from the Eng. Michele Pavanetto and the Eng. Ina Costin and the support from the company CEO Roberto Maddalon,
5) The Australian Company Mathers Hydraulics® that supported my research at the University of Minnesota. A special thanks to the CEO Norm Mathers and the Eng. Rob Price,
6) The US Company Continental Hydraulic Inc. that supported me for a research period in US. I appreciate the technical support from the engineers Wade Gehlhoff, Bob Allen, Bryan Edlund and Mike Voight. Thanks also to the company CEO David Zimmer.
7) The US Company Simerics®. In particular, thanks to the CEO Sam Lowry and to Haiyang Gao for the technical support.

8) The Eng. Federico Monterosso and the Eng. Micaela Olivetti of the Italian Company OMIQ srl,
9) The Eng. Michal Gust and the Eng. Brad Bohlmann of the Center for Compact and Efficient Fluid Power of the University of Minnesota,
10) The Post Doc. Feng Wang and the PhD Student Biswaranjan Mohanty of the University of Minnesota for the human and technical supports,
11) The Professor Fabio Bozza as head of the PhD course at the University of Naples "Federico II",
12) The Professor Rita M. A. Mastrullo as coordinator of the project "POR CAMPANIA FSE 2007-2013 / Reti di Eccellenza" that support my for a period in US,
13) The Professor Antonio Moccia as head of the Department of Industrial Engineering at the University of Naples "Federico II",
14) The technicians of the labs at Department of Industrial Engineering - University of Naples "Federico II". A particular thanks to Gennaro Stingo, Giuseppe Iovino, Marco Di Pilla, Rosario Moreschi, Umberto Cesaro.

REFERENCES

[1] Ferziger, J. H. and Peric, M., (2002) “Computational Methods for Fluid Dynamics”, Springer,

[2] Ding, H., Visser, F.C., Jiang, Y., Furmanczyk, M., (2009) “Demostration and Validation of a 3D CFD Simulation Tool Prediction Pump Performance and Cavitation for Industrial Applications”, ASME Fluids Engineering Division Summer Meeting,

[3] Senatore, A., Buono, D., Frosina, E., Arnone, L., Santato, L., Monterosso, F., Olivetti, M., (2013), “A tridimensional CFD analysis of the lubrication circuit of a non-road application Diesel engine”. 11th International Conference on Engines and Vehicles, ICE 2013,

[4] Senatore, A., Buono, D., Frosina, E., Manganelli, M. U., Olivetti, M., (2014), “A Tridimensional CFD Analysis of the Oil Pump of an High Performance Motorbike Engine”, ENERGY PROCEDIA, **45**, p. 938-948,

[5] Senatore, A., Buono, D., Frosina, E., Stelson, K. A., (2016), “A Mathematical Model to Analyze the Torque Caused by Fluid-Solid Interaction on a Hydraulic Valve”, ASME Journal of Fluids Eng., **138**(6),

[6] Singhal, A.K., Athavale, M.M., Li, H.Y., Jiang, Y., (2002), “Mathematical Basis and Validation of the Full Cavitation Model", ASME Journal of Fluids Eng., 124, pp. 617-624,

[7] Arndt, R.E.A., (1981) “Cavitation in fluid machinery and hydraulic structures,” Annual Review of Fluid Mechanics, **13**, pp. 273 – 328,

[8] Bahir, F., Rey, R., Gerber, A.G., Belamri, T., Hutchinson, B., (2004), “Numerical and experimental investigations of the cavitating behavior of an inducer,” International Journal of Rotating Machinery, **10**, pp. 15-25,

[9] Brennen, C.E., (1995), ”Cavitation and Bubble Dynamics”, Oxford University Press,

[10] Dupont, P., Okamura, T., (2003), “Cavitating flow calculations in industry,” International Journal of Rotating Machinery, **9**, pp. 163-170,

[11] Schleihs, C., Viennet, E., Deeken, M., Ding, H., Xia, X., Lowry, S., Murrenhoff, H., (2014), "3D-CFD simulation of an Axial Piston Displacement Unit, The 9th International Fluid Power Conference, **3**, pp. 332-343,

[12] Mohanty, B., Wang, F., Stelson, K.A., (2015), "Design of a Vane Pump Power Split Transmission for a Highway Vehicle" The Fourteenth Scandinavian International Conference on Fluid Power,

[13] Wang, F., Stelson, K.A., (2014), "A Novel Pressure-Controlled Hydro-Mechanical Transmission", ASME/BATH 2014 Symposium on Fluid Power & Motion Control,

[14] E. Frosina, A. Senatore, D. Buono, K. A. Stelson, F. Wang, B. Mohanty, M. J. Gust, (2015), " Vane pump power split transmission: three dimensional computational fluid dynamic modeling", ASME/BATH 2015 Symposium on Fluid Power and Motion Control,

[15] Inaguma, Y., (2010), "Theoretical analysis of mechanical efficiency in vane pump", JTEKT Engineering Journal English Edition, No. 1007E Technical paper, pp. 28-35,

[16] Inaguma, Y., and Hibi, A., (2005), "Vane pump theory for mechanical efficiency", Proceedings of the IMechE Part C: J. Mechanical Engineering Science, **219**, pp. 1269-1278,

[17] Inaguma, Y., and Hibi, A., (2007), "Reduction of friction torque in vane pump by smoothing cam ring surface", Proceeding of the IMechE Part C: J. Mechanical Engineering Science, **221**, pp. 527-534,

[18] Cho, I.S., Oh, S.H., Song, K.K., and Jung, J.Y., (2006), "The lubrication characteristics of the vane tip under pressure boundary condition of oil hydraulic vane pump", J. mechanical science and technology, **20**(10), pp. 1716-1721,

[19] Karmel, A.M., (1986), “A study of the internal forces in a variable-displacement vane-pump-Part I: A theoretical analysis”, ASME. J. Fluids Eng., **108**(2), pp. 227-232,

[20] Stachowiak, G. W., Batchelor, A. W., (2001), “Engineering Tribology”, Butterworth, Heinemann,

[21] Williams, A., (1995), “Pumps As Turbines: A user's guide”, London: Intermediate Technology Publications,

[22] Arriaga M., (2010), “Pump as turbine – A pico-hydro alternative in Lao People’s Democratic Republic”, Renewable Energy, **35**(5),

[23] Ivantysynova, M., Ivatysyn, J., (2001), “Hydrostatic Pumps and Motors”, Akademic Books International,

[24] Derakhshan, S. and Nourbakhsh, A., (2008), “Experimental study of characteristic curves of centrifugal pumps working as turbines in different specific speeds”, Experimental Thermal and Fluid Science, **32**(3), 800-807,

[25] Williams, A.A., Rodrigues, A., Singh, P., Nestmann, F. and Lai, E., (2003), “Hydraulic analysis of a pump as a turbine with CFD and experimental data”, IMechE seminar, Computational Fluid Dynamics for Fluid Machinery,

[26] Nautiyal H., Varun, Kumar A., (2010), “Reverse running pumps analytical, experimental and computational study: A review”, Renewable and Sustainable Energy Reviews, **14**(7), 2059–2067,

[27] Nautiyal H., Varun, Kumar Anoop, and Yadav S., (2010), “CFD Analysis on Pumps Working as Turbines”, HYDRO NEPAL, Issue 6, pp. 35-37,

[28] Carravetta, A., Del Giudice, G., Fecarotta, O., Ramos, H., (2013), “PAT design strategy for energy recovery in water distribution networks by electrical regulation”, Energies 2013, **6**, 411–424,

[29] Carravetta, A.; Del Giudice, G.; Fecarotta, O.; Ramos, H., (2013), “Pump as Turbine (PAT) Design in Water Distribution Network by System Effectiveness”, Water 2013, **5**, 1211-1225,

[30] Derakhshan, S., Nourbakhsh, A. and Mohammadi, B., (2009), "Efficiency improvement of centrifugal reverse pumps" ASME Journal of Fluids Engineering, **131**(2),

[31] Natanasabapathi, SR. and Kshirsagar, JT., (2004), "Pump as turbine - an experience with CFX 5.6", Corporate Research and Eng. Division, Kirloskar Bros,

[32] Barrio, R., et al., (2010), "Performance prediction of a centrifugal pump working in direct and reverse mode using Computational Fluid Dynamics", International Conference on Renewable Energies and Power Quality,

[33] Chapallaz, J.M., Eichenberger P., Fischer, G., (1992), "Manual on pumps used as turbines", Friedr Vieweg & Sohn Verlagsgesellschaft, Braunschweig,

[34] Childs, S.M., (1962), "Convert pumps to turbines and recover HP", Hydro carbon processing and petroleum refiner, **41**(10), pp. 173-174,

[35] McClaskey, B.M., Lundquist, J.A., (1976), "Hydraulic power recovery turbines", Joint Petroleum Mechanical Engineering and Pressure Vessels and Piping Conference, Mexico City, pp. 1-11,

[36] Lueneburg, R., Nelson, R.M., (1985), "Hydraulic power recovery turbines", Centrifugal Pumps: Design and Applications,

[37] Hancock, J.W., (1963), "Centrifugal pump or water turbine", Pipe Line News, pp. 25-27, June 1963,

[38] Grover, K.M., (1980), "Conversion of pumps to turbines", GSA Inter Corp., Katonah, New York, USA,

[39] Lewinsky-Keslitz, (1986), "Pumpen als Turbinen fur Kleinkraftwerke", Wasserwirtschaft, **77**(10), 531–537,

[40] Derakhshan, S. and Nourbakhsh, A., (2008), "Theoretical, numerical and experimental investigation of centrifugal pumps in reverse operation", Experimental Thermal and Fluid Science, **32**(8), pp. 1620-1627,

[41] Amirante, R., Moscatelli, P.G., and Catalano, L.A., (2007), "Evaluation of the flow forces on a direct (single stage) proportional valve by means of a

computational fluid dynamic analysis", Energy Conversion and Manage, **48** (3), pp. 942-953,

[42] José, R., Valdés, Miana, M. J., Núñeza, J. L., and Pützb, T., (2008), "Reduced order model for estimation of fluid flow and flow forces in hydraulic proportional valves", Energy Conversion and Manage., **49**(6), pp. 1517–1529,

[43] Amirante, R., Catalano, L.A., and Tamburrano, P., (2014), "The importance of a full 3D fluid dynamic analysis to evaluate the flow forces in a hydraulic directional proportional valve", Engineering Comput., **31**(5), pp.898 – 922,

[44] Lisowski, E., Czyzycki, W., and Rajda, J., (2013), "Three dimensional CFD analysis and experimental test of flow force acting on the spool of solenoid operated directional control valve", Energy Consers. Manage, **70**, pp. 220 – 229,

[45] Amirante, R., Del Vescovo, G., and Lippolis, A., (2006), "Flow forces analysis of an open center hydraulic directional control valve sliding spool", Energy Consers. Manage, **47**(1), pp. 114 – 131,

[46] Plau-Salvador, G., Gonzalez-Altozano, P., and Arviza-Valverde, J., (2008), "Three-dimensional modeling and geometrical influence on the hydraulic performance of a control valve", ASME J. Fluids Eng. **130** (1), pp. 011102,

[47] Amirante, R., Catalano, L.A., Tamburrano, P., and Poloni, L.A., (2014), "Fluid-dynamic 1design optimization of hydraulic proportional directional valves", Eng. Optim., **46**(10), pp. 1295 – 1314,

[48] Lee, G.S., Sung, H.J., and Kim, H.C., (2013), "Multiphysics Analysis of a Linear Control Solenoid Valve", ASME J. Fluids Eng. **135**(1), p. 011104,

[49] Jin, B., Zhu, YG, Li, W., Zhang, D.S., Zhang, L.L., and Chen, F.F., (2014), "A differential control method for the proportional directional valve", J. Zhe-jiang Univ., Sci., C, **15**(10), pp. 892 – 902,

[50] Canuto, E., Acuna-Bravo, W., Agostani, M., and Bonadei, M., (2014), "Digital current regulator for proportional electro-hydraulic valves with unknown disturbance rejection", ISA Trans., **53**(4), pp. 909 – 9019,

[51] Jia, WH., Yin, CB., and Cao, DH., (2014), "Research of median-nonlinear flow of proportional valve", International Conference on Advanced Engineering Materials and Architecture Science, ICAEMAS, Xi'an, **488**, pp. 1231 – 1234,

[52] Ding, C., Ding, F., Zhou, X., Liu, S., and Yang, CJ., (2013), "Novel Pressure-Resistant Oil-Immersed Proportional Actuator for Electrohydraulic Proportional Control Valve", ASME J. Mech. Des. **135** (12), p. 125001,

[53] Senatore, A., Cardone, M., Buono, D., and Balsamo, F., (2008), "Experimental Analysis of a Ship Stabilization Hydraulic System", TEHNONAV International Conference, Constanta, **X**(I), pp. 1-7,

[54] Lee, G. S., Sung, H., J., and Kim, H., C., (2010), "Flow Force Analysis of a Variable Force Solenoid Valve for Automatic Transmissions", ASME J. Fluids Eng. **132**(3), p. 031103,

[55] Liu, Y.-F., Dai, Z.-K., Xu, X.-Y., and Tian, L.,, (2011), "Multi-domain modeling and simulation of proportional solenoid valve", J. Cent. South Univ. Technol., **18**(05), pp.1589-1594,

[56] Watton, J., and Tadmori, M. J., (1988), "A comparison of techniques for the analysis of transmission line dynamics in electrohydraulic control systems" Appl. Math. Modell., **12**(5), pp. 457– 466,

[57] Min, B., Xin, F., and Ying, C., (2001), "Computational Fluid Dynamics Approach to Pressure Loss Analysis Of Hydraulic Spool Valve", 5th International Conference on Fluid Power Transmission and Control, pp. 467 – 471,

[58] Gamboa, A. R., Morris, C. J., and Forster, F. K., (2004), "Improvements in Fixed-Valve Micropump Performance Through Shape Optimization of Valves", ASME J. Fluids Eng., **127**(2), pp. 339 – 346,

[59] Rannow, M. B., and Perry, Y. Li, (2012), "Soft Switching Approach to Reducing Transition Losses in an On/Off Hydraulic Valve", ASME J. Dyn. Syst., Meas.,,Control, **134**(6), p. 064501,

[60] Yuan, Q. H., and Perry, Y. Li, (2007), "Robust Optimal Design of Unstable Valves", IEEE Trans. on Control Syst. Technol., **15**(6), pp. 1065-1074,

[61] Davis, J. A., and Stewart, M, (2002), "Predicting Globe Control Valve Performance - Part I: CFD Modeling", J. Fluids Eng **124**(3), pp. 778–783,

[62] Manring, N. D., (2004), "Modeling Spool -Valve Flow Forces", ASME Paper No. IMECE2004-59038,

[63] Manring, N. D., and Zhang, S., (2011), "Pressure Transient Flow Forces for Hydraulic Spool Valves", ASME J. Dyn. Syst., Meas., Control, **134**(3), p. 034501,

[64] Morita, R., Inada, F., Mori, M., Tezuka, K., and Tsujimoto, Y., (2006), "CFD Simulations and Experiments of Flow Fluctuations Around a Steam Control Valve", ASME J. Fluids Eng **129**(1), pp. 48-54,

[65] Senatore, A., Buono, D., Frosina E., Pavanetto, M., Contin, I., and Olivetti M., (2014), "Improving the performance of a two way control valve using a 3D CFD modeling", ASME Paper No. IMECE2014-38201,

[66] Schleihs, C., Viennet, E., Deeken, M., Ding, H., Xia, Y., Lowry, S., and Murrenhoff., H., (2014), "3D-CFD simulation of an axial piston displacement unit", 9th International Fluid Power Conference, pp. 332–343,

[67] Ding, H, Lu, XJ, and Jiang, B., (2012), "A CFD model for orbital gerotor motor", Earth and Environmental Science, **15**(6), pp. 062006,

[68] Franzoni, F., Milani, M., and Montorsi, L., (2007), "CFD Multidimensional Approach to Hydraulic Components Design", SAE Technical Paper 2007-01-4196,

[69] Davis, J. A., and Stewart, M., (2002), "Predicting Globe Control Valve Performance - Part II: Experimental Verification", J. Fluids Eng **124**(3), pp. 772–777,

[70] Leutwyler, Z., and Dalton, C., (2006), "A Computational Study of Torque and Forces Due to Compressible Flow on a Butterfly Valve Disk in Mid-stroke Position" J. Fluids Eng., **128**(5), pp. 1074-1082,

[71] Blackburn, J. F., Reethof, G. and Shearer, J. L., (1960), "Fluid Power Control", The MIT Press,

[72] Merritt, H. E., (1967), "Hydraulic Control Systems", John Wiley & Sons, Inc.

[73] Senatore, A., Buono, D., Frosina, E., Pavanetto, M., Costin, I.J., Olivetti, M., (2014), "Improving the position control performance of a proportional spool valve, using a 3D CFD modeling", IFPE Las Vegas.